COMPRESSIBILITY EFFECTS ON KELVIN-HELMHOLTZ INSTABILITY AND MIXING LAYER FLOWS

A Dissertation

by

MONA KARIMI

Submitted to the Office of Graduate And Professional Studies of
Texas A&M University
in partial fulfillment of the requirements for the degree of

DOCTOR OF PHILOSOPHY

Chair of Committee,	Devesh Ranjan
Co-Chair of Committee,	Sharath S. Girimaji
Committee Members,	Diego A. Donzis
	Jean-Luc Guermond
	Eric L. Petersen
	Helen L. Reed
Head of Department,	Andreas A. Polycarpou

May 2015

Major Subject: Mechanical Engineering

ABSTRACT

The objective of the thesis is to analyze, understand and explicate the various physical mechanisms underlying the suppression of instability and mixing in compressible mixing layers. The investigation comprises of three studies which employ linear analysis and Direct Numerical Simulation (DNS). The first study examines the effect of compressibility on the underlying planar Kelvin-Helmholtz (KH) instability. The transformative influence of compressibility on the ubiquitous free shear-flow instability is investigated. This study focuses on the change in the character of pressure from a Lagrange-multiplier in incompressible flows to a thermodynamic variable in compressible flows. Linear analysis reveals that compressibility engenders the formation of a dilatational-interface-layer (DIL) within which the velocity perturbation is wave-like rather than vortical. Inherently unsteady dilatational action is shown to disrupt vortex merging and roll-up leading to suppression of KH instability. The second study examines the effect of perturbation alignment and non-linear interaction on the stability of compressible mixing layers. Linear analysis clearly shows that compressibility effects diminish with increasing obliqueness of the perturbation with respect to the shear plane. Notably, spanwise perturbations are impervious to Mach number effects. The non-linear effects are examined using DNS. It is shown that triadic interactions among the perturbation wavemodes lead to new perturbation wavemodes that are aligned closed to the spanwise directions and hence unstable. The third study examines mixing layer flow structure at various Mach numbers. At low speeds, the mixing layers exhibit strong spanwise rollers and short streamwise

ribs. The effect of Mach number on the evolution of structures and the interaction between them are investigated in detail. With increasing Mach numbers, the spanwise rollers are suppressed. In the absence of spanwise rollers, the streamwise ribs align to form streamwise structures.

to those whom I adore,

"قومی متفکرند اندر ره دین
قومی به گمان فتاده در شک و یقین
می ترسم از آنکه بانگ آید روزی
کای بی خبران راه نه آن است و نه این"

خیام نیشابوری

TABLE OF CONTENTS

Page

ABSTRACT ii

DEDICATION iv

TABLE OF CONTENTS vi

LIST OF FIGURES ix

LIST OF TABLES xv

I INTRODUCTION 1

I.A. Objectives 2
I.B. Approach 4
I.C. Dissertation Outline 5

II LITERATURE REVIEW 8

II.A. Linear Stability of Compressible KH and Mixing Layers 8
II.B. Experimental Studies of Compressible Mixing Layers . 11
II.C. Numerical Simulations of Mixing Layers 13
II.C.1. Role of Obliqueness 14
II.C.2. Non-linearity 15
II.C.3. Mixing Layer Structure 16
II.D. Compressibility Parameters 17
II.D.1. Convective Mach number, M_c 18
II.D.2. Relative Mach number, M_r 20
II.D.3. Turbulent Mach number, M_t 21
II.D.4. Gradient Mach number, M_g 21

III GOVERNING EQUATIONS AND LINEAR STABILITY ANALYSIS 24

III.A. Linear Stability Analysis 25

CHAPTER Page

IV NUMERICAL SCHEME FOR TEMPORAL MIXING LAYER SIMULATIONS 37

IV.A. Numerical Scheme 37
IV.A.1. Gas-Kinetic Method 38
IV.B. Mixing Layer Simulations 44
IV.B.1. Scheme Implementation 48
IV.B.2. Boundary Conditions 49
IV.B.3. Initial Conditions 50
IV.B.4. Simulation Parameters 53
IV.C. Validation Studies 53
IV.C.1. Validation for Stability Simulations 54
IV.C.2. Validation for Turbulence Simulations 55
IV.C.3. Convergence Study 56

V EFFECT OF COMPRESSIBILITY ON KELVIN-HELMHOLTZ INSTABILITY 61

V.A. Linear Analysis 61
V.B. Direct Numerical Simulations 63
V.B.1. Mixing Metrics 66
V.C. KH Instability Mechanism at Low Mach Numbers . . . 73
V.D. KH Instability Dynamics at High Mach Numbers . . . 76
V.D.1. Gradient Mach Number as a Compressibility Parameter 76

VI EFFECT OF OBLIQUENESS AND NON-LINEAR INTERACTIONS 85

VI.A. Linear Stability of Oblique Perturbations 85
VI.B. Simulations of Single Oblique Modes 89
VI.C. Effect of the non-linear interactions 100
VI.C.1. Simulations of Coupled Oblique Modes 103

VII MIXING LAYER FLOW STRUCTURE 113

VII.A. Vortical Structure of Turbulent Mixing Layers 113
VII.B. Vortical Structure at Linear Growth Regime 116

CHAPTER Page

VII.C. Segregation of Two Streams 119

VIII SUMMARY AND CONCLUSIONS 122

REFERENCES 125

LIST OF FIGURES

FIGURE		Page
I.1	Variation of normalized spreading rate with Mach number	3
I.2	Current approaches in studying mixing layers in available literature .	5
I.3	Schematic representation of a planar mixing layer flow	6
III.1	Schematic representation of a typical oblique wavemode	32
III.2	Schematic of modal stability of incompressible and (b) compressible homogeneous shear flows	35
IV.1	Flow chart describing GKM steps	45
IV.2	(a) spatial mixing layer in the laboratory frame of reference, (b) temporal mixing layer in the convective frame of reference	46
IV.3	Schematic of the temporal mixing layer	48
IV.4	Schematic of the computational domain for the temporally evolving shear layer	49
IV.5	Schematic of a typical oblique mode in modal simulation	50
IV.6	Schematic diagrams (not to scale) of the initial perturbation mode within the computational domain: (a) streamwise, (b) spanwise, and (c)oblique wave modes	52
IV.7	Temporal evolution of the turbulent kinetic energy at M_c =(a) 0.8 and (b) 1.05.	55
IV.8	Time evolution of the normalized momentum thickness. Dash-dot lines correspond to the DNS results.	56

FIGURE Page

IV.9 (a) Streamwise, (b) cross-stream r.m.s. velocity, and (c) the Reynolds shear stress along the normal direction in compressible mixing layer at $M_c = 0.7$. Symbols correspond to experimental data at $M_c = 0.64$, whereas dash-dot lines correspond to the DNS results at $M_c = 0.7$. 57

IV.10 Temporal evolution of the normalized turbulent kinetic energy for different resolution of $N_{x_1} \times N_{x_2} \times N_{x_3}$ and the fixed time-step of $\Delta t = 10^{-5}$. 59

IV.11 Temporal evolution of the normalized turbulent kinetic energy for different time-step of Δt for the simulations in the computational domain with the fixed resolution of $256N_{x_1} \times 512N_{x_2} \times 128N_{x_3}$. 60

V.1 A schematic representation of the flow conditions and computational geometry of a mixing layer initialized to a hyperbolic tangent profile for the mean velocity as $\bar{u} = (\Delta U/2 \tanh(x_2/\delta_m^0), 0, 0)$; initial velocity perturbation field of $u_i' = (0, \hat{u}_2^0 \sin(\kappa_1 x_1), 0)$; pivot point P; stagnation points S_1, S_2; and quadrants marked by $Q_1 - Q_4$. 65

V.2 Temporal evolution of the normalized (a) momentum thickness and (b) vorticity thickness at different Mach numbers when the initial obliqueness angle is zero, β=0. 67

V.3 Temporal evolution of the normalized turbulent kinetic energy and the normal component of the turbulent kinetic energy at different Mach numbers when the initial obliqueness angle is zero, β=0. 68

V.4 Temporal evolution of the normalized enstrophy at $M_c =$ 0.3, 0.7 and 1.2. 69

V.5 Sketch of the closed curve for calculating circulation on the $x_1 - x_2$ plane. 69

FIGURE Page

V.6 Temporal evolution of the normalized circulation in (a) the incompressible mixing layers at $M_c = 0.3$ and 0.6 and (b) the compressible mixing layers at $M_c = 0.8, 1.0$ and 1.2 71

V.7 Temporal evolution of the perturbation field for a mixing layer with the initial velocity field of $\beta = 0$ at (a) $M_c = 0.3$ and (b) $M_c = 1.2$. 72

V.8 $x_1 - x_2$- plane contours of pressure perturbation contours (on the left) and spanwise vorticity perturbation (on the right) of a mixing layer at $M_c = 0.3$, illustrating *Stage 1* in (a-b), *Stage 2* in (c-d) and *Stage 3* in (e-f) of the KH instability development in the incompressible flows. 75

V.9 Gradient Mach number contours for $M_c = 1.2$ at $\tau =$ (a) 0, (b)10, (c)24, (d)64, (e)105 , (f)172, (g)209, (h)257 ,(i)287, (j)345, (k)355 and (l) 375. Solid dark blue line indicates $M_g = 1$. . . 77

V.10 A schematic of a compressible mixing layer; the dilatational interface layer where $M_g > 1$; two stagnation points (S_1 and S_2); and propagated pressure waves in the outer region (color online). 78

V.11 Profiles of the flow velocity (solid line) and speed of sound (dashed line); U_c is the convective velocity in a mixing layer given by (2.6); a is the average speed of sound which varies along the normal direction at (a) stationary (b) convective coordinates frames, taken from [1] 79

V.12 Contours of pressure perturbation (on the left) and spanwise vorticity perturbation (on the right) of a mixing layer at $M_c =$ 1.2, illustrating *Stage 1* in (a-b), *Stage 2* in (c-f) of the KH instability development in the compressible flows. 81

V.13 Schematic representation of contrasting the stages of development of the KH instability in compressible flows (on the right) against the incompressible counterpart (on the left); and $u_2' S$ are marked by solid black arrows. 84

FIGURE Page

VI.1 Schematic of modal stability for compressible mixing layers 86

VI.2 Schematic diagrams (not to scale) of the initial perturbation mode within the computational domain: (a) streamwise, (b) spanwise, and (c)oblique wave modes 91

VI.3 The temporal evolution of the normalized momentum thickness and the normalized vorticity thickness at different Mach numbers when the initial obliqueness angle is zero, β=0. 92

VI.4 The temporal evolution of the normalized turbulent kinetic energy and the normal component of the turbulent kinetic energy at different Mach numbers when the initial obliqueness angle is zero, β=0. 92

VI.5 The temporal evolution of the normalized momentum thickness and the normalized vorticity thickness at different Mach numbers when the initial obliqueness angle $\beta = \pi/2$. 94

VI.6 The temporal evolution of the normalized turbulent kinetic energy and the normal component of the turbulent kinetic energy at different Mach numbers when the initial obliqueness angle is $\pi/2$, $\beta = 90$. 94

VI.7 The temporal evolution of the normalized momentum thickness and the normalized vorticity thickness at different Mach numbers when the initial obliqueness angle is $\beta = \pi/6$. 97

VI.8 The temporal evolution of the normalized turbulent kinetic energy and the normal component of the turbulent kinetic energy at different Mach numbers when the initial obliqueness angle is $\beta = \pi/6$. 97

VI.9 The temporal evolution of the normalized momentum thickness and the normalized vorticity thickness at different Mach numbers when the initial obliqueness angle is $\beta = \pi/3$. 98

FIGURE Page

VI.10 The temporal evolution of the normalized turbulent kinetic energy and the normal component of the turbulent kinetic energy at different Mach numbers when the initial obliqueness angle is $\beta = \pi/3$. 98

VI.11 Stability map of the compressible mixing layer 100

VI.12 Sketches of the three types of triad interactions among wavemodes . 103

VI.13 Schematic representation of the initial wavemode in the $\kappa_1-\kappa_3$ plane for (a) a singleton with the obliqueness angle of $\beta = \pi/4$ and (b) a pair wavemode with the obliqueness angle of $\beta = (\pi/4, -\pi/4)$.105

VI.14 The evolution of the turbulent kinetic energy for a singleton with the obliqueness angle of $\beta = \pi/4$ and a pair wavemode with the obliqueness angle of $\beta = (\pi/4, -\pi/4)$ at (a) $M_c = 0.3$ and (b)$M_c = 1.2$. 106

VI.15 Temporal evolution of the wavevector spectrum of a singleton at Mach number contours for $M_c = 0.3$ at $\tau =$ (a) 0, (b)4, (c)8, (d)12, (e)16, (f)21, (g)25, (h)29, (i)31, (j)33, (k)37 and (l) 41. Dash gray line indicates the initial obliqueness angle. 109

VI.16 Temporal evolution of the wavevector spectrum of a singleton at Mach number contours for $M_c = 1.2$ at $\tau =$ (a) 0, (b)4, (c)8, (d)12, (e)17, (f)20, (g)23, (h)27,(i)33, (j)37, (k)40 and (l) 43. Dash gray line indicates the initial obliqueness angle. 110

VI.17 Temporal evolution of the wavevector spectrum of a pair wavemode at Mach number contours for $M_c = 0.3$ at $\tau =$ (a) 0, (b)4, (c)8, (d)12, (e)16, (f)21, (g)25, (h)29, (i)31, (j)33, (k)37 and (l) 41. Dash gray line indicates the initial obliqueness angle. . . . 111

VI.18 Temporal evolution of the wavevector spectrum of a pair at Mach number contours for $M_c = 1.2$ at $\tau =$ a) 0, (b)4, (c)8, (d)12, (e)17, (f)20, (g)23, (h)27 ,i)33, (j)37, (k)40 and (l) 43. Dash gray line indicates the initial obliqueness angle. 112

FIGURE Page

VII.1 Vorticity plots of the turbulent mixing layer simulation with the initial flow conditions of [2] at $M_c = 0.3$. 114

VII.2 Vorticity plots of the turbulent mixing layer simulation with the initial conditions of [2] at $M_c = 1.2$. 115

VII.3 Side view of vorticity contours at the initial convective Mach number of 0.3 at $\beta =$ (a) 0, (b) 30, (c) 60 and (d) 90 116

VII.4 Side view of vorticity contours at the initial convective Mach number of 1.2 at $\beta =$ (a) 0, (b) 30, (c) 60 and (d) 90 116

VII.5 Top view of vorticity contours at the initial convective Mach number of 0.3 at $\beta =$ (a) 0, (b) 30, (c) 60 and (d) 90 117

VII.6 Top view of vorticity contours at the initial convective Mach number of 1.2 at $\beta =$ (a) 0, (b) 30, (c) 60 and (d) 90 117

VII.7 The temporal evolution of the velocity perturbation pathlines with the embedded vorticity contour plots for a mixing layer with the initial isotropic turbulent velocity field at $M_c = 0.3$ (a) initial $\tau = 0$ (b) at $\tau = 250$ (color). 120

VII.8 The temporal evolution of the velocity perturbation pathlines with the embedded vorticity contour plots for a mixing layer with the initial isotropic turbulent velocity field at $M_c = 1.2$ (a) initial $\tau = 0$ (b) at $\tau = 250$ (color). 121

LIST OF TABLES

TABLE Page

IV.1 Parameters for the validation simulations 56

IV.2 Simulations parameters for grid convergence studies 58

V.1 Initial physical and numerical parameters for the KH instability simulations 64

VI.1 Simulation parameters for the study of the obliqueness angle effects . 90

VI.2 Simulation parameters for non-linear effects study 104

I

INTRODUCTION

Kelvin-Helmholtz (KH) instability occurs at the interface of two fluid layers in relative motion or in a state of stratification. The KH instability is not only important in atmospheric and oceanic flows [3–6], in geophysics and astrophysics [7–10], but also as well as in engineering applications. For example, in astrophysical plasma flows, the interface between the solar wind and the Earth's magnetosphere [11] can create KH-like waves or *billows*. This instability is also believed to occur in many astrophysical plasmas such as the magnetopause [12], the planetary magnetosphere [7, 13], Earth's auroa [14], cometary tails [15], supernovas [16–18], protoplanetary disks [19], jets and outflows [20, 21], and other astrophysical situations.

The KH instability is of great importance in the turbulent mixing of engineering flows [22]. In the field of aerodynamics, this instability occurs in mixing layers, jets and wakes. This instability is the central mixing mechanism in free shear flows. Due to the ubiquitous nature of KH instability, especially in shear layers, it has been an important research topic in both fundamental investigations [23] and engineering applications [24]. While the KH instability in incompressible flows has been investigated exhaustively, its behavior in compressible flows has not been thoroughly examined. Therefore, there is a need to understand the KH instability, in particular, and corresponding mixing layer behavior, in general, in compressible shear layers of interest in nature and engineering flows.

For the past several decades, it has been established that the mixing layer growth

rate reduces as the Mach number increases [1, 25–29]. To empirically represent the compressibility effects in the supersonic regime, a functional form for the mixing-layer spreading rate was proposed by Papamoschou and Roshko [1]. Further experiments have supported this functional form and have been consolidated to the so-called *Langley Curve* (Figure I.1) compiled by Birch & Eggers [30]. The Langley Curve presents the ratio between the spreading rate of a compressible mixing layer to its corresponding incompressible value at different Mach numbers. Initially, it was speculated that some of the observed effects could be due to density difference [31]. Later, it was emphatically demonstrated that high-speed compressibility effects, rather than density effects, were responsible for the growth rate reductions (Brown & Roshko [32]; Bradshaw [33]; Papamoschou & Roshko [1, 31]).

The evolution of compressible mixing layers has also been investigated through several direct numerical simulations (DNS): Sandham & Reynolds [34], Vreman *et al* [35], Freund *et al* [36] and large eddy simulations (LES) by Comte *et al* [37], Foysi & Sarkar [38] and Hadjadj *et al* [39]. There is general agreement amongst the numerical studies that turbulence production and momentum thickness decrease with increasing Mach number. KH instability is the principal mixing mechanism and thus any fundamental study of mixing layer efficiency must address the underlying flow physics.

I.A. Objectives

At the current stage of development, there is clear evidence that the KH instability is profoundly affected by compressibility. Many studies (reviewed in Chapter *II*)

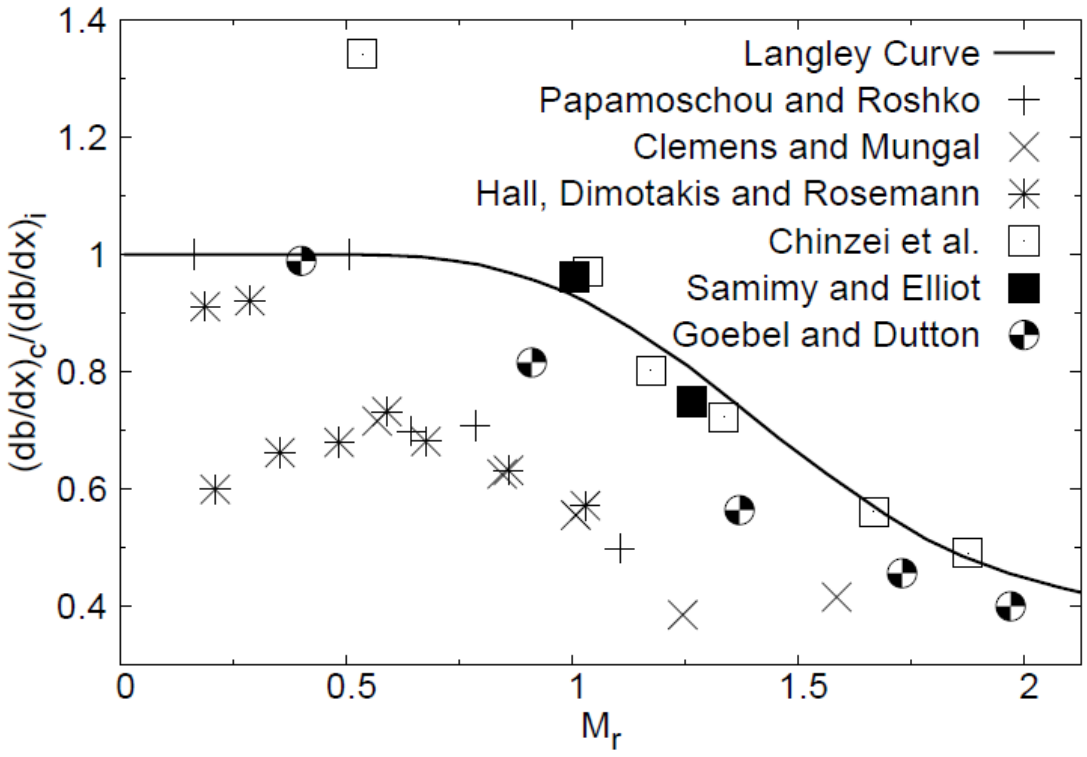

Figure I.1. Variation of normalized spreading rate with Mach number

have been performed to understand the various effects of compressibility on mixing layers leading to important progress. However, the fundamental nature of this effect and the underlying physical mechanisms are still unclear. Specifically, the precise pressure-velocity interaction mechanism underlying the influence of compressibility is yet to be explicated. Most importantly, the effect of compressibility on the KH instability is not clearly understood. To address these questions, we formulate the objectives of this work as follows:

1. The primary objective is to examine the influence of compressibility on the Kelvin-Helmholtz instability with a particular emphasis on the underlying physical mechanism. Linear stability analysis and direct numerical simulation will be performed to explicate the flow physics. The flow physics will be compared and contrasted against the KH instability in incompressible flows.

2. The second objective is to examine the effect of perturbation obliqueness and non-linear interaction on the mixing efficiency in compressible mixing layers.

3. The final objective is to examine the transformation in flow and vortical structure in the mixing layer as a function of Mach number.

I.B. Approach

To study the influence of compressibility on the KH instability and mixing layers, extant tools can be classified into three categories of: (i) experiments, (ii) stability analyses and (iii) numerical simulations. An overview of these approaches is illustrated in Figure I.2. The present study employs the approaches in the shaded boxes:

inviscid linear stability analysis and results from direct numerical simulations. Using

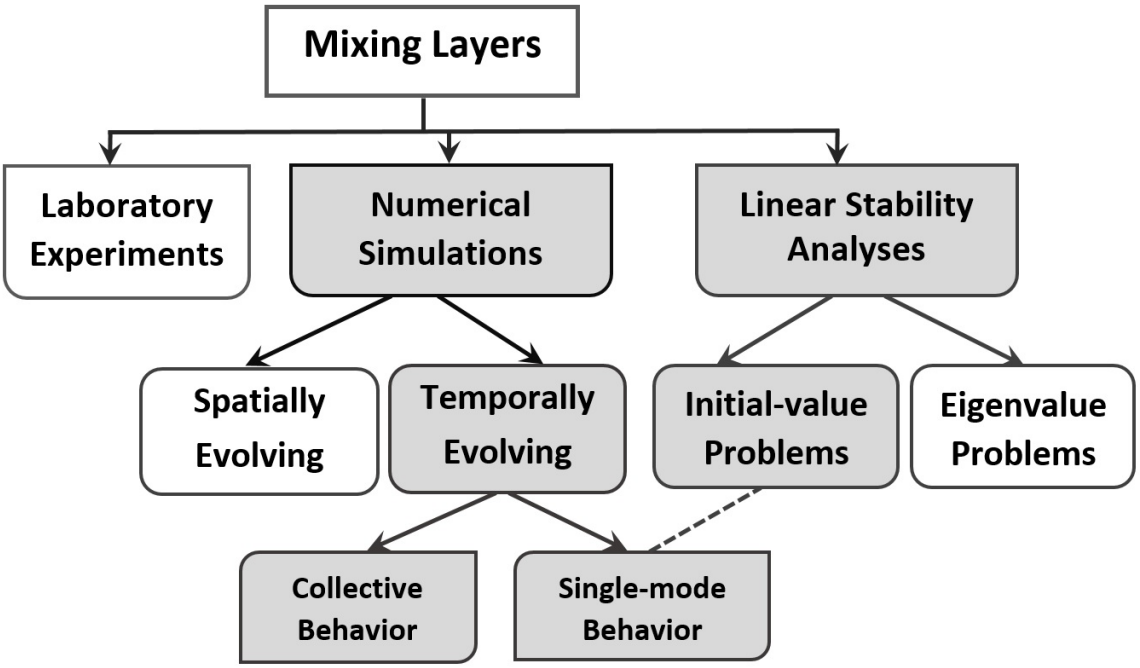

Figure I.2. Current approaches in studying mixing layers in available literature

linear stability analysis, we identify the relevant mechanisms and important flow features responsible for the onset and the development of the instability. Once the right mechanisms are identified, their effect is examined in detail by using direct numerical simulations. While most stability analyses examine an eigenvalue problem [40–43], the present linear analysis solves an initial value problem and correspondingly simulates a temporal mixing layer to highlight transient dynamics.

I.C. Dissertation Outline

In this work, we examine instability and turbulence in a planar mixing layer of the type shown in Figure I.3. Shear is generated by two nearly-parallel streams of

fluids with unequal velocities and, often in the compressible case, unequal densities. This dissertation only examines the effect of large shear rate. The figure shows two streams of mean velocity U_i, Mach number M_i, and density ρ_i merging to form a mixing layer. In each stream, the speed of sound can also differ.

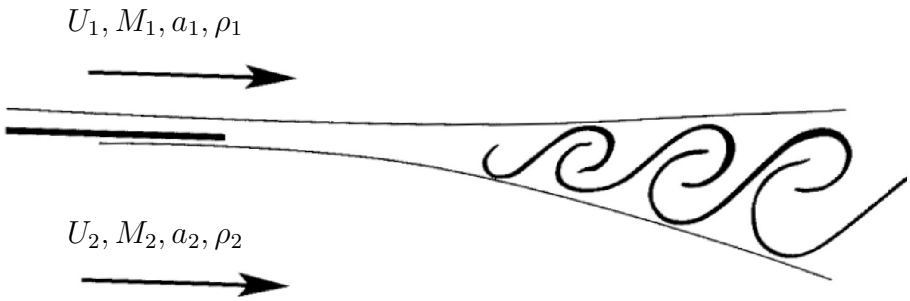

Figure I.3. Schematic representation of a planar mixing layer flow

This dissertation is organized as follows: Chapter II presents a complete literature review of the previous relevant theoretical, numerical and experimental work in the context of the KH instability and mixing layers in compressible flows, followed by a brief discussion of the compressibility parameters. The relevant linear initial value problem is formulated in Chapter III. The numerical method used for the DNS, the gas-kinetic method, is detailed in Chapter IV. The specification of the initial conditions, boundary conditions, and other simulation parameters are also discussed in Chapter IV. Extensive validation studies of the present scheme against recent DNS data and available experimental results for supersonic mixing layers will close Chapter IV. Using the tools introduced in Chapters III and IV, we proceed to describe the main three studies of the dissertations in Chapters V, VI, and VII. In Chapter V, the modification and inhibition of the KH instability in the presence of compressibility

are explicated. Chapter VI presents the DNS results of mixing layers to highlight the effect of perturbation obliqueness at different Mach numbers. In Chapter VII, the effects of compressibility and perturbation obliqueness on the vortical structure of the mixing layer are examined. Finally, Chapter VIII provides a brief summary of the salient findings of this work.

II

LITERATURE REVIEW

In this chapter, we review the important contributions in the area of incompressible and compressible KH instability and mixing layers. This review is categorized along the line of stability analyses, experimental studies and numerical simulations. We close this chapter by compiling a list of non-dimensional parameters that characterize compressibility effects in mixing layers.

II.A. Linear Stability of Compressible KH and Mixing Layers

Rayleigh was the first to address the stability characteristics of incompressible shear flows and identify the importance of the inflection point in the mean velocity profile [44]. One of the earliest compressible mixing layer stability investigations was conducted by Miles [45]. In this paper, the KH instability is established between a layer of low-viscosity liquid located over a layer of air. While speeds of two layers are small, this paper still yields valuable insight into the mechanism in high-speed flows. Inviscid linear stability analyses of a high-speed compressible mixing layer include: spatial analysis of Gropengiesser [42] and temporal stability analyses of Lessen *et al* with subsonic and supersonic initial disturbances [40, 41]. In these studies, a hyperbolic tangent profile is used as the base flow. Using the inviscid temporal stability analysis, Lessen *et al* established that viscosity has a stabilizing influence on a compressible mixing layer [40, 41]. While Lessen *et al* assumed the temperature of the stationary stream is higher than that of the moving gas, Gropengiesser varied the

temperature ratio of the two streams as an input parameter. Both concurred that growth rate decreases as Mach number increases. Gropengiesser observed the growth reduction of instability with the increase of Mach numbers. These stability results were later verified by Ragab & Wu [43]. Besides the growth rate, the propagation of disturbances at oblique angles to the streamwise direction was also examined [40,42], demonstrating that the shear layer becomes more unstable as this angle increases.

Assuming uniform temperature through the layer, later studies investigated the temporal stability of a compressible mixing layer [46–48]. Jackson & Grosch [49, 50] conducted an inviscid stability study of a compressible mixing layer, considering both two- and three-dimensional perturbation fields. Their base flow, including stationary and moving streams, was described by a hyperbolic tangent profile. The temperature was determined by the Crocco-Busemann's relation [51] which specifies the initial temperature profile as a function of the initial velocity field and Mach number. Over a wide range of Mach numbers, Jackson & Grosch classified unstable modes as follows [49]: (i) at low Mach numbers there exists only one class of modes, called *subsonic modes*, where growth rate decreases with the increase of Mach number, (ii) at high Mach numbers, there are two classes of unstable modes: *fast modes* and *slow modes*. These two bands of unstable frequencies can be related to the phase-speed ratio between the two streams. Therefore, a reference Mach number, M_*, to related these two freestream phase-speeds was introduced as follows [49]:

$$M_* \equiv \frac{1 + (T_{-\infty}/T_{+\infty})^{1/2}}{cos(\theta)}, \tag{2.1}$$

M_*reference Mach number where θ is the angle of propagation of the disturbance wave with respect to the streamwise direction. $T_{-\infty}$ and $T_{+\infty}$ are the freestream

temperatures at $y = -\infty$ and $y = +\infty$, respectively. Fast modes are supersonic with respect to the stationary stream and exist at Mach numbers greater than M_*. Slow modes, existing at Mach numbers less than M_*, are supersonic with respect to the moving stream. Both modes are vorticity modes, not acoustic modes [52]. As Mach number approaches unity, Jackson & Grosch [49] showed that the proposed existence of the supersonic fast and slow modes was in agreement with previous work [47, 48].

Most early analyses demonstrated that under the incompressible K-H instability, small perturbations along the interface between two fluids first experience linear growth stages [53–57], and then undergo nonlinear growth stages [9, 58–60] which may lead to turbulent mixing due to the nonlinear interactions among perturbation modes. In stratified flows, Chimonas [61] found that the growth rate of the fastest growing mode in a plane-parallel stratified shear flow is of the order of S^2 (square of shear rate).

Betchov & Szewczyk conducted a linear stability analysis of a laminar shear layer [62] which we use to expand upon the rationale of *inviscid* analysis. By the linear stability diagram of a two dimensional mixing layer (Fig.2 of [62]), they demonstrated that the perturbation amplification rates are no longer affected by viscosity when the Reynolds number exceeds 40. In other words, as the Reynolds number increases, instability becomes inviscid such that it can be well described by the Rayleigh equation [63].

Employing a spatial linear stability analysis, Ragab & Wu [43] investigated the effects of three parameters on the growth rate of compressible mixing layers: the velocity ratio, the temperature ratio, and the Mach number. Considering both in-

viscid and viscous stability, a hyperbolic tangent profile for the initial base velocity field and Sutherland's profile for the initial base temperature field were used. Their major findings concluded that (i) the dependence of the maximum growth rate on the velocity ratio for a compressible mixing layer required more complex representation as compared to the one for incompressible flows, (ii) the compressible mixing layer had an inviscid inflection instability, thus the viscosity delayed the growth of the disturbances independent of their frequencies, and (iii) non-parallel effects were observed as negligible factors for compressible mixing layers.

II.B. Experimental Studies of Compressible Mixing Layers

There is an extensive amount of experimental work in the field the mixing layer stability. However, most studies have focused on the incompressible flows rather than compressible ones. Evidently this is due the fact that most operating conditions cannot be easily replicated in any ground-based experimental facility. Here we discuss some of those experimental studies which are relevant to our subject matter.

Early experimental studies on a chemically–reacting, turbulent shear flow by Breidenthal [64] showed that streamwise streaks appeared as a result of stretching the spanwise instability wave, which forms in the early stage of flow development. In fact, Winant & Browand [65] were the first to explain the early stage of transition mechanism in mixing layer flows. They proposed that in the case of sufficiently large Reynolds numbers, the vortical lumps of fluid begin rolling due to the initial shear. The successive amalgamation of spanwise vortices is the main process contributing to the mixing layer growth in the streamwise direction. Consequently, the vorticity

initially contained in the base velocity profile is being redistributed into larger and larger vortices, their wavelength and strength being doubled after each interaction.

One of the experimental works examining the structure development of mixing layers is that of Lasheras *et al* [66]. Their work illustrated that for incompressible flows, mixing transition can be explained by the development of secondary instability, which is followed by the KH as a primary instability. While KH instability is associated with spanwise rollers, secondary instability can be related to vortical braids or ribs. By examining the effects of the initial perturbations on the shear layer development, Lasheras *et al* [66] concluded that a positive strain (stretching) of the interface between two streams is produced by the first KH wave, and the magnitude and the location of the braids are correlated to the amplitude of the the first KH wave and to the initial position of the perturbation. Lasheras *et al* observed that streamwise vortical structures initially form between two consecutive spanwise rollers, which is perhaps why they are known as braids. These braids then propagate into the cores of the rollers.

A notable experimental study of the compressible mixing layer was conducted by Elliot & Samimy [67]. Employing planar laser Doppler velocimetry, they measured the relevant turbulence characteristics of a fully developed flow. Their results exhibited that as the Mach number increases there is a reduction in the turbulent intensities and the Reynolds stresses. The reduction of the mixing layer growth as Mach number increases has been observed experimentally by Papamoschou & Roshko [1], Goebel & Dutton [29], Clemens & Mungal [26] and many others researchers [25,27,68] as well.

II.C. Numerical Simulations of Mixing Layers

While linear analyses establish asymptotic characteristics of the evolution, numerical simulations have been widely used to understand the stability mechanism in compressible mixing layers. It is has been found that for incompressible mixing layers, streamwise KH instability grows until the saturation of the axisymmetric spanwise rollers [69, 70]. Spanwise rollers interact with each other and eventually coalesce through a pairing mechanism. In addition to the spanwise rollers, other organized and reoccurring structures have been observed through various experimental studies (Brown & Roshko [71]; Winant & Browand [65]; Hernan & Jimenez [72]; Jimenez [73]; Lasheras *et al* [66]; Bernal & Roshko [74]; Cho & Maxworthy 1986; Bell & Mehta [68]) and numerical investigations (Lin & Corcos [75]; Metcalfe *et al* [76]; Moser & Rogers [77]; Rogers & Moser [78], [79]). These vortical structures have been referred to by different names such as streamwise filaments, streamwise streaks, braids, or ribs. Note that these structures can only be observed in the vortical plane, normal to the streamwise flow direction. Ribs are formed between the spanwise rollers and are found to be counter-rotating with respect to the corresponding rollers. Numerical simulations also reveal the importance of the initial perturbation orientation, the non-linear interaction among the perturbation modes and flow structure toward understanding the effect of compressibility effects on the development of the mixing layers.

II.C.1. Role of Obliqueness

A numerical study conducted by Metcalfe *et al* [76] was an early attempt to identify the importance of the amplitude and orientation of the initial perturbation modes during the early-stage development of mixing layer instability. Although their work was limited to the incompressible limit, their results provided valuable insight in explaining the possible mechanism of transition applied to compressible mixing layers. Using a pseudo-spectral scheme, Metcalfe *et al* performed a temporal DNS to investigate pairing mechanism and other interaction between vortices as their initial perturbations. They showed that the introduction of a two-dimensional (or streamwise) disturbance can have a fundamental effect on the mixing layer evolution. Through their temporal simulation, they showed that despite more complexities in a turbulent mixing layer, there are three-dimensional secondary instabilities similar to those in boundary layer flows. They concluded that the linear instabilities in a wall-bounded flow are mainly driven by viscosity; therefore, linear instabilities are weak. Contrary to wall-bounded flows, free shear flows (e.g. mixing layers) are mainly driven by convection. As a result, free shear flows are subject to a variety of inviscid instabilities. Depending on which type of perturbation mode is dominant among other modes, the corresponding governing instability can be specified. Another remarkable finding of their temporal DNS was that the transition of mixing layers depends significantly on the past history of the flow. Metcalfe *et al* used the term *three-dimensionality* to refer to the very early stage of instability of the initial growth of the mixing layer. Although the term of three-dimensionality has been used by many researchers since, it is avoided in this work for reasons that will

be explained later. Oblique disturbances in the context of the compressible mixing layers were first discussed by Sandham & Reynolds [34].

In terms of the the initial perturbation wavevector, the critical role of obliqueness with respect to the shear plane has been further investigated in several studies [80–83]. It was demonstrated that the obliqueness angle affects the growth of the perturbation kinetic energy. Employing DNS of temporally evolving compressible mixing layer, Sandham & Reynolds [34] demonstrated that oblique disturbances are more unstable than two-dimensional initial disturbances. Additionally, they showed that a combination of a streamwise mode and a pair of oblique modes exhibited faster growth than a single mode [34]. However, that study does not investigate the effect of obliqueness or non-linearity in great detail.

II.C.2. Non-linearity

Most investigations have been studying the effect of compressibility in homogeneous shear flows and mixing layers, starting with a large set of isotropically distributed initial perturbation/fluctuation modes evolving in the corresponding background field. These studies then record the difference in the evolution of statistics at various levels of compressibility as indicated by Mach number. However, such an approach does not provide clear insight into various physical processes rendering closure modeling difficulties. It is essential to understand the behavior of the individual wave mode.

With the exception of the work [84], most, if not all, previous homogeneous shear turbulence investigations have focused on the evolution of collective-mode velocity

and pressure statistics. The statistics are gleaned from a collection of perturbation modes that are initially distributed in an isotropic manner. While this has led to important advances in understanding, a comprehensive explanation requires the characterization of individual mode behavior. This section delineates, building on the earlier work by [84], the evolution of pressure and velocity amplitudes of individual modes as a function of initial convective Mach number and initial wave-orientation.

Triadic interaction representation has been used in studying homogeneous turbulence [85, 86]. There is a large amount of valuable theoretical and numerical work in the realm of the role of the triadic interaction on the energy transfer in various types of flows such as: homogeneous shear turbulence [87, 88], the rotating stratified turbulence [89], and decaying isotropic turbulence [90]. Yet, triad interaction is not extensively explored in the domain of inhomogeneous shear flows .

II.C.3. Mixing Layer Structure

Most studies of the compressibility effects on the flow structures in mixing layers are restricted to relatively low-Mach number flows [70, 78, 79]. Although there have been a few studies in the context of compressible mixing layer structure [91–93], a detailed explanation for the underlying physics of how compressibility affects the structures of inhomogeneous shear flows is absent.

The morphology of the secondary instability was demonstrated in a frame-by-frame visualization by Bernal [94]. Although his work provided an overall picture of the counter-rotating structures residing in the spanwise plane (x-plane in Figure I.3), it was unclear whether these structures were the same wiggles around the rollers seen

in the streamwise plane (z-plane in Figure I.3). Later, other researchers demonstrated that the inception of the transition process in mixing layer flows began with the K-H instability. A major contributor to instability comes from the mixing of unmixed core fluid entrained during the initial two-dimensional development [74], when the coalescence of the spanwise vortices occurs mainly in the spanwise plane. Meanwhile, contribution to secondary instability starts with stretching vorticity along the braids in the normal plane and between the spanwise rollers. Hence, most authors call this phenomenon *three dimensionality instability* since it resides in two planes versus the KH-type, which is only in the streamwise plane. The secondary instability occurs via the formation of streamwise structures or ribs. Bernal and Roshko [74] deduced, that although the ribs play an indirect role in the mixing transition mechanism, both the primary instability (correlated to the spanwise rollers) and the secondary instability (correlated to the streamwise ribs) generate three-dimensionality. Additionally, they argued that amalgamation of the spanwise rollers redistributes three dimensionality. However, even Bernal and Roshko [74] themselves were not satisfied with the proposed argument of the transition growth in mixing layer flows, as they also mention that there might be *additional internal instabilities* in the flow.

II.D. Compressibility Parameters

To quantify compressibility effects, a variety of Mach numbers have been used in literature. However, the true utility of these Mach numbers in analyses strictly depends on the nature of the flow of interest. Although the physical interpretation of these Mach numbers may seem straightforward, the relevance may not always

be evident. It is important therefore to identify the appropriate Mach number for parametrizing a physical effect, based on the governing equations. For the sake of completion of discussion in this review, Mach numbers commonly used in the literature are introduced and discussed briefly. Consequently, in later chapters of this work, stability analysis (in Chapter III) and the DNSs (in Chapters V & VI) are used to identify the appropriate Mach number which embodies the effect of compressibility in mixing layers.

II.D.1. Convective Mach number, M_c

A dimensionless parameter called the convective Mach number, M_c, has been introduced by Bogdanoff [95] who expanded upon the earlier idea of Coles [96] that was further studied by Dimotakis [97] and Papamoschou & Roshko [1]. They proposed the parametrization of M_c based on a stability analysis of a temporally evolving vortex sheet. The convective Mach number for each stream can be defined with respect to the velocity of the large vortices [95] or the convective velocity, U_c. In a mixing layer between two parallel streams of flow with velocities U_1 and U_2 (where $U_1 > U_2$), we have

$$M_c^{(1)} \equiv \frac{U_1 - U_c}{a_1}, \quad M_c^{(2)} \equiv \frac{U_2 - U_c}{a_2}, \tag{2.2}$$

where a_1 and a_2 are the speeds of sound corresponding to the free stream velocities of U_1 and U_2, respectively. $M_c^{(1)}$ and $M_c^{(2)}$ are the convective Mach numbers relative to stream 1 and stream 2, respectively. Assuming the initial pressure across the interface between two streams is uniform, one can write:

$$\left(1 + \frac{\gamma_1 - 1}{2} M_{c^1}^2\right)^{\gamma_1/(\gamma_1-1)} = \left(1 + \frac{\gamma_2 - 1}{2} M_{c^2}^2\right)^{\gamma_2/(\gamma_2-1)}. \tag{2.3}$$

The two convective Mach numbers can be related by

$$M_c^1 = \left(\frac{\gamma_1}{\gamma_2}\right)^{1/2} M_c^2. \tag{2.4}$$

Considering the ρ_2/ρ_1 as the density ratio between two streams, U_c can also be written as

$$U_c = U_1 \frac{1 + (U_2/U_1)\sqrt{\rho_2/\rho_1}}{1 + \sqrt{\rho_2/\rho_1}}. \tag{2.5}$$

In the case of the incompressible uniform-density flow, convective velocity will simply be $U_c = (U_1 + U_2)/2$. Generally speaking, when $\gamma_1 \neq \gamma_2$ and $\rho_2 \neq \rho_1$, the two convective Mach numbers, M_c^1 and M_c^2, are different. Additionally, an asymmetric behaviour can be expected since compressibility effects may occur unevenly across the interface. Assuming the same specific heat ratio (γ) at both streams and the isentropic flow throughout, then $M_c^1 = M_c^2 = M_c$. The convective velocity (U_c) and convection Mach number (M_c) yield

$$U_c = \frac{U_1 a_2 + U_2 a_1}{a_1 + a_2}, \tag{2.6}$$

and

$$M_c \equiv \frac{U_1 - U_2}{a_1 + a_2} = \frac{\Delta U}{a_1 + a_2}, \tag{2.7}$$

where ΔU is the velocity difference between two streams. In this case, U_c is the velocity of the stagnation point rather than the velocity of the large-scale structures as presumed by Bogdanoff [95] earlier. It is noteworthy to mention that in the case of the three dimensional disturbances, the orientation of the propagation with respect to the shear plane shall be included [50]. Therefore, an effective convective Mach number can be defined by

$$M_{c_{eff}} = M_c \cos(\theta), \tag{2.8}$$

where θ is the obliqueness angle with respect to the streamwise direction as seen in (2.1). The inclusion of the projection of disturbances on the shear plane or $\cos(\theta)$ has been suggested by previous authors [34, 42, 98] based on heuristic arguments. Despite the apparent simplicity of the convective Mach number in (2.7), there are some concerns about considering it as a parameter: (i) it is empirically and intuitively evident that a mixing layer with one subsonic and one supersonic streams will behave differently from a mixing layer with two supersonic streams, in spite of having the same convective Mach number; (ii) equation (2.6) is based on the existence of the stagnation point in a convective frame of reference and the absence of shocks in a shear flow, which is implemented by the isentropic flow assumption. Clearly, this assumption is not valid for either highly compressible or reacting mixing layers. Therefore, M_c may not be the optimal physical parameter for quantifying compressibility in mixing layers.

II.D.2. Relative Mach number, M_r

Based on the velocity difference across the shear layer, Birch & Keyes [99] define the relative Mach number, M_r, as

$$M_r \equiv \frac{U_1 - U_2}{\bar{a}}. \tag{2.9}$$

where $\bar{a}$ is the average speed of sound of the two streams. In the case of the same specific heat ratio for both streams, the relative Mach number is simply twice the convective Mach number. Due to its easier measurement, this Mach number has been mainly used in experimental studies, such as [29].

II.D.3. Turbulent Mach number, M_t

Another Mach number to quantify compressibility is the turbulent Mach number, which is given by

$$M_t \equiv \frac{\sqrt{u'^2}}{a}, \tag{2.10}$$

where u' is the perturbation velocity and a is the speed of sound. In some situations this Mach number is not a useful parameter to characterize compressibility effects. For instance, if the velocity fluctuations are of smaller order than the speed of sound, we cannot expect shocks to be formed due to the fluctuating motion. Through the DNS of the compressible turbulence, it is demonstrated that the structure of homogeneous shear turbulence cannot be characterized by M_t, whereas decaying isotropic turbulence can. They observe that the former is independent of the initial conditions [100]. It is found that M_t cannot be a very informative parameter when there is a need to identify the ratio of the solenoidal to the non-solenoidal component of the velocity field [24].

II.D.4. Gradient Mach number, M_g

The definition of M_c requires a measure of relative velocity across a shear layer (see (2.7)). Thus, it can be formally linked to another compressibility parameter, the gradient Mach number, M_g, that was introduced by Sarkar [101]. In the case of a mixing layer, the initial value of the gradient Mach number can be defined by

$$M_g \equiv \frac{Sl}{\bar{a}}, \tag{2.11}$$

where S is the mean shear rate, $\bar{a}$ is the average of the speeds of sound of two streams, and l represents a characteristic or an appropriate length-scale of the perturbation

in the direction of shear. The parameter M_g can vary locally within a shear layer, whereas M_c involves the mean velocity difference across the entire shear layer; therefore, M_c is a global parameter. In other words, M_g can be interpreted as the ratio of two timescales: the ratio of an acoustic time for a large eddy $(l/\bar{a})$ to the mean flow timescale $(1/S)$.

It is useful to investigate whether there is any correlation between these Mach numbers, especially M_c, M_g, and perhaps M_t. In the self-similar region of a mixing layer, M_c can be an appropriate choice for a similarity parameter. In mixing layers, the mean shear rate, $\partial U/\partial y$ can be approximated as $\delta U/\delta_\omega$, where δ_ω is the vorticity thickness defined by $\delta_\omega = \Delta U/(\partial \bar{u_1}/\partial y)$. The integral lengthscale can be assumed to be of the order of δ_ω, while it can also vary by convective Mach number such that $l = f(M_c)\delta_\omega$. Therefore, one can write

$$M_g \approx \frac{\Delta U}{\delta_\omega}\frac{f(M_c)\delta_\omega}{\overline{a}} \approx M_c f(M_c). \tag{2.12}$$

Sarkar estimates that the value of M_g at the centerline of a mixing layer is a function of the convective Mach number in a linear relation as $M_g \approx 2.2M_c$ [101]. It is found that the parameter M_g is twice the value of M_c in high-speed mixing layers, whereas M_g remains almost constant in the boundary layer with the increase of the free-stream Mach number M_∞ (equivalent to the M_c in mixing layers)(Figure 14 of [101]). This may explain the difference between the extent of compressibility effects in the compressible mixing layer as opposed to the compressible boundary layer.

There has also been an attempt to derive a relationship between M_t and M_c [24]. In a mixing layer, it may be assumed that $u'/\Delta U = f^*(M_c)$, where f^* is the

normalized spreading rate (e.g. the vertical axis in Figure I.1) and u' is the peak value of the root mean square velocity fluctuations. Thus, one can write

$$M_t \approx f^* M_c. \tag{2.13}$$

As (2.13) and (2.12) indicate these three Mach numbers, M_g, M_c, and M_t, are nearly proportional to each other, and are also of the same order despite the fact that each can represent different physical aspects of the flow. For instance, the definitions of M_c and M_g both include the mean characteristics of the velocity field. However M_c corresponds to the mean velocity difference across the two streams, while M_g corresponds to the mean velocity difference across an inhomogenous shear layer (measured by the vorticity thickness). Nonetheless, the correlation of M_g and M_c can provide useful information, as in the case of the annular mixing-layer simulation [102]. Since M_c is defined based on the mean characteristics of the flow, it can be interpreted as the Mach number of the relative motion of the large eddies.

III

GOVERNING EQUATIONS AND LINEAR STABILITY ANALYSIS

While most stability analyses concur that in compressible mixing layers there is a reduction of growth rate with increasing convective Mach number [50, 103, 104], fundamental understanding of suppression is lacking. The present chapter aims to give a basis for a physical understanding of the KH instability under the influence of compressibility using linear stability analysis of a compressible mixing layer. We now present the three-dimensional, unsteady, compressible Navier-Stokes equations that form the basis of instability analysis. Effects of body forces are not included in this study. The conservation equations of mass, momentum, and energy are as follows:

$$\frac{\partial \rho}{\partial t} + \frac{\partial}{\partial x_j}(\rho u_j) = 0, \tag{3.1}$$

$$\frac{\partial}{\partial t}(\rho u_j) + \frac{\partial}{\partial x_k}(\rho u_j u_k) = -\frac{\partial\left(p\delta_{jk}\right)}{\partial x_k} + \frac{1}{Re_l}\frac{\partial \sigma_{jk}}{\partial x_k}, \tag{3.2}$$

$$\frac{\partial p}{\partial t} + u_j\frac{\partial p}{\partial x_j} = -\gamma p\frac{\partial u_k}{\partial x_k} + \frac{\gamma(\gamma-1)}{Re_l}\frac{\partial\left(\sigma_{jk}u_k\right)}{\partial x_j} + \frac{\gamma}{PrRe_l}\nabla^2(\frac{p}{\rho}), \tag{3.3}$$

where the thermodynamic pressure, p, is given by the ideal gas law

$$p = \rho RT, \tag{3.4}$$

and the viscous stress tensor σ_{ij} is given by the constitutive relation:

$$\sigma_{ij} = 2\mu S_{ij} + \left[\frac{2}{3}\left(\lambda - \mu\right)S_{kk}\right]\delta_{ij}, \tag{3.5}$$

where x_i are the Cartesian coordinates, u_i are the velocity components for i = 1-3 and time is denoted by t. The density and the dynamic pressure are ρ and p,

respectively. The specific heat ratio is $\gamma = c_p/c_v$. The coefficient of the dynamic viscosity, μ, is given by Sutherland's law, and λ is the second viscosity coefficient. S_{ij} is the rate of strain tensor given by

$$S_{ij} = \frac{1}{2}\left(\partial u_i/\partial x_j + \partial u_j/\partial x_i\right). \tag{3.6}$$

The relevant non-dimensional parameters are the Reynolds number, Re_l, and the Prandtl number, Pr, which are defined by

$$Re_l = \frac{\rho U l}{\mu}, \tag{3.7}$$

$$Pr = \frac{c_p \mu}{k}. \tag{3.8}$$

It is important to point out that the energy equation (3.3) is expressed in terms of pressure. These equations form the foundation of the linear stability analysis.

III.A. Linear Stability Analysis

We perform linear analysis for a general parallel streamline shear flows in which the flow of specific interest is a planar mixing layer. Our analysis is restricted to inviscid flow with no chemical reaction. The inflectional instability of the mixing layer provides the inviscid instability mechanism, and the only effect of viscosity is damping disturbance amplitudes [62]. It has been established that the viscous effects on the large-scale dynamics of the highly compressible free shear flows do not actively contribute to the instability mechanism [105, 106]. To capture the transient stages of instability evolution, we formulate the linear stability analysis as an initial value problem. This is a similar approach as the work of Prichett *et al* [107]; however, they were interested in understanding the magnetohydrodynamics instability

of compressible plasma.

Starting with equations (3.1)-(3.3) for a passive mixing layer flow, we take the initial pressure and the initial density to be uniform. Reynolds decomposition is applied to the instantaneous field. Although the flow is compressible, it has been established that at the linear limit, the difference between Favre and Reynolds averages is negligible in shear flows [101]. An arbitrary flow quantity is decomposed into base and perturbation components:

$$q = \bar{q} + q', \tag{3.9}$$

where $\bar{(.)}$ and $(.)'$ denote mean or background quantities and small disturbance or perturbation quantities, respectively. Since pressure across the interface between two streams is taken to be continuous, it can be adopted as the primary variable. Applying decomposition (3.9) to (3.1)-(3.3) renders the evolution equation of the base quantities as follows:

$$\frac{\partial \bar{\rho}}{\partial t} + \bar{u_j}\frac{\partial \bar{\rho}}{\partial x_j} = \bar{\rho}\frac{\partial \bar{u_j}}{\partial x_j}, \tag{3.10}$$

$$\frac{\partial \bar{u_j}}{\partial t} + \bar{u_k}\frac{\partial \bar{u_j}}{\partial x_k} = -\frac{1}{\bar{\rho}}\frac{\partial \bar{p}}{\partial x_j}, \tag{3.11}$$

$$\frac{\partial \bar{p}}{\partial t} + \bar{u_k}\frac{\partial \bar{p}}{\partial x_k} = -\gamma\bar{p}\frac{\partial \bar{u_k}}{\partial x_k}, \tag{3.12}$$

Assuming that the mean flow field only varies slowly in the streamwise (x_1) and spanwise (x_3) directions, the base velocity can be described by a parallel shear velocity profile as

$$\overline{u}_i = (U_1(x_2), 0, 0). \tag{3.13}$$

Therefore, $\overline{u}_{i,j} = S\delta_{i1}\delta_{2j}$, where S is the mean shear rate. A particular mean velocity of a hyperbolic tangent profile can be taken for the initial mean velocity field as

shown in IV.4. This implies that $\partial\bar{u}_i/\partial x_i = 0$ and $\partial\bar{p}/\partial x_i = 0$ [ref]. Thus, in the linear limit, we have:

$$\bar{\rho} \approx \bar{\rho}(x_1, x_2, x_3, 0) = \bar{\rho}_0; \quad \text{and} \quad \bar{p}(t) \approx \bar{p}(x_1, x_2, x_3, 0) = \bar{p}_0. \tag{3.14}$$

By subtracting the base flow from the instantaneous flow equations, the perturbation field evolution equations are obtained:

$$\frac{\partial \rho'}{\partial t} + U_1 \frac{\partial \rho'}{\partial x_1} = -\frac{\partial(\bar{\rho} u_k')}{\partial x_k}, \tag{3.15}$$

$$\frac{\partial u_1'}{\partial t} + U_1 \frac{\partial u_1'}{\partial x_1} = -u_2' \frac{\partial U_1}{\partial x_2} - \frac{1}{\bar{\rho}} \frac{\partial p'}{\partial x_1}, \tag{3.16}$$

$$\frac{\partial u_2'}{\partial t} + U_1 \frac{\partial u_2'}{\partial x_1} = -\frac{1}{\bar{\rho}} \frac{\partial p'}{\partial x_2}, \tag{3.17}$$

$$\frac{\partial u_3'}{\partial t} + U_1 \frac{\partial u_3'}{\partial x_1} = -\frac{1}{\bar{\rho}} \frac{\partial p'}{\partial x_3}, \tag{3.18}$$

$$\frac{\partial p'}{\partial t} + U_1 \frac{\partial p'}{\partial x_1} = -\gamma \frac{\partial(\bar{p} u_k')}{\partial x_k}. \tag{3.19}$$

Due to the nature of the initial base flow profile (3.13), the linearized velocity perturbation equations are expressed as given in (3.16)-(3.18). Having the perturbation field in place, we continue with our linear analysis. Differentiating (3.16) with respect to x_1, (3.17) with respect to x_2, and (3.18) with respect to x_3, we get

$$\frac{\partial}{\partial t}\left(\frac{\partial u_1'}{\partial x_1}\right) + U_1 \frac{\partial}{\partial x_1}\left(\frac{\partial u_1'}{\partial x_1}\right) = -\frac{1}{\bar{\rho}} \frac{\partial^2 p'}{\partial x_1^2} - \frac{\partial u_2'}{\partial x_1} S(x_2), \tag{3.20a}$$

$$\frac{\partial}{\partial t}\left(\frac{\partial u_2'}{\partial x_2}\right) + U_1 \frac{\partial}{\partial x_1}\left(\frac{\partial u_2'}{\partial x_2}\right) = -\frac{1}{\bar{\rho}} \frac{\partial^2 p'}{\partial x_2^2} - S(x_2) \frac{\partial u_2'}{\partial x_1}, \tag{3.20b}$$

$$\frac{\partial}{\partial t}\left(\frac{\partial u_3'}{\partial x_3}\right) + U_1 \frac{\partial}{\partial x_1}\left(\frac{\partial u_3'}{\partial x_3}\right) = -\frac{1}{\bar{\rho}} \frac{\partial^2 p'}{\partial x_3^2}, \tag{3.20c}$$

where the mean/background shear in the normal direction, $S(x_2)$, is given by

$$S(x_2) = \frac{\partial U_1}{\partial x_2}. \tag{3.21}$$

Adding the three equations above leads to

$$\frac{\partial}{\partial t}\left(\frac{\partial u_i'}{\partial x_i}\right) + U_1\frac{\partial}{\partial x_1}\left(\frac{\partial u_i'}{\partial x_i}\right) = -\frac{1}{\bar{\rho}}\frac{\partial^2 p'}{\partial x_i^2} - 2S(x_2)\frac{\partial u_2'}{\partial x_1}, \tag{3.22}$$

Since the aim is to express the pressure perturbation Laplacian in terms of pressure itself to the extent possible, the right-hand side of equation (3.22) are obtained from the energy equation (3.3). For the sake of simplicity, we refer to $S(x_2)$ as S hereafter. To construct the left-hand side of (3.22), the energy equation (3.3) is differentiated once with respect to t and once with respect to x_1, respectively, as follows:

$$\frac{\partial}{\partial t}\left(\frac{\partial u_i'}{\partial x_i}\right) = -\frac{1}{\gamma\bar{p}}\left(\frac{\partial^2 p'}{\partial t^2} + U_1\frac{\partial^2 p'}{\partial t\partial x_1}\right), \tag{3.23}$$

$$U_1\frac{\partial}{\partial x_1}\left(\frac{\partial u_i'}{\partial x_i}\right) = -\frac{U_1}{\gamma\bar{p}}\left(\frac{\partial^2 p'}{\partial t\partial x_1} + U_1\frac{\partial^2 p'}{\partial x_1^2}\right). \tag{3.24}$$

Substituting (3.23) and (3.24) into (3.22), the evolution of the pressure perturbation can be expressed in a hyperbolic form of

$$\frac{\partial^2 p'}{\partial x_i^2} + 2\bar{\rho}S\frac{\partial u_2'}{\partial x_1} = \frac{1}{\bar{a}^2}\left[\frac{\partial^2 p'}{\partial t^2} + 2U_1\frac{\partial^2 p'}{\partial t\partial x_1} + U_1^2\frac{\partial^2 p'}{\partial x_1^2}\right], \tag{3.25}$$

where $\bar{a} = \sqrt{\gamma\bar{p}/\bar{\rho}}$ is the speed of sound. Equation (3.25) expresses the evolution of the pressure perturbation in a very general sense of a mixing layer, which applies to either a compressible or an incompressible case. However, at the incompressible limit, the speed of sound is infinite. As $a \to \infty$, equation (3.25) can be reduced to an elliptic form of Poisson's equation for the pressure perturbation as follows:

$$\nabla^2 p' = \frac{\partial^2 p'}{\partial x_i^2} = -2S\bar{\rho}\frac{\partial u_2'}{\partial x_1}. \tag{3.26}$$

In this case, pressure is acting as a Lagrange multiplier, imposing only the incompressibility condition. In order to facilitate further analyses and to delineate the

behavior of the perturbation from the base field, we apply the Howarth-Dorodnitzn transformation [108]. In this transformation, the flow evolution is essentially described as a coordinate moving at the convective velocity of U_c, defined in (2.5). The advantage of working in this coordinate frame is the fact that velocity distributions remain the same in spite of having different initial Mach numbers at two streams. Taking the streamwise mean velocity as a convective velocity of the coordinate frame, the suggested transformation is given by

$$X_1 \equiv x_1 - \int_0^t U_1(X_2) d\xi, \tag{3.27a}$$

$$X_2 \equiv x_2, \tag{3.27b}$$

$$X_3 \equiv x_3, \tag{3.27c}$$

$$t \equiv t. \tag{3.27d}$$

Hence, the perturbation equations (3.15)-(3.19) can be rewritten in the new frame as follows:

$$\frac{\partial \rho'}{\partial t} = -\bar{\rho}\left[\frac{\partial u_1'}{\partial X_1} + \frac{\partial u_2'}{\partial X_2} - S^* + \frac{\partial u_3'}{\partial X_3}\right], \tag{3.28}$$

$$\frac{\partial u_1'}{\partial t} = -\frac{1}{\bar{\rho}}\frac{\partial p'}{\partial X_1} - u_2' S, \quad \frac{\partial u_2'}{\partial t} = -\frac{1}{\bar{\rho}}\frac{\partial p'}{\partial X_2} + \frac{1}{\bar{\rho}}\frac{\partial p'}{\partial X_1} S^*, \tag{3.29}$$

$$\frac{\partial u_3'}{\partial t} = -\frac{1}{\bar{\rho}}\frac{\partial p'}{\partial X_3}, \tag{3.30}$$

$$\frac{\partial p'}{\partial t} = -\gamma\bar{p}\left[\frac{\partial u_1'}{\partial X_1} + \frac{\partial u_2'}{\partial X_2} - S^* + \frac{\partial u_3'}{\partial X_3}\right], \tag{3.31}$$

where

$$S^* = S^*(X_2, t) = \int_0^t S(X_2) d\xi. \tag{3.32}$$

Alternatively, the pressure equation in a new coordinate frame can also be written

in the hyperbolic wave form starting from (3.25) as follows:

$$\frac{1}{\bar{a}^2}\frac{\partial^2 p'}{\partial t^2} - \frac{\partial^2 p'}{\partial X_i^2} = -2\bar{\rho}S\frac{\partial u_2'}{\partial X_1}. \tag{3.33}$$

Based on the assumption of the nearly-parallel mean field, the flow homogeneity in streamwise (x_1) and spanwise (x_3) direction, or in the new transformed coordinate systems, (X_1 and X_3), is consequently deduced. Such periodicity allows us to work in wavenumber space. Thus, we examine the behavior of a single Fourier mode of the wavevector of $\vec{\kappa} = \kappa_1\vec{\mathbf{e}_1} + \kappa_3\vec{\mathbf{e}_3}$, where κ_1 and κ_3 are the components of the wavenumber vector in the streamwise and spanwise directions, respectively. The modulus of the wavenumber vector is defined as $\kappa = \sqrt{\kappa_1^2 + \kappa_3^2}$.

In an initial value approach, we analyze temporal development of a small perturbation about its initial state [109]. Simple Fourier mode solutions to the equations (3.28)-(3.31) can be considered if we let the wave vector evolve in time [110, 111]. As the problem is periodic in the streamwise and spanwise directions, we can take a Fourier transformation in the variable X_1 and X_3. Therefore, the solution can be sought to be harmonic wavemodes, with an arbitrary initial profile in X_2 and t direction in the following form of

$$q' = \hat{q}(X_2, t)e^{i(\kappa_1 X_1 + \kappa_3 X_3)}, \tag{3.34}$$

where $i = \sqrt{-1}$ is the unit imaginary number, and $\hat{(\cdot)}$ represents the Fourier amplitude of a perturbation mode. Considering the perturbation array of $q' = (\rho', u_i', p')$ and the proposed solution form of (3.34), the Fourier transform of the perturbation field equations, (3.15)-(3.19), are obtained as follows

$$\frac{\partial \hat{\rho}}{\partial t} = -\bar{\rho}\left[i\kappa_1\hat{u_1} + \frac{\partial \hat{u_2}}{\partial X_2} - i\kappa_1\hat{u_2}S^* + i\kappa_3\hat{u_3}\right], \tag{3.35}$$

$$\frac{\partial \hat{u_1}}{\partial t} = -\frac{i}{\bar{\rho}}\kappa_1 \hat{p} - \hat{u_2} S, \tag{3.36}$$

$$\frac{\partial \hat{u_2}}{\partial t} = -\frac{1}{\bar{\rho}}\frac{\partial \hat{p}}{\partial X_2} - \frac{i}{\bar{\rho}}\kappa_1 \hat{p} S^*, \tag{3.37}$$

$$\frac{\partial \hat{u_3}}{\partial t} = -i\frac{\kappa_3}{\bar{\rho}}\hat{p} \tag{3.38}$$

$$\frac{\partial \hat{p}}{\partial t} = -\gamma \bar{p}\left[i\kappa_1 \hat{u_1} + \frac{\partial \hat{u_2}}{\partial X_2} - i\kappa_1 \hat{u_2} S^* + i\kappa_3 \hat{u_3} \right]. \tag{3.39}$$

To examine the compressibility effect manifesting via the role of pressure, we return to the hyperbolic equation (3.25). In similar fashion, using equations (3.36) -(3.39), we can obtain the evolution equation of the pressure perturbation, in the wavenumber space as follows:

$$\frac{\partial^2 \hat{p}}{\partial x_2^2} - (\kappa_1^2 + \kappa_3^2)\hat{p} + 2i\bar{\rho}\kappa_1 \hat{u_2} S = \frac{1}{a_0^2}\frac{\partial^2 \hat{p}}{\partial t^2}. \tag{3.40}$$

To highlight the influence of Mach number and the initial perturbation orientation in the pressure perturbation evolution (3.40), the following definitions are presented:

1. The *gradient Mach number*, M_g, corresponds to the shear rate across an appropriate length-scale, which is defined by

$$M_g \equiv \frac{Sl}{\bar{a}} = \frac{S}{\bar{a}\kappa}, \tag{3.41}$$

where the magnitude wavevenumber, κ, can be accounted as the related lengthscale, l.

2. The *obliqueness angle*, β, is a measure of the initial wavenumber vector with respect to the streamwise direction. The obliqueness angle is defined by

$$\beta \equiv \cos^{-1}\left(\frac{\kappa_1^0}{\kappa^0}\right), \tag{3.42}$$

where κ_1^0 and κ^0 are the initial value of the streamwise wave number and wavenumber magnitude, respectively. The orientation of the wavemode, oblique angle with respect

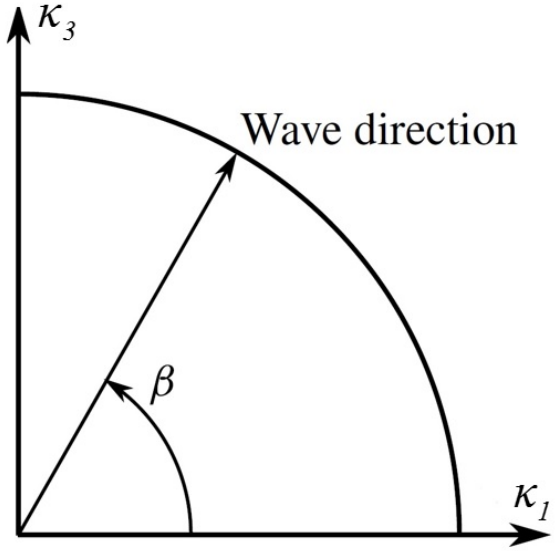

Figure III.1. Schematic representation of a typical oblique wavemode

to the streamwise direction on the κ_1-κ_3 plane is depicted in Figure. III.1. Based on this definition, the modes along the κ_1 direction are called streamwise modes ($\beta = 0$) while spanwise modes are along the κ_3 directions ($\beta = \pi/2$). For the oblique modes: $\beta \in (0, \pi/2)$. Using these two definitions and dividing by the magnitude of the wavenumber vector, κ^2, (3.40) can be rearranged to

$$\frac{1}{\kappa^2}\frac{\partial^2 \hat{p}}{\partial x_2^2} - \hat{p} + 2i\frac{\bar{\rho}}{\kappa}\hat{u}_2 S\cos\beta = M_g^2\cos^2\beta\frac{1}{S^2}\frac{\partial^2 \hat{p}}{\partial t^2}. \tag{3.43}$$

3. To focus on the compressibility effect more meticulously, we define a new parameter called the *effective gradient Mach number* which plays an important role in the interaction between flow dynamics, given by

$$M_g^* = M_g\cos\beta. \tag{3.44}$$

Normalized temporal and spatial coordinates are suggested as

$$t^* = St, \tag{3.45}$$

$$x^* = \kappa^0 x. \tag{3.46}$$

The normalized velocity, $\hat{u}_i^*$, and pressure amplitudes, $\hat{p}^*$, are given respectively by

$$\hat{u}_i^* \equiv \hat{u}_i/u^0, \quad \hat{p}^* \equiv \hat{p}/\overline{p}^0, \tag{3.47}$$

where u^0 is the r.m.s of the initial perturbation velocity and $\overline{p}$, is the initial background pressure. By taking the non-dimensionalizing temporal and spatial coordinates found in (3.45)-(3.46) and using (3.47) and (3.44), the equation (3.43) can be rewritten as

$$\frac{\partial^2 \hat{p}^*}{\partial x_2^{*2}} - \hat{p}^* + 2i\frac{u^0\bar{\rho}}{\kappa\bar{p}}\hat{u}_2^* S\cos\beta = M_g^{*2}\frac{\partial^2 \hat{p}^*}{\partial t^{*2}}, \tag{3.48}$$

Similarly, the velocity perturbation evolution can be expressed as

$$\frac{\partial^2 \hat{u}_2^*}{\partial x_2^{*2}} + (\hat{u}_2^* S^* - \hat{u}_1^*)S^* + \frac{i}{\kappa}\frac{\hat{p}^*}{\gamma u^0} S\cos\beta = M_g^{*2}\frac{\partial^2 \hat{u_2}}{\partial t^{*2}}. \tag{3.49}$$

To isolate the compressibility effect, mainly via the velocity-pressure interaction, based on the value of M_g^*, we consider three cases as follows:

I. Incompressible Case: At the incompressible limit, since $a \to \infty$, $M_g^* \to 0$, (3.48) is reduced to

$$\frac{\partial^2 \hat{p}}{\partial x_2^{*2}} - \hat{p} + 2i\frac{\bar{\rho}}{\kappa}\hat{u_2} S\cos\beta = 0. \tag{3.50}$$

Equation (3.50) is the Poisson's equation expressed in the wavenumber space, where the last term on the left-hand side acts as a source term.

II. Compressible Case with $\beta = \pi/2$: If the initial wavenumber vector is along the spanwise direction, then $\cos\beta = 0 \;\to\; M_g^* = 0$. Therefore, pressure evolves according to the reduced form of (3.48) given by

$$\frac{\partial^2 \hat{p}}{\partial x_2^{*2}} - \hat{p} = 0 \quad \Rightarrow \nabla p' = 0. \tag{3.51}$$

If the initial perturbations are spanwise modes, it is evident that pressure perturbation evolution is impervious to the value of $M_g^* = 0$. In other words, the thermodynamic pressure field is decoupled with the flow field. For the spanwise modes case with $\kappa_1 = 0$, the velocity perturbation field equations in (3.36)-(3.38) are reduced to

$$\frac{\partial \hat{u_1}}{\partial t} = -\hat{u_2} S, \tag{3.52}$$

$$\frac{\partial \hat{u_2}}{\partial t} = -\frac{1}{\bar{\rho}} \frac{\partial \hat{p}}{\partial X_2}, \tag{3.53}$$

$$\frac{\partial \hat{u_3}}{\partial t} = -i \frac{\kappa_3}{\bar{\rho}} \hat{p}, \tag{3.54}$$

Here, the velocity field experiences the least amount of compressibility effects. This implies that no matters what the initial convective Mach number is, the streamwise velocity perturbation grows linearly in a monotonical manner as indicated in (3.52). This extreme is called the pressure-release limit in literature [112]. Consequently, the turbulent kinetic energy evolution also follows the pressure-release limit.

III. Compressible Case with $0 \leq \beta < \pi/2$: Take an arbitrary initial perturbation mode at any obliqueness $\beta \in [0, \pi/2)$. Further manipulation on the equation (3.48) is carried out, since the (3.48) is not completely dimensionless. In order to do so, *only* in the compressible limit, the following normalization of the pressure is suggested

$$\hat{p}^{**} = \frac{\hat{p}}{\bar{\rho}\bar{a}^2}. \tag{3.55}$$

The pressure perturbation (3.48) can be rearranged. Thus, the velocity-pressure interaction is expressed by the inhomogeneous wave equation as:

$$\frac{\partial^2 \hat{p}^{**}}{\partial x_2^{*2}} - \hat{p}^{**} + 2iM_p \; M_g^* \hat{u}_2^* = M_g^{*2} \frac{\partial^2 \hat{p}^{**}}{\partial t^{*2}} \tag{3.56}$$

where the *perturbation Mach number* is defined by

$$M_p \equiv \frac{\hat{u}_2^0}{\bar{a}}, \tag{3.57}$$

M_p is similar in characteristics with turbulent Mach number, M_t in (2.10). The non-dimensional source term, $2iM_p\, M_g^* u_2^*$ in (3.56), contributes to the inhomogenous part of the wave equation. There particular solution to the wave equation (3.56) exits in the case of the large shear rate, S in the vicinity of the initial inflection point of the background velocity field. Whereas, in the top and bottom outer region, the general solution to the homogeneous part of (3.56) is more dominant. Regarding the compressibility parameters, it must be noted that the convective Mach number M_c is a of global measure of the mixing layer speed, while M_g is a local measure of the effect of compressibility on the perturbation of wavenumber κ.

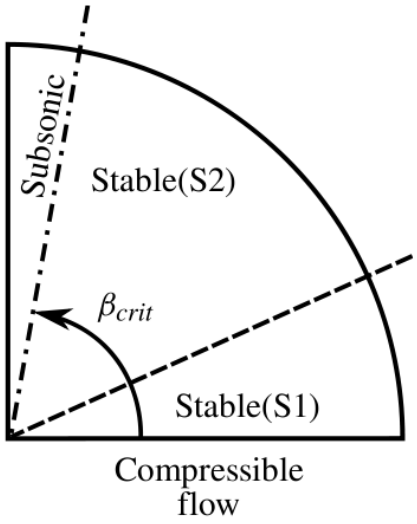

Figure III.2. Schematic of modal stability of incompressible and (b) compressible homogeneous shear flows

For homogeneous shear flows, detailed analysis has been performed in [113] lead-

ing to a clear explication of the velocity-pressure coupling and resulting reduction in kinetic energy growth. To delineate how compressibility affects the stability of homogeneous shear flows, their work has reached the following inferences: (i) streamwise modes ($\beta = 0$) experience the highest degree of compressibility effect, (ii) spaniwse modes ($\beta = \pi/2$) experience the least of compressibility effects, (iii) between $\beta = 0$ and $\pi/2$, there exists a critical angle, beyond which all modes expertise subsonic Mach numbers. Figure III.2 schematically shows these effects.

At the current stage of development, the stabilizing mechanism manifesting via p'-u_2' interactions, in homogeneous shear flow is reasonably well understood. A similar analysis of mixing layer geometry is rendered difficult due to the fact that inhomogeneity precludes many of the simplifying feature. Therefore, we examine the effect of compressibility on KH instability in Chapter V and mixing layers in ChapterVI using a combination of linear analysis and numerical simulations.

IV

NUMERICAL SCHEME FOR TEMPORAL MIXING LAYER SIMULATIONS

This chapter presents the details of the numerical scheme used for DNS. Numerical implementation of this scheme, initial conditions, boundary conditions and simulation parameters are discussed in detail. Validation studies of the numerical scheme are also provided.

IV.A. Numerical Scheme

Most of the current computational schemes are based on the Navier-Stokes equations, which represents momentum balance within an infinitesimal continuum control volume. However, applications involving high non-equilibrium conditions such those in astrophysical fluid dynamics, atmospheric re-entry, and hypersonic flights demand kinetic theory-based solvers (constructed based on the Boltzmann equation) that can offer significant advantages over the conventional Navier-Stokes solvers. The Boltzmann equation is potentially valid over a wide range of non-equilibrium conditions of relevance to high-speed flows. The Navier-Stokes based solvers are known to generate unrealistic flow physics, resulting in the numeric adverse effects. On the other hand, due to the dissociative nature of the kinetic theory-based schemes, they are able to capture the non-equilibrium effects, they may not be capable of resolving such adverse effects [114]. One of the key advantages of the kinetic theory-based formulation resides in a one-particle distribution function. To construct a numerical

scheme, it is more precise to apply the discritization to a fundamental quantity rather than derived continuum variables, such momentum and energy [115]. Based on the gas-kinetic theory, the Navier-Stokes equations can be derived (or recovered) from the Boltzmann equation using the Chapman-Enskog expansion [116,117]. Moreover, the simulation of a highly compressible flow with strong shock waves and extreme expansion waves requires a numerical scheme which offers both the robustness and accuracy [114,118–122].

The Gas-Kinetic Method (GKM) has gained popularity over the last decade, particularly in the context of compressible flow simulations [123–125], more specifically the type of GKM in which the Boltzmann equation collision term is expressed by a simplified kinetic collision model (e.g. the Bhatnagar-Gross-Krook (BGK) collision model [126]). The physical content of the BGK-GKM is far richer than Navier-Stokes solvers, especially in non-equilibrium flows [127,128].In this work, we carry out DNS using the GKM-BGK scheme. A brief description of this scheme is now presented.

IV.A.1. Gas-Kinetic Method

The DNS scheme used in this work is founded on the kinetic Boltzmann equation, which serves as the evolution equation of a single particle distribution function in phase-space. Considering a microscopic description of the flow, based on the particles' motion, macrospoic fluid variables can be defined as a statistical measure of particle behavior. For instance, fluid density can be defined as

$$\rho = \sum_i m n_i = \sum_i f(x_i, t, u_i, \xi_i), \tag{4.1}$$

where m is the molecular mass, and n_i is the number of particles moving at a specific velocity in the control volume. Due to the very large numbers of particles in a small fluid volume, the probability of particles of a certain velocity, mn_i is approximated by a continuous distribution function, $f(x_i, t, u_i)$, where the location of a particle with a velocity of u_i in space and time is denoted by (x_i, t). The internal motions among the molecules, such as rotation and vibration, are taken into account via the internal variable ξ_i, which may have different value in different Cartesian coordinates, x_i. At equilibrium, the internal variable ξ_i^2 is equal to $\xi_i^2 = \xi_1^2 + \xi_2^2 + ... + \xi_K^2$, where K is total number of degrees of freedom for a specific fluid. More information on the formulation of ξ_i can be found in [114]. Following the particles in the phase-space, the summation in (4.1) can be rewritten in integral form as follows:

$$\rho = \int f(x_i, t, u_i, \xi_i) d\Xi, \tag{4.2}$$

where $d\Xi = du_i d\xi$ is an elemental volume in an expanded, non-equilibrium phase-space. Similar to (4.2), the other macroscopic quantities can be expressed as the moments of the distribution function as follows:

$$\mathbf{Q} = \begin{pmatrix} \rho \\ \rho U_i \\ E \end{pmatrix} = \int \psi_\alpha f d\Xi, \quad \alpha = 1..5, \tag{4.3}$$

where the array of the macroscopic quantities $\mathbf{Q}$ includes U_i, the component of fluid velocity, and the total energy of fluid flow is given by $E = \frac{1}{2}\rho\left(U_i^2 + \frac{K+2}{2\lambda}\right)$, where λ is a function of temperature, T, molecular mass, m, and the Boltzmann constant, k_B, by the relation $\lambda = m/2k_BT$. The collision invariants, denoted by ψ_α can be

expressed as an array in the Cartesian coordinate frame as follows:

$$\psi_\alpha = (\psi_1, \psi_2, \psi_3, \psi_4, \psi_5)^T = \left(1, u_1, u_2, u_3, \frac{1}{2}\left(u_1^2 + u_2^2 + u_3^2 + \xi^2\right)\right)^T. \tag{4.4}$$

GKM is a finite-volume numerical scheme which combines both macroscopic and kinetic approaches. In GKM, we seek to solve the transport equations (3.1)-(3.3) to determine the array of the macroscopic quantities $\mathbf{Q}$. The kinetic part comes from the fact that the fluxes are calculated by taking moments of a particle distribution function,f. The central equation for GKM is:

$$\frac{\partial}{\partial t}\int_\forall \mathbf{Q}\, dx + \oint_A \vec{\mathbf{F}} \cdot d\vec{A} = 0, \tag{4.5}$$

where $\vec{F}$ is the flux through cell interfaces, $\vec{A}$. Equation (4.5) essentially corresponds to the Euler equation in the x-direction, which indicates conservation of a macroscopic flow quantity or $\mathbf{Q}$ within a control volume. Nonetheless, the algorithm of the GKM formulation can be decomposed into three stages:

(i) **Reconstruction of the Macroscopic Quantity, Q**: At this stage, the values of macroscopic variables at cell centers are interpolated to generate the cell-interface values. In this work, we use the weighted essentially non-oscillatory (WENO) scheme [**?**, 129], more specifically a 5^{th} order accuracy WENO. However, the implementation of any desired flux limiter is viable in our code.

(ii) **Flux Calculation**: The fluxes of the macroscopic quantities, $\mathbf{F}$, across cell interface are calculated by using the kinetic approach or better say evolution of moment. This step is the central part of GKM. The flux through a cell interface for a one-dimensional flow case is the following:

$$F_1 = [F_\rho, F_{\rho u_i}, F_E]^T = \int_{-\infty}^{\infty} u_i \psi_\alpha f(x_1, t, u_1, \xi) d\Xi, \tag{4.6}$$

where F_1 represents the flux calculation of mass, F_ρ, momentum , $F_{\rho u_i}$, and energy, F_E, calculated in the x direction. In a similar manner, fluxes in other directions can also be calculated.

(iii) **Update**: Having calculated fluxes using (4.6), the cell-centred macroscopic variables, $\mathbf{Q}$, can be updated using time-dependent fluxes in all three directions:

$$\begin{aligned}\mathbf{Q}_j^{n+1} - \mathbf{Q}_j^n = &\frac{1}{x_{1i+1/2,j,k} - x_{1i-1/2,j,k}} \int_{t^n}^{t^{n+1}} \left(\mathbf{F}_{1i+1/2,j,k}(t) - \mathbf{F}_{1i-1/2,j,k}(t)\right) dt \\ &+ \frac{1}{x_{2i,j+1/2,k} - x_{2i,j-1/2,k}} \int_{t^n}^{t^{n+1}} \left(\mathbf{F}_{2i,j+1/2,k}(t) - \mathbf{F}_{2i,j-1/2,k}(t)\right) dt \\ &+ \frac{1}{x_{3i,j,k+1/2} - x_{3i,j,k-1/2}} \int_{t^n}^{t^{n+1}} \left(\mathbf{F}_{3i,j,k+1/2}(t) - \mathbf{F}_{3i,j,k-1/2}(t)\right) dt,\end{aligned} \tag{4.7}$$

Equation (4.7) shows the macroscopic variable updates for a one-dimensional flow case. Here, n represents the number of the time step. To calculate the fluxes at the cell interface, the flow variables at the cell center must be interpolated to the cell interface. In this work, our scheme uses WENO as its flux limiter [130].

Starting with the **Flux Calculation** step, we need to determine f according to (4.6). Therefore, we consider the Boltzmann equation with the BGK model for its collision term, which has the form of

$$\frac{\partial f}{\partial t} + u_i \frac{\partial f}{\partial x_i} = \frac{(g - f)}{\tau}, \tag{4.8}$$

where a distribution function f, as a non-equilibrium state is approaching the distribution function g in the equilibrium state within the characteristic relaxation time of τ. The relaxation time can be interpreted as the time interval between collision. The

equilibrium state distribution is assumed to have a form of the Maxwell-Boltzmann distribution, which is given in three-dimensions as follows:

$$g = \rho \left(\frac{\lambda}{\pi}\right)^{(K+2)/2} \left(-\lambda(u_1-U_1)^2+(u_2-U_2)^2+(u_3-U_3)^2\right), \tag{4.9}$$

where (u_1, u_2, u_3) are the components of the *microscopic particle velocity*, and (U_1, U_2, V_3) are components of the *macroscopic flow velocity*. Equation (4.8) is a non-linear integro-differential equation. Applying (4.3) to calculate the macroscopic quantities, f appears in a non-linear manner in the definition of g. Assuming that collisions between particles are perfectly elastic, results in the conservation of mass, momentum and energy [131]. Thus, f and g satisfy the compatibility constraint give by

$$\int_0^{\Delta t} \int \psi_\alpha \frac{(g-f)}{\tau} dt d\Xi = 0, \quad \alpha = 1...5. \tag{4.10}$$

In our scheme, both the initial gas distribution function $f_0 = f(x_i, 0, u_i, \xi_i)$ and the equilibrium state g are evaluated based on the distribution of macroscopic flow variables [123]. With a local constant value for τ, the general solution to the BGK-GKM in (4.8) at a cell interface $x_{i+1/2}$ and time t is obtained by

$$\begin{aligned} f(x_{i+1/2,j,k}, t, \mathbf{u},) = \frac{1}{\tau} \int_0^t g(x'_{i,j,k}, t', \mathbf{u}, \xi) \\ e^{-(t-t')/\tau} dt' + e^{-t/\tau} f_0(x_{i+1/2,j,k} - \mathbf{u}t) dt', \end{aligned} \tag{4.11}$$

where $x_{\prime i,j,k}$ represents the particle trajectory given by $x'_1 = x_{i+1/2,j,k} - (t-t')\mathbf{u}$ and the microscopic velocity of a particle is denoted by $\mathbf{u} = (u_1, u_2, u_3)$. As a special case, one can assume that at time t_0, the initial gas distribution function f_0 is described independent of the spatial coordinates, according to (4.3), no quantity will macroscopically change in time and space. Then (4.11) can be reduced to

$$f(x_{i+1/2,j,k}, t) = \left(1 - e^{-(t-t_0)/\tau}\right) g + e^{-(t-t_0)/\tau} f(x_{i+1/2,j,k}, t_0) \tag{4.12}$$

Equation (4.12) clearly indicates that the initial distribution function, f_0, exponentially approaches the equilibrium distribution function, g, defined earlier in (4.9) within the characteristic relaxation time, τ. Either from 4.12 or 4.11, it is evident that the formal solution for f has two unknowns, f_0 and g. Besides determining these two unknowns, we also need to provide an expression for the collision time, τ. Applying the second-order of the Chapman-Enskog expansion [127], the BGK-GKM equation (4.8) can be rewritten as

$$\begin{aligned} f &= g + u_1 g_{,x_1} + u_2 g_{,x_2} + u_3 g_{,x_3} - \tau \left(u_1 g_{,x_1} + u_2 g_{,x_2} + u_3 g_{,x_2} + g_{,t} \right) \\ &= g(a + a x_1 + b x_2 + c x_3) - \tau (a u_1 + b u_2 + c u_3 + A), \end{aligned} \tag{4.13}$$

where $a = \partial g / \partial x_1$, $b = \partial g / \partial x_2$, $c = \partial g / \partial x_3$, and $A = \partial g / \partial t$. One can demonstrate the dependence of coefficients (a, b, c, A) on the particle velocities by performing a Taylor expansion about a Maxwellian with the form of

$$\begin{aligned} a &= a_0 + a_1 u_1 + a_2 u_2 + a_3 u_3 + \tfrac{1}{2} a_4 (u_1^2 + u_2^2 + u_3^2 + \xi^2) \\ &\cdots \\ &\cdots \\ A &= A_0 + A_1 u_1 + A_2 u_2 + A_3 u_3 + \tfrac{1}{2} A_4 (u_1^2 + u_2^2 + u_3^2 + \xi^2) \end{aligned} \tag{4.14}$$

For the sake of the notational simplicity, we set $x_{i+1/2,j,k} = 0$ and $t = 0$. Rewriting (4.13) at the cell interface and in a form of the piecewise function, f_0 at the left and right sides of the cell interface along the x_1 direction for instance) has the form of

$$f_0(x_1, x_2, x_3, 0) = \begin{cases} g^l \left[1 + a^l x_1 + b^l x_2 + c^l x_3 - \tau (a^l x_1 + b^l u_1 + c^l x_3 - A^l) \right], & x < 0; \\ g^r \left[1 + a^r x_1 + b^r x_2 + c^r x_3 - \tau (a^r x_1 + b^r u_1 + c^r x_3 - A^r) \right], & x \geq 0, \end{cases} \tag{4.15}$$

where the superscripts $(.)^l$ and $(.)^r$ indicate the left and right side of the cell interface, respectively. The equilibrium state g across a cell interface can be approximated by

$$g(x_1, x_2, x_3, t) = g_0 \left(1 + (1 - H[x])\, \bar{a}^l x_1 + H[x]\bar{a}^r x_1 + \bar{b}x_2 + \bar{c}x_3 + \bar{A}t)\right), \qquad (4.16)$$

were $H[x]$ is the Heaviside function. Substituting equations (4.15) and (4.16) into (4.11) and performing the integration, the gas distribution function f at a cell interface can be expressed as

$$\begin{aligned} f(x_{i+1/2,j,k}, \mathbf{u}, \xi) = &\left((1 - \bar{A}\tau)(1 - e^{-t/\tau}) + \bar{A}t\right) g_0 \\ &+ \left((t + \tau)e^{-t/\tau} - \tau\right) \left(\bar{a}^l u_1 H[u_1] + \bar{a}^r u_1 \left(1 - H[u_1]\right) + \bar{b}u_2 + \bar{c}u_3\right) g_0 \\ &+ e^{-t/\tau} \left(1 - (t + \tau)(a^l u_1 + b^l u_2 + c^l u_3) - \tau A^r\right) H[u] g^l \\ &+ e^{-t/\tau} \left(1 - (t + \tau)(a^r u_1 + b^r u_2 + c^r u_3) - \tau A^r\right) \left(1 - H[u]\right) g^r, \end{aligned} \qquad (4.17a)$$

Details of calculation of the coefficients (a, b, c, A) can be found in [114, 122, 123, 132]. To summarize, the overall flow chart of the scheme used for the DNSs of this work is depicted in Figure IV.1.

IV.B. Mixing Layer Simulations

Since we perform a temporal stability analysis in Chapter III, simulation of a temporally evolving mixing layer is applicable. A temporally developing mixing layer can be interpreted as an approximation of the evolution of a set of flow structures as they are convected downstream. Such an approximation of spatial correlations by temporal correlations is known by different names of the *frozen turbulence approximation* or *Taylor's hypothesis* or *Galilean transformation* [133]. However, it is demonstrated that the applicability of Taylor's hypothesis in shear flows is only

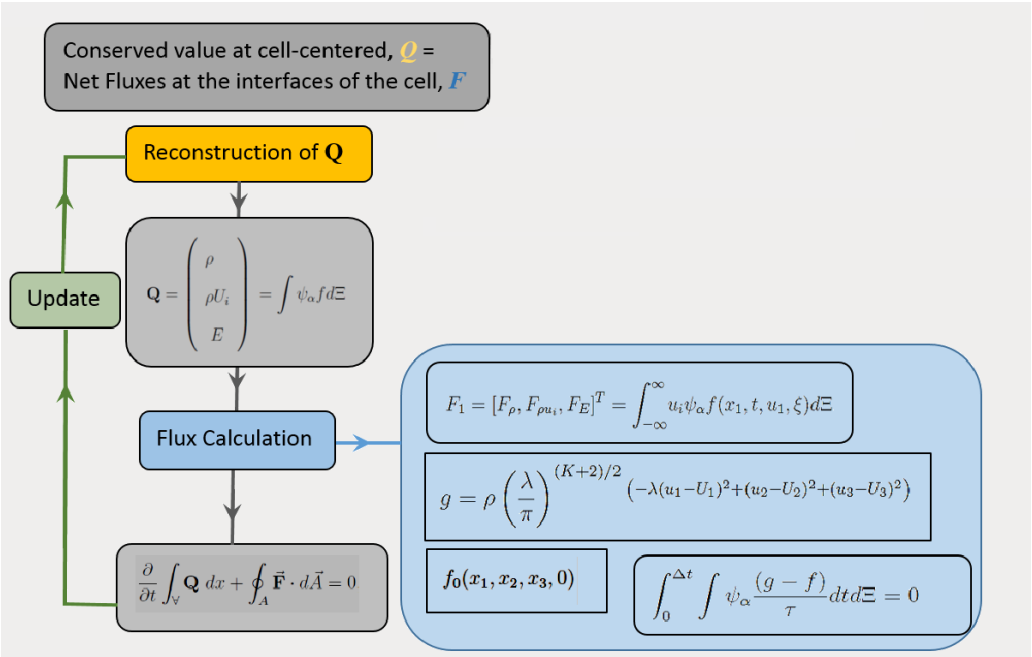

Figure IV.1. Flow chart describing GKM steps

valid if any single large-scale structure is not rapidly interacting with its adjacent structures [134].

In a temporal formulation, the spatial flow periodicity is enforced while allowing perturbation fields to evolve temporally. On that note, flows in nature and almost all experiments evolve spatially in time. Since the flow originates at a point in space, then an instability develops spatially downstream along the direction of mean velocity. The best way to explain the basic concept of these two formulations is to show the difference in the choice of coordinate. The schematic representation of the frame reference for both formulations is shown in Figure. IV.2. A spatially growing mixing layer, illustrated in Figure. IV.2 (a) is seen from a laboratory frame of reference. Whereas in a convective frame of reference, a reference frame is fixed to largescale structures travelling at U_c. A temporally evolving mixing layer is shown

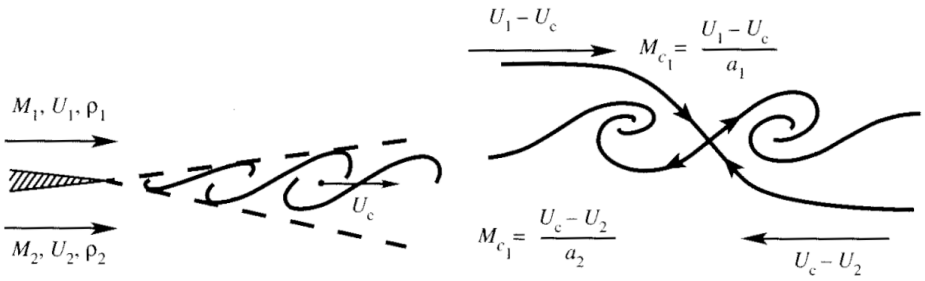

Figure IV.2. (a) spatial mixing layer in the laboratory frame of reference, (b) temporal mixing layer in the convective frame of reference

in Figure. IV.2 (b). In the convected frame of reference, there exists a saddle point between two adjacent eddies.

Speaking of the dynamical mechanism, spatially- and temporally-evolving mixing layers show similarities [135]. However, there is an argument for the validity of Taylor's hypothesis applicability to the flows involving largescale structures interactions. All largescale structures interactions such as pairing, merging, tearing, slippage may result in the absence of a global convective velocity, whereas Taylor's hypothesis requires a single convective velocity for the entire the flow to transform the coordinate frame [134]. Regarding the validity of Taylor's hypothesis applicability, there is another relevant work which compares the statistics of the spatial and temporal simulations of the decaying isotropic turbulence for different range of compressibility [136]. In terms of relating the spatial and temporal frames together, it was found that Taylor's hypothesis is valid for for solenoidal flow variables e.g. vorticity, therefore the computed statistics of incompressible turbulence statistics form the temporal and spatial simulations are in good agreement with the experimental

data. However, the Taylor's hypothesis may not be applicable for purely compressible motion: for instance the temporal and spatial correlations of the dilatation are not in agreement [136].

The applicability of Taylor's hypothesis is further discussed [137–139]: in the case of small turbulence intensity as the convection mean velocity is much larger than fluctuation fields in decayling isotropic flows [137]. Most works concur on the fact the Taylor's hypothesis is able to relate the temporal problem to the spatial problem correctly, at least in the qualitative sense, if the evolution of the shear layer is small compared to the evolution of the vortex size or large-scale interactions [134, 138].

Assuming an initial constant static pressure across the mixing layer, and considering the same specific heat ratio for both fluid flows, the *convective velocity*, U_c, is obtained by

$$U_c \equiv \frac{a_2 U_1 + a_1 U_2}{a_1 + a_2}, \tag{4.18}$$

where U_i and a_i refer to the mean velocities and speeds of sound, respectively. The advantages of a temporal simulation compared to the spatial one are: (i) relatively simple implementation of the boundary conditions by avoiding the requirement of imposing inflow-outflow condition, (ii) lower computational cost making it viable to implement, and (iii) smaller scales and higher Mach number cases examined in more detail, with more efficient codes, at higher resolutions.

However, time-developing schemes have their own disadvantages as well. The biggest drawback is the high level of uncertainty in initial conditions (more specifically in the case of fully turbulent initial set-up), which yields inconsistency in flow statistics measured by laboratory experiments. This may be accentuated by the fact

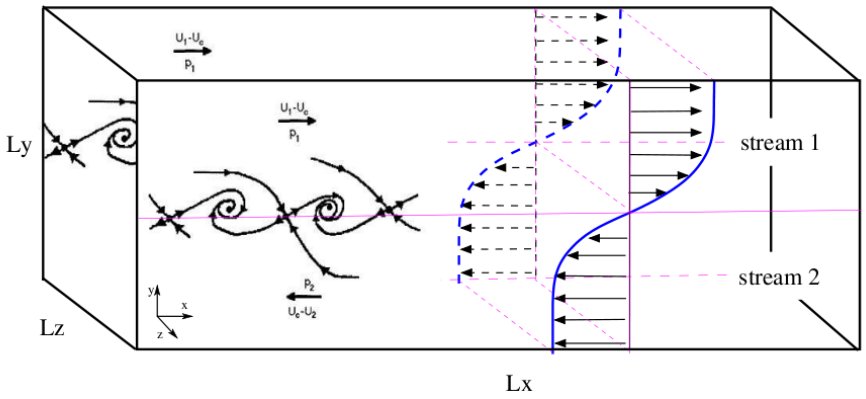

Figure IV.3. Schematic of the temporal mixing layer

that the frozen turbulence approximation is not accurate unless the velocity ratio of the spatial layers approaches unity [140].

In spite of the high demands on computational effort, several researchers have conducted DNS of spatially growing mixing layers [141–143]. The increase of the computing power over the last decade seems promising in overcoming this limitation. However, apart from computational effort, setting up the correct boundary conditions in spatially growing simulations that correspond to the exact experimental inflow and outflow conditions is challenging. Figure IV.3 shows the schematic of a temporal mixing layer. For more details on the initial velocity profile see § IV.B.3. The reference length-scale here is chosen as the initial vorticity thickness, δ_ω^0, defined by the ratio of the initial velocity difference between two streams and the maximum shear, $\delta_\omega^0 = \Delta U/(\frac{\partial u}{\partial y})_{max}$.

IV.B.1. Scheme Implementation

In a cubic geometry of $[0, L_{x_1}] \times [-\frac{1}{2}L_{x_2}, \frac{1}{2}L_{x_2}] \times [0, L_{x_3}]$, the fully compressible Navier-Stokes equations are solved. The length of the computational domain is set

equal to $l = 2\pi$. The box is discretized into $N_{x_1} \times N_{x_2} \times N_{x_3}$ elements along the x, y and, z directions, respectively. The upper stream has a velocity of $\Delta U/2$, and the lower stream has a velocity of $-\Delta U/2$. A sketch of the computational domain is shown in Figure IV.4. Based on the assumption of slow variation of density and

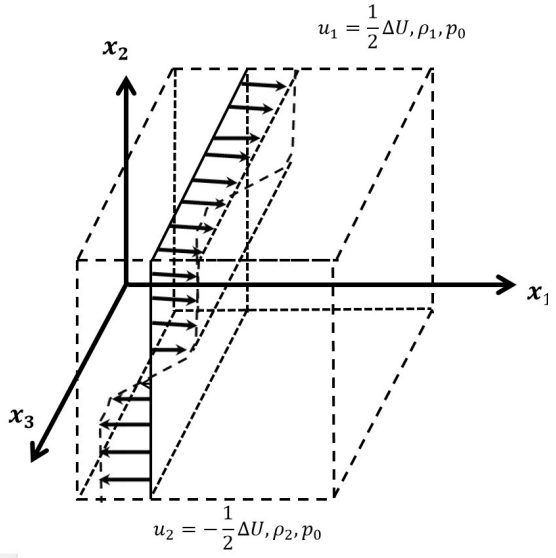

Figure IV.4. Schematic of the computational domain for the temporally evolving shear layer

pressure in the $x_1 - x_3$ plane in this analysis, the decomposition (3.9) can only be applied to the velocity field. Unlike the one-dimensional initial base field, the perturbation field is fully three-dimensional, given by

$$u_i' = (u_1', u_2', u_3'). \tag{4.19}$$

IV.B.2. Boundary Conditions

For both streamwise and spanwise directions, a periodic boundary condition is used. In order to simulate the farfield accurately in the cross-stream direction,

we would ideally prefer to resolve the equations on an infinite domain. A closer approximation to this would be to impose a *non-reflective* boundary condition in the normal direction. The basic idea of such a boundary condition, developed by Thompson [144], is to consider the free-slip mean field at the wall, while the cross-stream fluctuation field remains periodic.

IV.B.3. Initial Conditions

It is well-known that in a temporal mixing layer simulation, the transition to turbulence is very sensitive to the details of inflow disturbances [35, 145–147]. However, one of the advantages of numerical simulations over laboratory experiments is the ability to precisely specify these initial conditions. The action of the initial broadband perturbation is essentially nothing but the collective behavior of many individual wave modes. To avoid any ambiguity caused by different terms used by various researchers, the terminology for the initial perturbation modes is introduced as follows:

(i) Streamwise modes are the modes that are initially aligned along the downstream direction($\beta = 0$). The perturbation velocity is initialized by

$$(u_1', u_2', u_3') = (0, {u_2'}^0 \sin(\kappa_1 x_1 + \Delta), 0), \tag{4.20}$$

(ii) Spanwise modes are the modes that are initially aligned in the cross-stream direction with respect to the initial mean flow field ($\beta = \pi/2$). Thus, the initial solenoidal velocity perturbation used in DNS is given by:

$$(u_1', u_2', u_3') = (0, {u_2'}^0 \sin(\kappa_3 x_3 + \Delta), 0), \tag{4.21}$$

The velocity fields in both (4.20) and (4.21) are initially divergence-free with fluctuations along the direction of shear (x_2 direction).

(iii) The modes that are initially residing on the plane normal to the streamwise direction are called oblique modes ($0 < \beta < \pi/2$). Oblique modes combine characteristics of both spanwise and streamwise modes. The initial conditions for the fluctuating velocity field are given by:

$$(u_1', u_2', u_3') = (0, {u_2'}^0 \sin(\kappa_1 x_1 + \kappa_3 x_3 + \Delta), 0), \quad \Delta \in [0, \pi], \tag{4.22}$$

where $\Delta \in [0, \pi]$ is an arbitrary phase shift, and κ_1 and κ_3 are streamwise and spanwise wavenumbers, respectively. Figure.III.1 shows a typical oblique mode, which can be defined in the $\kappa_1 - \kappa_3$ plane. The initial turbulence intensity can be set by adjusting the amplitude of the initial sinusoidal wave, ${u_2'}^0$. In all the initial modes considered (4.20)-(4.22), u_1^0 and u_3^0 are taken to be zero. This is due to the fact that these components do not contribute to the instability.

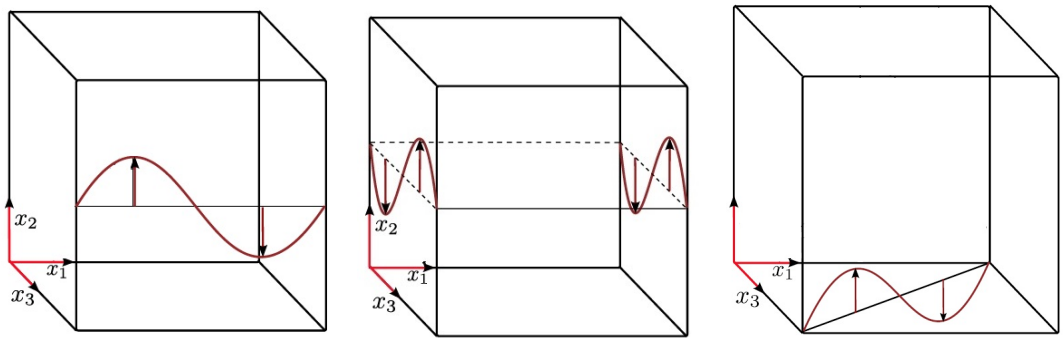

Figure IV.5. Schematic diagrams (not to scale) of the initial perturbation mode within the computational domain: (a) streamwise, (b) spanwise, and (c)oblique wave modes

Figure.IV.6 exhibits these three classes of modes in a computational domain. In the literature, streamwise modes have been referred to as azimuthal or two-dimensional. Due to the lack of clarity, the term *three dimensionality* has been associated to the oblique modes. It was assumed that the oblique were the only modes responsible for the generation of small-scale structures or three dimensionality; for instance in the work of Metcalfe *et al* [76], where a summation of two streamwise modes (a fundamental mode and its subharmonic) and one spanwise mode was used. Until the work of Sandham and Reynolds [34], the term of obliqueness had seldom been used in the literature. The amplitude of perturbation modes in many prior investigations has been chosen as the most unstable eigenfunctions of the linear Orr-Sommerfeld equations for a given wavenumber. Most work done in area of the compressible flows instability has adopted an eginevalue problem approach, similar to what has been the trend in the area of incompressible instability. However, we formulate the instability of a compressible mixing layer as an initial value problem. Based on this approach, we analyze the temporal evolution of a small perturbation about its initial value.

The inflectional instability of the mixing layer provides an inviscid instability mechanism [63, 98]. In the current numerical simulations, the mean velocity is initialized by a hyperbolic tangent profile for the streamwise velocity, $u(y)$, while all other mean velocity components are set to zero. Thus,

$$(\bar{u}_1, \bar{u}_2, \bar{u}_3) = (\frac{\Delta U}{2} \tanh\left(-\frac{x_2}{2\delta_m^0}, 0, 0\right), \tag{4.23}$$

where δ_m^0 is the half of the initial mixing layer thickness. The desired convective Mach is achieved by changing the initial mean velocity, $\Delta U/2$, accordingly.

IV.B.4. Simulation Parameters

The density ratio between two streams is specified to unity. The mean pressure is set to a uniform value, p_0. The initial temperature for all the cases is $T_0 = 300$. The initial momentum thickness Reynolds number is fixed to $Re^0_{\delta_m} = 400$ for all cases at different initial convective Mach numbers. The Prandtl number is set to $Pr = 0.7$. In the current simulations, air is used as the working fluid, thus, the Gas constant is $R = 287\ (J/KgK)$ and the specific heat ratio is $\gamma = 1.4$.

IV.C. Validation Studies

A comprehensive validation of GKM has been conducted in the context of a variety of homogeneous shear flows such as decaying isotropic flows, where linear and non-linear flow features are independently verified and validated against asymptotic Rapid Distortion Theory (RDT); DNS results [113, 148]; in wall-bounded flows [149] and the Lattice Boltzmann Method (LBM) [124]. To validate GKM for temporal mixing layer simulations, we compare current DNS results against previous DNS data by Sandham and Reynolds [34], Pantano and Sarkar [2], and experimental data from Elliot and Samimy [67].

IV.C.1. Validation for Stability Simulations

To validate our scheme against the spectral scheme used in DNS by Sandham and Reynolds [34], in addition to the mean velocity profile given in (4.23), two different types of initial perturbation fields are tested : (i) the streamwise perturbation mode similar to (4.20) but for all velocity components and (ii) a combination of the

streamwise mode and a pair of oblique waves with the obliqueness angle of $\beta = \pi/4$ given by

$$u' = u'^0_{2d} \sin(x_1) + u'^0_{pair} \sin(x_1 + x_3), \tag{4.24}$$

where u'^0_{2d} and u'^0_{pair} are the initial perturbation amplitudes of the streamwise mode and a pair-mode set to match the initial values in the DNS of Sandham and Reynolds [34]. The variation of the kinetic energy as a function of normalized time at different Mach numbers is compared in Figure.IV.7. The growth trend at two different Mach numbers agree well with their DNS results. At later times, at higher Mach number, the oblique waves have an energy content that is almost two orders of magnitude higher than the streamwise waves do. This may be related to the difference in numerical methods, and more specifically, initial conditions. At lower Mach numbers, the oblique waves are more amplified than the two-dimensional (streamwise) waves.

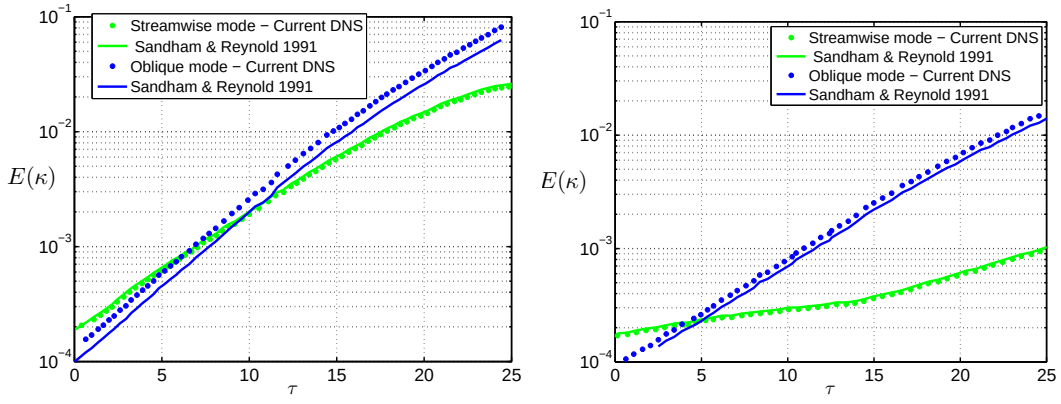

Figure IV.6. Temporal evolution of the turbulent kinetic energy at M_c =(a) 0.8 and (b) 1.05.

IV.C.2. Validation for Turbulence Simulations

To validate our scheme for a collection of perturbation modes, we compare present DNS against that of Pantano and Sarkar [2]. The energy spectrum of these perturbations, which are random, initially divergence-free and isotropic, can be given by

$$E(\kappa) = Ae^{-B(\kappa/\kappa_0)^2}, \tag{4.25}$$

where κ is the wavenumber, and the constant A is chosen such that the initial turbulent intensity of 10% is attained. The constant B and the initial wavenumber κ_0 are set such that the desired initial peak wavelengths are obtained. The temporal evolution of the normalized momentum thickness at different convective Mach numbers is compared against the DNS results of Pantano and Sarkar in Figure IV.8. Furthermore, the comparison of the turbulence profile in terms of the r.m.s. of velocity and the Reynolds shear stress along the normal direction is shown in Figure IV.9. These results are also compared with experimental data [67]. The agreement is again reasonably good.

Table IV.1. Parameters for the validation simulations

Case	M_c	s	$Re_{\delta^0_\omega}$	Pr_0	δ^0_m	$N_x \times N_y \times N_z$
V1	0.8	1.0	380	0.7	0.25	$128 \times 256 \times 128$
V2	1.05	1.0	380	0.7	0.25	$128 \times 256 \times 128$
V3	0.3	1.0	640	0.7	0.25	$256 \times 512 \times 128$
V4	0.7	1.0	640	0.7	0.25	$256 \times 256 \times 128$
V5	1.2	1.0	640	0.7	0.25	$256 \times 512 \times 128$

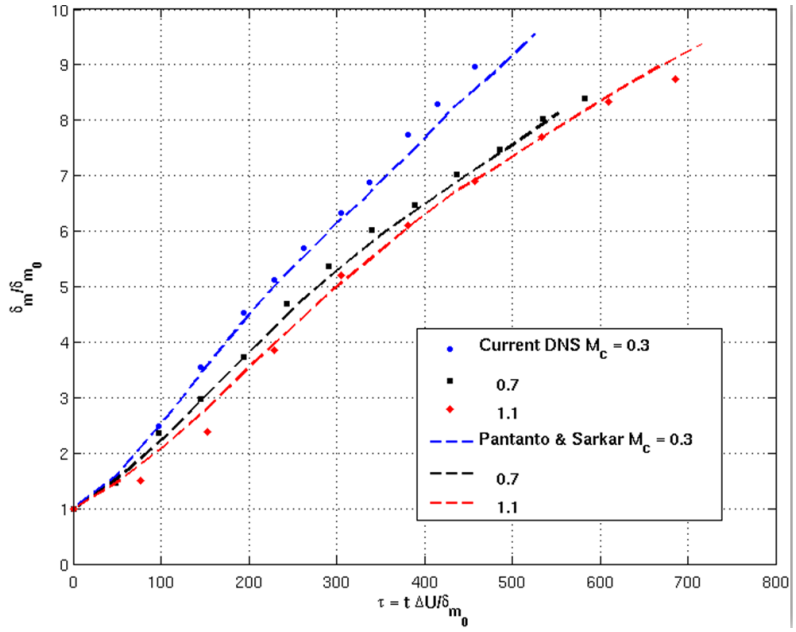

Figure IV.7. Time evolution of the normalized momentum thickness. Dash-dot lines correspond to the DNS results.

IV.C.3. Convergence Study

In order to validate the scheme and establish the accuracy of the results, several simulations are performed to examine the effects of the grid resolution and time-step size. All simulations are performed at Reynolds number, $Re = 400$, and Prandtl number, $Pr = 0.7$. Table IV.2 lists the grid sizes and the corresponding parameters of these simulations. The evolution of the normalized turbulent kinetic energy for different resolutions is shown in Figure IV.10. The time-step convergence study is presented in Figure IV.11, where the different simulations with different time-step are carried out for the resolution of $256N_{x_1} \times 512N_{x_2} \times 128N_{x_3}$. Both grid convergence and time-step convergence demonstrated in Figures IV.10 and IV.11 are performed for the compressible mixing layer case of $M_c = 1.2$. The streamwise initial velocity perturbation is of the form of $\vec{u'} = (0, u'_2(0)\sin(x_1), 0)$, with initial

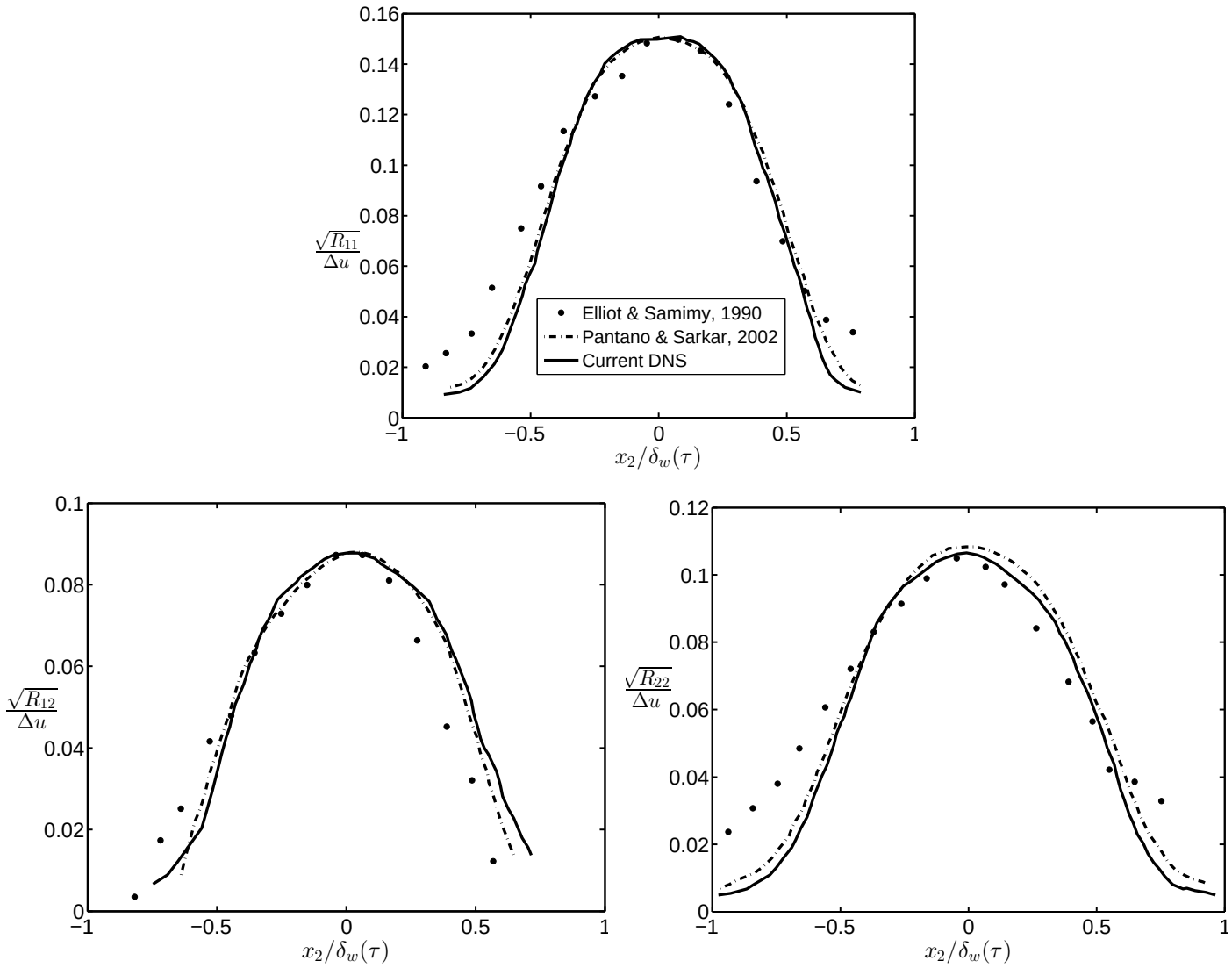

Figure IV.8. (a) Streamwise, (b) cross-stream r.m.s. velocity, and (c) the Reynolds shear stress along the normal direction in compressible mixing layer at $M_c = 0.7$. Symbols correspond to experimental data at $M_c = 0.64$, whereas dash-dot lines correspond to the DNS results at $M_c = 0.7$.

turbulent intensity set to 7%. Clearly converged results are obtained for grids finer than $256N_{x_1} \times 512N_{x_2} \times 128N_{x_3}$ and time-steps smaller than 1×10^{-5} units.

Table IV.2. Simulations parameters for grid convergence studies

Case	M_c	β	δ_m^0	$N_{x_1} \times N_{x_2} \times N_{x_3}$
G1	1.2	0	0.25	$256 \times 512 \times 128$
G2	1.2	0	0.25	$256 \times 512 \times 256$
G3	1.2	0	0.25	$1025 \times 256 \times 256$
G4	1.2	0	0.25	$1025 \times 512 \times 128$

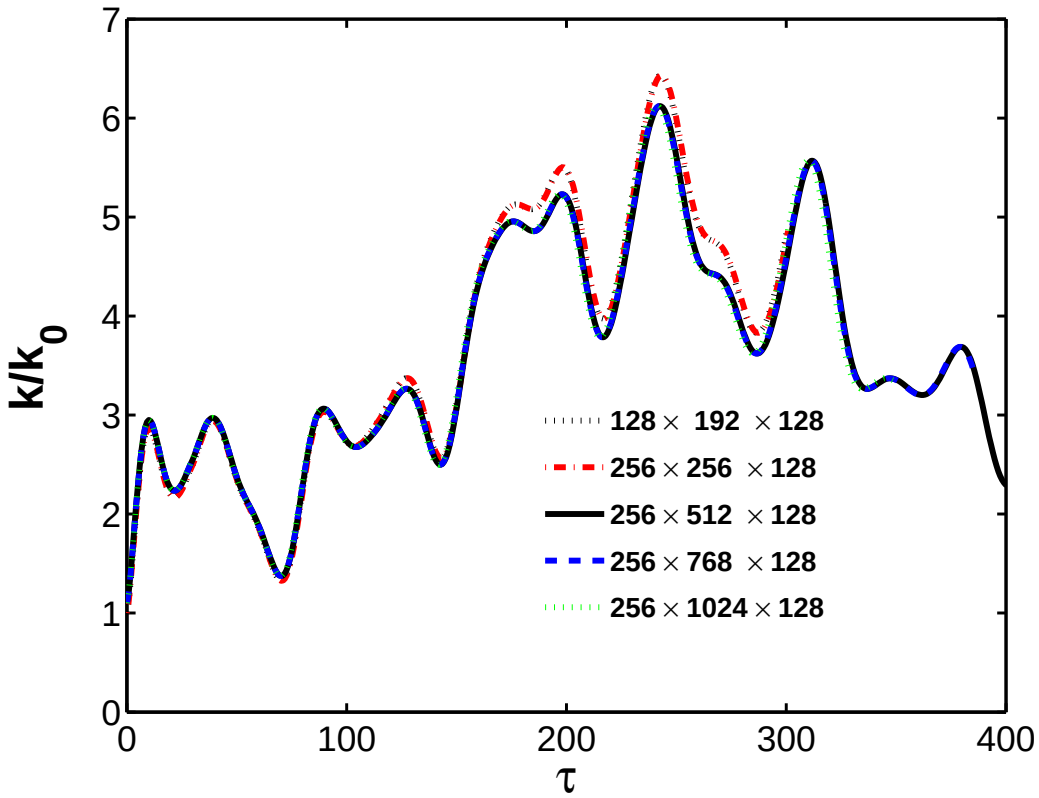

Figure IV.9. Temporal evolution of the normalized turbulent kinetic energy for different resolution of $N_{x_1} \times N_{x_2} \times N_{x_3}$ and the fixed time-step of $\Delta t = 10^{-5}$.

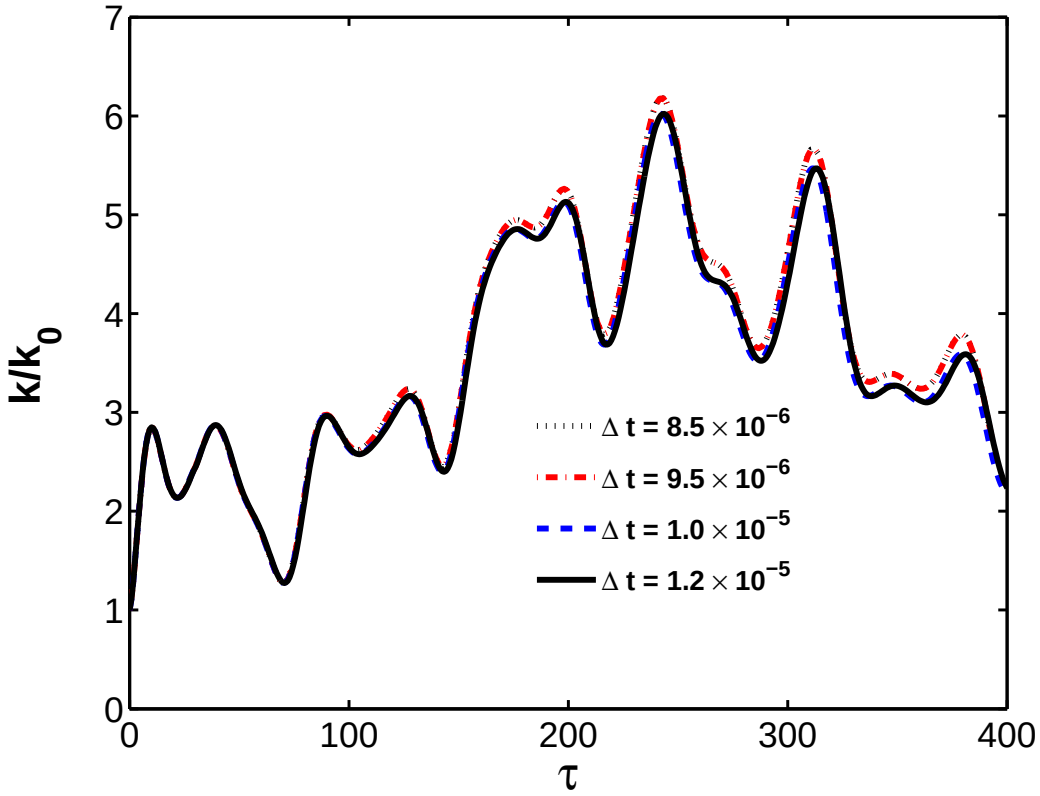

Figure IV.10. Temporal evolution of the normalized turbulent kinetic energy for different time-step of Δt for the simulations in the computational domain with the fixed resolution of $256N_{x_1} \times 512N_{x_2} \times 128N_{x_3}$.

V

EFFECT OF COMPRESSIBILITY ON KELVIN-HELMHOLTZ INSTABILITY

The objective of the chapter is to explicate the key compressibility mechanism responsible for the KH instability suppression employing linear analysis and numerical simulations First, we complete the linear analysis, introduced in Chapter III to examine KH instability under the influence of compressibility. Then we employ the results of the numerical simulations of a temporally evolving mixing layer at different initial convective Mach numbers to develop a more comprehensive understanding. Finally, the physics of compressible KH instability evolution will be compared and contrasted against the KH instability in incompressible flows.

V.A. Linear Analysis

Since KH instability is an inviscid instability driven by the inflection point [63, 98, 150], it suffices to consider the inviscid linear perturbation equations [46]. We commence our linear analysis from Chapter III. It is established that (i) the normal component of velocity perturbation, u_2', plays an important role in the evolution of perturbation kinetic energy and spanwise vorticity, and (ii) changes in pressure-velocity interaction and the consequent effect on spanwise vorticity (and kinetic energy) Classical KH instability involves only planar (streamwise) perturbations.

Therefore, we set $\beta = 0$

$$\frac{\partial^2 \hat{u}_2^*}{\partial x_2^{*2}} + (\hat{u}_2^* S^* - \hat{u}_1^*) S^* + \frac{i}{\kappa} \frac{\hat{p}^*}{\gamma u^0} S = M_g^2 \frac{\partial^2 \hat{u}_2^*}{\partial t^{*2}}, \tag{5.1}$$

$$\frac{\partial^2 \hat{p}^*}{\partial x_2^{*2}} - \hat{p}^* + 2i \frac{u^0 \bar{\rho}}{\kappa \bar{p}} \hat{u}_2^* S = M_g^2 \frac{\partial^2 \hat{p}^*}{\partial t^{*2}}, \tag{5.2}$$

where the normalized independent variables as follows: $t^* \equiv St$ and $x_2^* \equiv \kappa X_2$, and κ is the magnitude of the wavenumber vector. The normalized velocity and pressure amplitudes are: $\hat{p}^* \equiv \hat{p}/\overline{p}$ and $\hat{u}_i^* \equiv \hat{u}_i/u^0$, respectively where u^0 is the r.m.s of the initial perturbation velocity. Recall that the gradient Mach number, is defined by

$$M_g \equiv \frac{S}{\bar{a_0} \kappa}, \tag{5.3}$$

where $\bar{a_0} = \sqrt{\gamma \bar{p}/\bar{\rho}}$ is speed of sound, S is the background shear rate and κ is the magnitude of the wavenumber vector. From the form of the equations (5.1)-(5.2), it is evident that the M_g is the relevant Mach number to characterize compressibility effects on the perturbation field. It is crucial to point out that M_g is a local measure of the effect of compressibility on the perturbation of wavenumber κ, while the convective Mach number, M_c, is a global measure of the mixing layer speed. Based on the value of M_g, effect of compressibility on KH instability can be classified as follows:

1. At the incompressible limit, $\bar{a} \to \infty$, then $M_g \to 0$, the hyperbolic equation expressing the evolution of the pressure perturbation, (5.2) is reduced to an elliptic form of

$$\frac{\partial^2 \hat{p}^*}{\partial x_2^{*2}} - \hat{p}^* = -2i \frac{u^0 \bar{\rho}}{\kappa \bar{p}} \hat{u}_2^* S. \tag{5.4}$$

This is indeed the Poisson's equation for the pressure and leads to the familiar KH behavior [98]. Nonetheless, due to a smaller value of the shear rate, the source term

is relatively weak at low-Mach number flows. At the incompressible limit, pressure has the sole purpose of imposing the divergence-free constraint on the velocity field.

2. At higher speeds ($M_g > 0$), the full form of hyperbolic wave equations (5.1)-(5.2) govern the evolution of velocity and pressure perturbations. In this limit, pressure is a true thermodynamic variable with evolution governed by an inhomogeneous wave equation given in (5.2) with a propagation speed of $1/M_g$ in the normal direction. It is well established in literature that KH is severely suppressed [1,49,98]. While the transformative influence of compressibility is known, the precise mechanism of suppression and its connection to wave behavior of p' and u_2' needs to be formally established and understood. We now explicate the suppression mechanism by combining the above linear analysis with findings from numerical simulations.

V.B. Direct Numerical Simulations

To examine KH instability in compressible flows and to contrast the KH dynamics at low and high Mach numbers, we perform DNS of a temporally evolving mixing layer. The numerical scheme employs the GKM, introduced in Chapter IV, which effectively solves the full Navier-Stokes equations with all non-linear and viscous physics completely intact. The background velocity field is taken to be $\overline{u}_i = (\Delta U/2 \tanh(x_2/(2\delta_m^0), 0, 0)$, where δ_m^0 is the initial momentum thickness of the mixing layer, is the the velocity difference between two streams farfield. Only streamwise perturbations corresponding to the classical KH instability are considered in this chapter. Isolating the effect of only a single perturbation mode rather than the broadband perturbation helps us to scrutinize the evolution of KH instability

development more comprehensively. Even at very high speeds, it is evident from Chapter III that high wavenumber perturbations ($\kappa > S/\bar{a_0}$) experience subsonic gradient Mach numbers. Therefore, low wavenumber or large wavelength initial velocity perturbation field is chosen: $u_i' = (0, \hat{u}_2^0 \sin(\kappa_1 x_1), 0); \kappa_1 = 2\pi/L = 1,\ 2,$ where L is the domain length and $\hat{u}_2^0 = 0.05\Delta U$. A thorough numerical convergence study, presented in section IV.C.1 confirms that a cubical domain of side $L = 2\pi$ with $256 \times 512 \times 128$ grid points provides results of requisite accuracy. Table V.1 describes the simulation parameters.

Table V.1. Initial physical and numerical parameters for the KH instability simulations

Case	M_c	s	$Re_{\delta_\omega^0}$	κ_1	δ_m^0	$N_x \times N_y \times N_z$
C1	0.3	1.0	395	1.0	0.25	$256 \times 1024 \times 256$
C2	0.4	1.0	395	1.0	0.25	$256 \times 512 \times 256$
C3	0.6	1.0	395	1.0	0.25	$256 \times 512 \times 128$
C4	0.7	1.0	400	1.0	0.25	$256 \times 512 \times 128$
C5	0.8	1.0	400	1.0	0.25	$256 \times 512 \times 128$
C6	0.9	1.0	400	1.0	0.25	$256 \times 512 \times 128$
C7	1.0	1.0	400	1.0	0.25	$256 \times 512 \times 128$
C8	1.1	1.0	400	1.0	0.25	$256 \times 512 \times 128$
C9	1.2	1.0	400	1.0	0.25	$256 \times 512 \times 128$
C10	0.3	12.0	400	2.0	0.25	$256 \times 512 \times 128$
C11	0.7	1.0	400	2.0	0.25	$256 \times 512 \times 128$
C12	1.2	1.0	400	2.0	0.25	$256 \times 512 \times 128$

To closely examine the dynamics of the KH instability as Mach number increases, mixing layers of different convective Mach numbers are computed: $M_c =$ 0.3, 0.6, 0.8, 1.0 , 1.1 & 1.2. The initial is varied based on the initial M_c. It must be noted that the convective Mach number M_c is a of global measure of the mixing layer speed, while M_g is a local measure of the effect of compressibility on the

perturbation of wavenumber κ. The thermodynamic fields are initially taken to be uniform: temperature ratio and the density ratio between two streams, $s = \rho_2/\rho_1$, are initially of unity. The simulations are carried out for the air $\gamma = 1.4$ and initially uniform density of unity, $\bar{\rho}_0 = 1$ $(N.m^2)$. The initial Reynolds number based on the momentum thickness and Prandtl numbers are $Re_{\delta_m^0} = 400$ and $Pr = 0.7$, respectively.

Specification of boundary conditions is detailed in Chapter IV. Various features of the flow conditions including the hyperbolic tangent profile for the background streamwise velocity $\bar{u}_1^0(x_2)$ and the sinusoidal wave for the initial streamwise perturbation mode ${u'_2}^0(x_1)$ are exhibited in Fig. V.1. Note the locations of the three points in Fig. V.1 that are marked by S_1, S_2 and the initial inflection point of the background velocity marked by P. The streamwise and normal directions are denoted by x_1 and x_2, respectively.

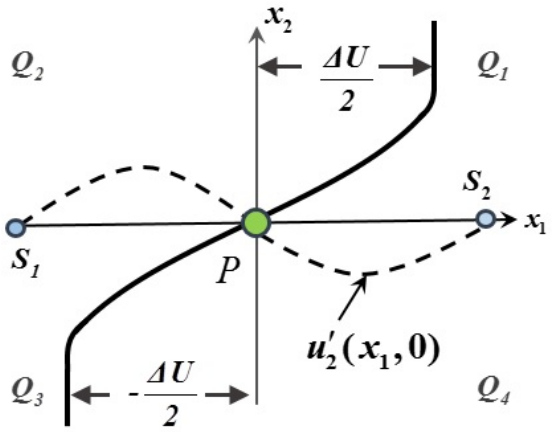

Figure V.1. A schematic representation of the flow conditions and computational geometry of a mixing layer initialized to a hyperbolic tangent profile for the mean velocity as $\bar{u} = (\Delta U/2 \tanh(x_2/\delta_m^0), 0, 0)$; initial velocity perturbation field of $u'_i = (0, \hat{u}_2^0 \sin(\kappa_1 x_1), 0)$; pivot point P; stagnation points S_1, S_2; and quadrants marked by $Q_1 - Q_4$.

V.B.1. Mixing Metrics

The extent of KH instability can be characterized in terms of the following mixing metrics: (i) momentum thickness, (ii) the turbulent kinetic energy, (iii) the normal-component of velocity, and (iv) vorticity thickness; additionally to characterize the degree of the KH instability development, the evolution of two more quantities are investigated: (v) enstrophy and (vi) circulation. The temporal evolution of all statistics are shown in normalized time defined by

$$\tau = \frac{\Delta U/2}{\delta_m^0} t. \tag{5.5}$$

All mixing metrics are non-dimensionalized in the conventional way by its initial value, except circulation which is non-dimensionalized by the initial characteristic velocity ($\Delta U/2$) and the initial characteristic shear layer thickness (δ_m^0). The definition of each mixing metric as follows:

1. Spreading rate can be one of the indicators of the mixing layer growth. This work considers characterizing the spreading rate both in terms of the *momentum thickness*, δ_m, and *vorticity thickness*, δ_ω. Additionally, instability growth can be measured in terms of the turbulent kinetic energy, $k = (\overline{u_i' \cdot u_i'})/2$. The momentum thickness is defined by

$$\delta_m(t) = \frac{1}{\bar{\rho}_0 \Delta U^2} \int_{-\infty}^{\infty} \bar{\rho}(\frac{1}{4}\Delta U^2 - u_1^2) dx_2. \tag{5.6}$$

The vorticity thickness is defined by

$$\delta_\omega(t) = \frac{\Delta U}{(\partial \bar{u}_1/\partial x_2)_{max}}, \tag{5.7}$$

where $(\partial \bar{u}_1/\partial x_2)_{max}$ occurs at the inflection point, marked by P in Figure V.1. Momentum thickness or vorticity thickness can be related to each other. The correlation

between them depends on the initial values of the convective Mach number and the velocity ratio between two streams [2]. The temporal evolution of the momentum thickness and the vorticity thickness for different initial M_c is presented in Figure V.2. The temporal evolution of turbulent kinetic energy, k, along with its important normal component, $\overline{u_2'u_2'}$ is presented in Figure V.3. The turbulent kinetic energy evolves nearly monotonically until it saturates, as shown in Figure V.3 (a). The maximum growth is observed at the lowest initial M_c (0.3). Normal component of velocity u_2' follows the same trend of evolution as does that of k, expect within the very early stage of evolution. For both k and $\overline{u_2'u_2'}$, the energy growth is suppressed at the higher M_c.

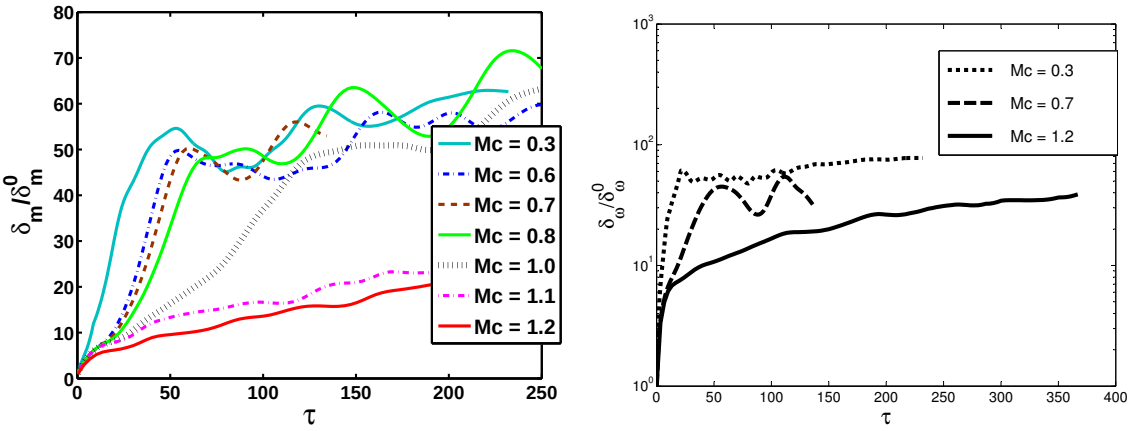

(a) (b)

Figure V.2. Temporal evolution of the normalized (a) momentum thickness and (b) vorticity thickness at different Mach numbers when the initial obliqueness angle is zero, β=0.

2. Enstrophy. To understand how flow structures are affected by compressibility, we can exploit other properties of velocity field such as vorticity. In this context,

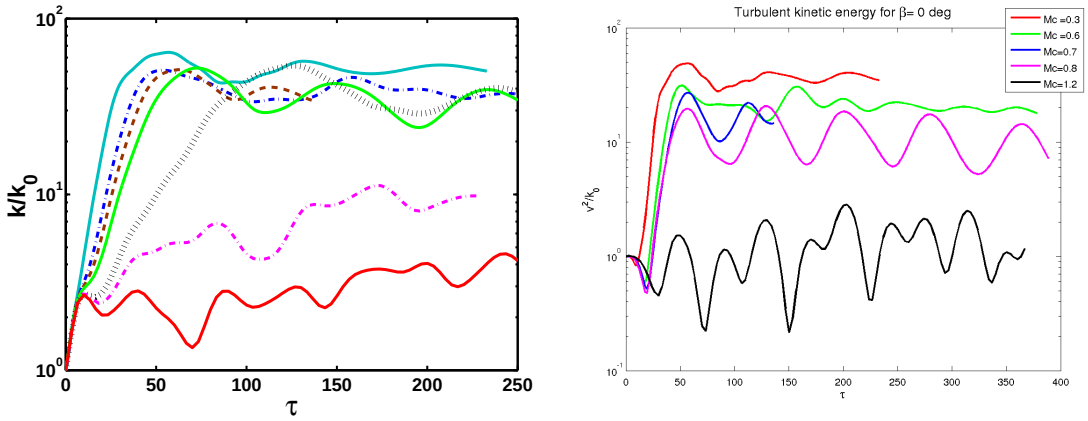

(a) (b)

Figure V.3. Temporal evolution of the normalized turbulent kinetic energy and the normal component of the turbulent kinetic energy at different Mach numbers when the initial obliqueness angle is zero, β=0.

mixing can be studied in the perspective of vorticity magnitude. One measure of vortex strength or the vorticity intensity is the *enstrophy*, Ω, defined by

$$\Omega = \frac{1}{2}\overline{\omega_3' \cdot \omega_3'}, \tag{5.8}$$

where ω_3' is the spanwise perturbation vorticity. The temporal evolution of enstrophy normalized by its initial value at different Mach numbers is illustrated in Figure V.4. As Mach number increases, the growth of enstrophy in the entire field is inhibited to the extent that at $M_c = 1.2$, the entrophy remain nearly constant.

3. Circulation. Another measure of the magnitude of the vortex strength is circulation, Γ, defined by

$$\Gamma \equiv \oint_C \vec{u'} \cdot \vec{I}, \tag{5.9}$$

where u' is the velocity perturbation field and I is a directed line segment at a point on the closed curve, C. Clearly, circulation is a kinematic property depending only

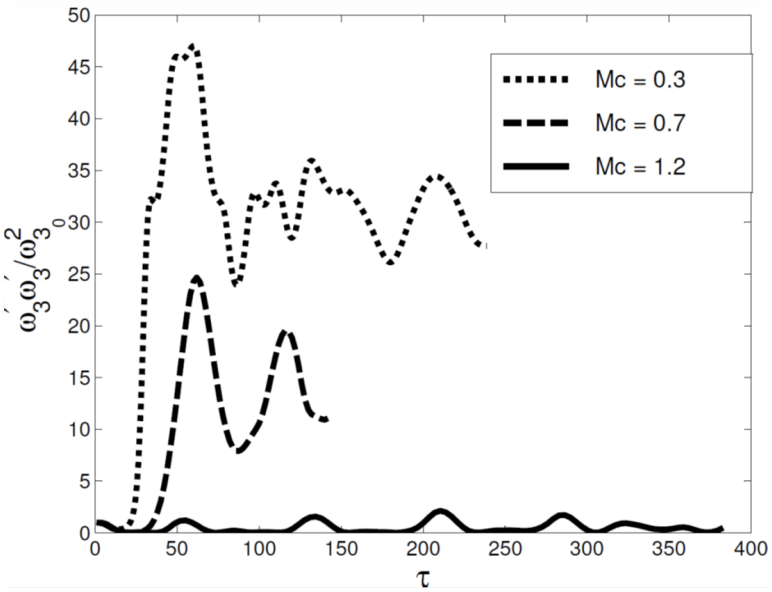

Figure V.4. Temporal evolution of the normalized enstrophy at $M_c = 0.3,\ 0.7$ and 1.2.

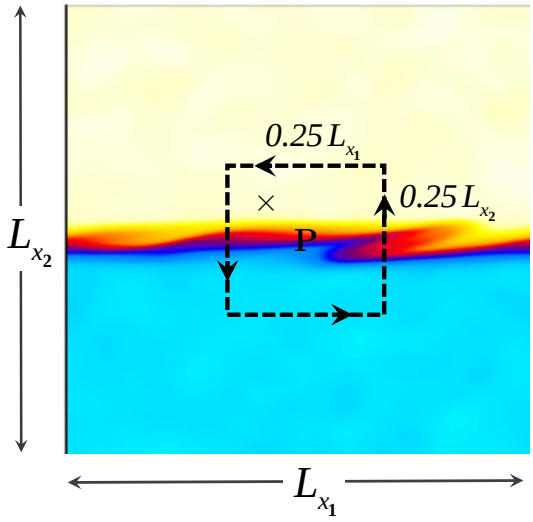

Figure V.5. Sketch of the closed curve for calculating circulation on the $x_1 - x_2$ plane.

on the velocity field and choice of closed curve. This scalar quantity is of great importance in describing vortical flow structures. Circulation exists in the flow if the line integral in (5.9) is finite. In the absence of shocks or other discontinuities, applying the Stoke's theorem to the above definition leads to

$$\Gamma = \iint_S \vec{\Omega} \cdot \vec{n} S, \tag{5.10}$$

where S is the infinitesimal area closed by the infinitesimal curve, C, and $\vec{n}$ is a normal vector to this area. Note that expressing circulation as a surface integral of the vorticity component normal to the surface enclosed by the contour is only valid for incompressible flows. For all Mach numbers, the circulation is calculated along the line integral in (5.9). A closed curve is assumed as a square with a length of $0.25L_{x_i}$ around the pivot point at the center of the mixing layer shown in Figure V.5. The temporal evolution of the normalized circulation is depicted in Figure.V.6, indicating that the circulation in the low-Mach number cases (e.g. $M_c = 0.3$) keeps increasing, as shown in Figure.V.6 (a), while it oscillates around zero for high Mach-number cases (e.g. $M_c = 1.2$) as depicted in Figure V.6 (b).

To demonstrate the change of nature of the velocity-pressure interaction, toward the dynamics of KH instability under influence of compressibility, a point close to the interface, within the vicinity of P is chosen. This point is marked by the cross sign in Figure V.5. The evolution of the velocity and pressure field at this specific location is monitored and shown in Figure V.7. At low speed flows (e.g. $M_c = 0.3$), the pressure gradient field, $\partial\hat{p}/\partial x_2$, and the source term in (5.2), $\hat{u}_2 S$, due to the nature of Poission equation, u_2' and p' remain in-phase, as shown in Figure V.7 (a). On the other hand, at high speed flows (e.g. $M_c = 1.2$), temporal of evolution of u_2'

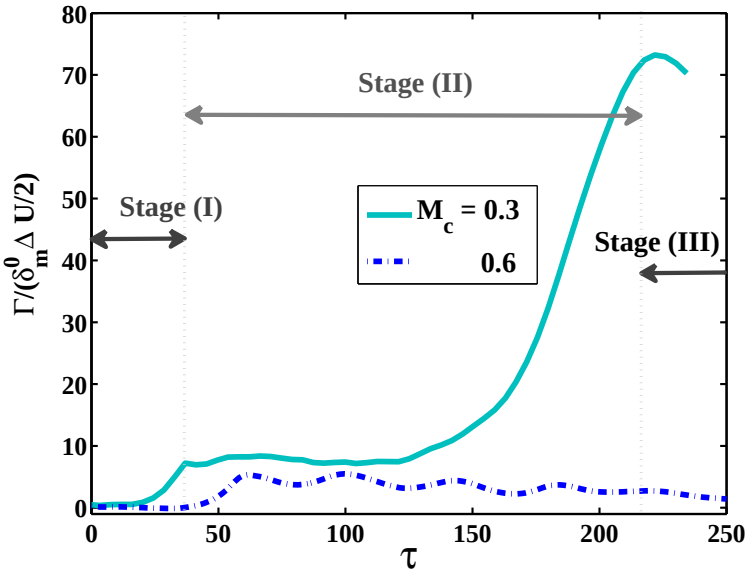

(a)

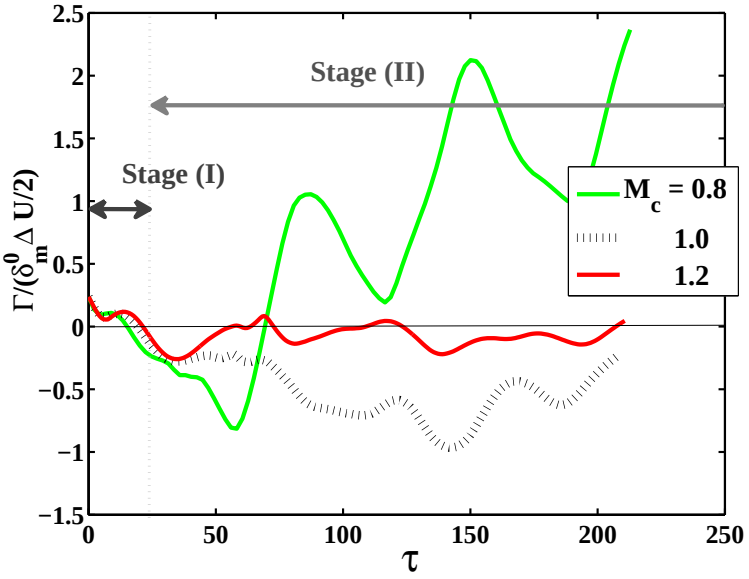

(b)

Figure V.6. Temporal evolution of the normalized circulation in (a) the incompressible mixing layers at $M_c = 0.3$ and 0.6 and (b) the compressible mixing layers at $M_c = 0.8, 1.0$ and 1.2

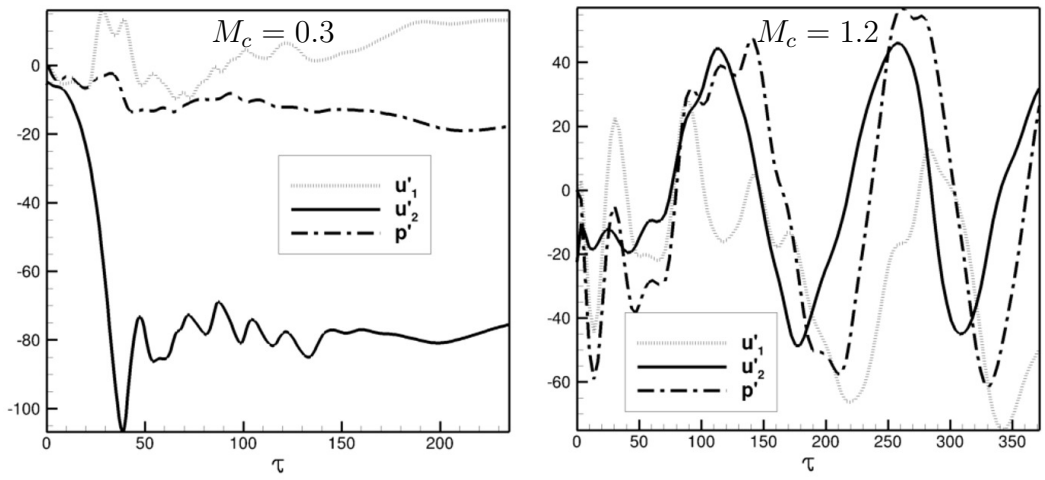

(a) (b)

Figure V.7. Temporal evolution of the perturbation field for a mixing layer with the initial velocity field of $\beta = 0$ at (a) $M_c = 0.3$ and (b) $M_c = 1.2$.

and p' at the same given point indicates that they evolve in the out-of-phase manner, seen in in Figure V.7 (b). From Figure V.7, it clear that the variation of p' in low Mach numbers is very small comparing to the counterpart in high Mach numbers, to the extent that p' keeps oscillating with the relatively high amplitude.

Consistent with findings in literature [1,2,24], all mixing characteristics diminish with Mach number indicating a strong suppression of KH instability with increasing M_c. In low speed flows, for a given initial Mach number (e.g. $M_c = 0.3$), it can be shown that p', u_1', u_2' and ω_3' fields evolve monotonically resulting in the classical KH instability behavior. Whereas, in high speed flows, the growth of most of mixing characteristics are inhibited. Now, we will examine the underlying physical mechanism which has been identified from analysis to be the p'-u_2'-ω_3' interactions. We begin with a brief description of the incompressible instability mechanism and

contrast it against the compressible-case behavior. While extending incompressible concepts to compressible flows is injudicious, it is useful for contrasting how structure evolves with the change of Mach number. Using the incompressible KH instability as the baseline behavior, we investigate how the flow changes with a gradual increase in Mach number. Starting our investigation, we begin with the incompressible KH instability.

V.C. KH Instability Mechanism at Low Mach Numbers

We now describe the three stages of KH development [70, 77] by analyzing the p' and ω_3' contours at various stages. The dynamics in the four quadrants Q_1 - Q_4 around the pivot (P) and stagnation (S_1, S_2) points, schematically shown in Fig. V.1, are central to this description. There are three distinct stages in the evolution of the KH instability at low Mach numbers [70]:

Stage 1: Initial Development Stage. The behavior in the initial development stage is dictated by the initial conditions and source terms in the pressure and vorticity equations. In this stage, velocity perturbation evolution and vorticity perturbation production are initiated by the following terms:

$$\frac{\partial u_1'}{\partial t} \sim -u_2' S, \tag{5.11}$$

$$\frac{\partial \omega_3'}{\partial t} \sim -u_2' \frac{\partial^2 U_1}{\partial x_2^2}, \tag{5.12}$$

where ω_3 is the spanwise component of vorticity perturbation. The vortex sheet, respectively is the highest concentration of vorticity, initially forms at the interface between the two streams. Low pressure region forms around pivot point P and high-pressure region about the stagnation points S_1 & S_2. In the neighborhood of P,

negative (clockwise) vortices are initiated in quadrants Q_2 & Q_4, positive (counter-clockwise) vortices in Q_1 and Q_3. Around the stagnation points S_1 & S_2, clockwise vortices are generated in Q_1 & Q_3 and the counter-clockwise vortices in Q_2 & Q_4. These features are captured in Figure. V.8 (a) and (b).

Stage 2: Pairing, merger and roll-up stage . The incompressible steadily-evolving velocity field has the following effects at the pivot point P: (i) clockwise vortices are strengthened; (ii) counter-clockwise vortices are weakened; and, (iii) pressure is further reduced. As a result, the two negative vortices grow, merge in the vicinity of P and begin to roll around P to the pivoting action of the source term in equation (5.4). As the cores of the original spanwise rollers merge and form an almost circular core, the spiral arms of weaker spanwise rollers are ejected away, seen in Figure. V.8 (d). It is well known that vorticity and negative pressure have a positive feedback interaction. Consequently, at P, both p' and clockwise vorticity mutually intensify each other. The merged clockwise vortex begins to roll-up rapidly and constitutes the central mechanism of KH instability. Therefore, this period of evolution is called *merger and roll-up stage*. The rolling vortex begins to entrain fluid from both the free-streams as can be seen from Figure. V.8 (c) and (d). At S_1 & S_2, the incompressible velocity field engenders: (i) suppression of clockwise vortex; (ii) enhancement of the counter-clockwise vortex; and (iii) rise in pressure. However, the counter-clockwise vortex and high pressure fields do not mutually intensify one another. Thus, the pressure and vorticity fields grow slowly at these stagnation points. Early in this stage, there is a sustained growth of the instability. Vorticity continues growing until the first pairing occurs, about $\tau = 30$, which is consistent

with the first peak of the circulation plot for $M_c = 0.3$ as shown in Figure. V.6 (a).

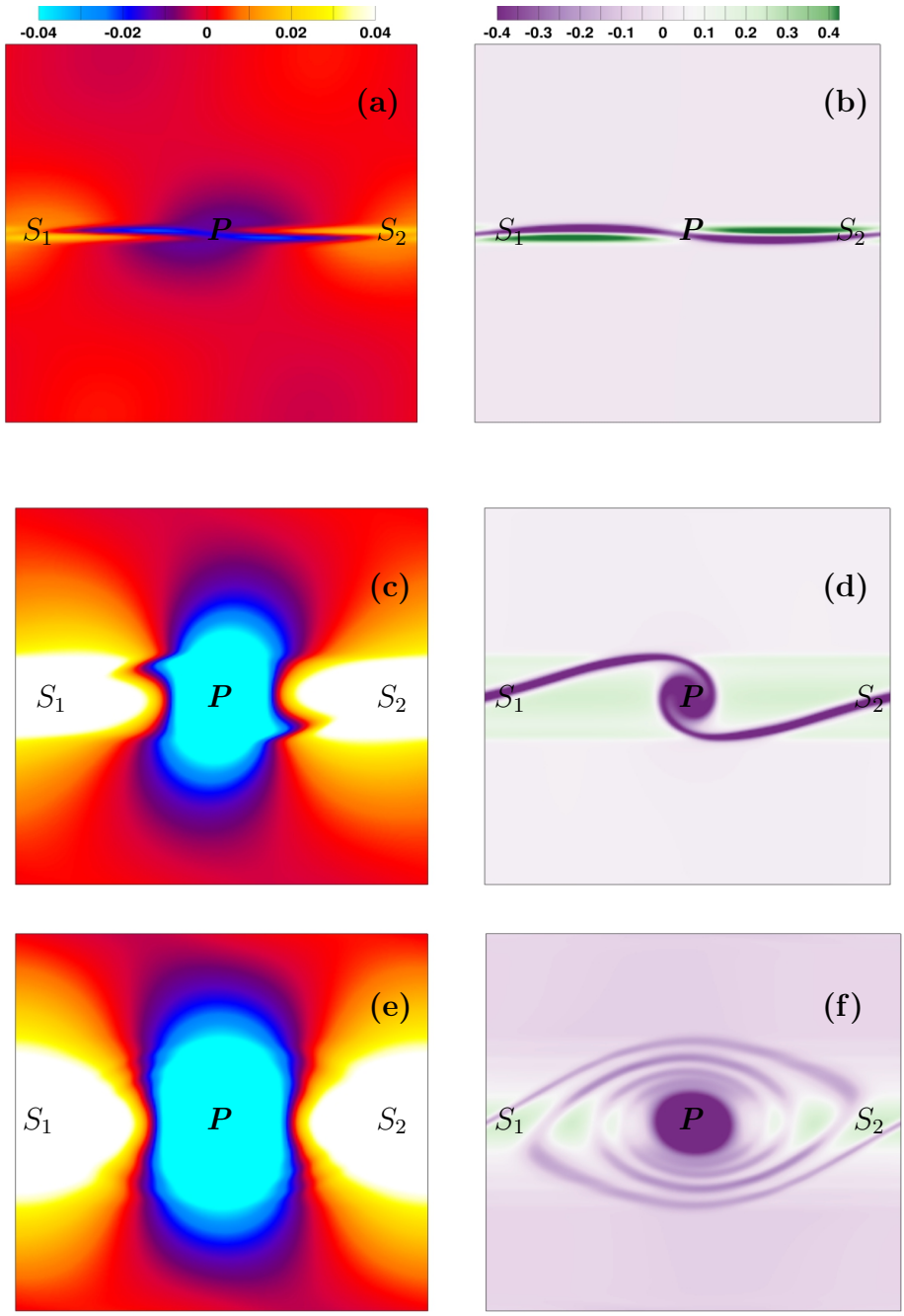

Figure V.8. $x_1 - x_2$**- plane contours of pressure perturbation contours (on the left) and spanwise vorticity perturbation (on the right) of a mixing layer at** $M_c = 0.3$**, illustrating *Stage 1* in (a-b), *Stage 2* in (c-d) and *Stage 3* in (e-f) of the KH instability development in the incompressible flows.**

Stage 3: Asymptotic KH instability stage. The final stage is marked by consolidation and rapid inward spiral rotation of the low-pressure vortex about the pivot point. Entrainment intensifies leading to the onset of instability as can be seen from Fig. V.8 (e) and (f). At this stage, subharmonics are dissipated. This leads to a nearly solid body vortex rotation in the low pressure region around P, when disturbances reach their final amplitude. The shape of the strongest roller core eventually becomes elliptical in form and vertically aligned, as does the pressure perturbation field. Following the velocity streamtrace reveals that the centers of all three spanwise cores finally get aligned on the $x_2 = 0$ plane. Eventually, the strong spanwise rollers are advected into the braid region by viscous dissipation. Ultimately, this location develops into an asymmetric structure of the so-called *cat's eye* vortex structure, shown in Fig. V.8 (f).

V.D. KH Instability Dynamics at High Mach Numbers

Unlike the well-established incompressible KH instability, the compressible counterpart has not been studied in detail. The evolution of the pressure perturbation is now governed by the hyperbolic equation (5.2). Due to the presence of a large initial shear, the effect of the source term in the pressure perturbation equation (5.2) is significant.

V.D.1. Gradient Mach Number as a Compressibility Parameter

At low Mach numbers, M_g remains very small throughout the flow domain over the entire evolution. With increasing Mach number, the region of $M_g > 1$ gets larger.

When $M_c \geq 0.8$, the formation of a layer around the interface within which $M_g > 1$ is evident. The evolution of the local value of M_g for the compressible case of $M_c = 1.2$ is shown in Figure V.9.

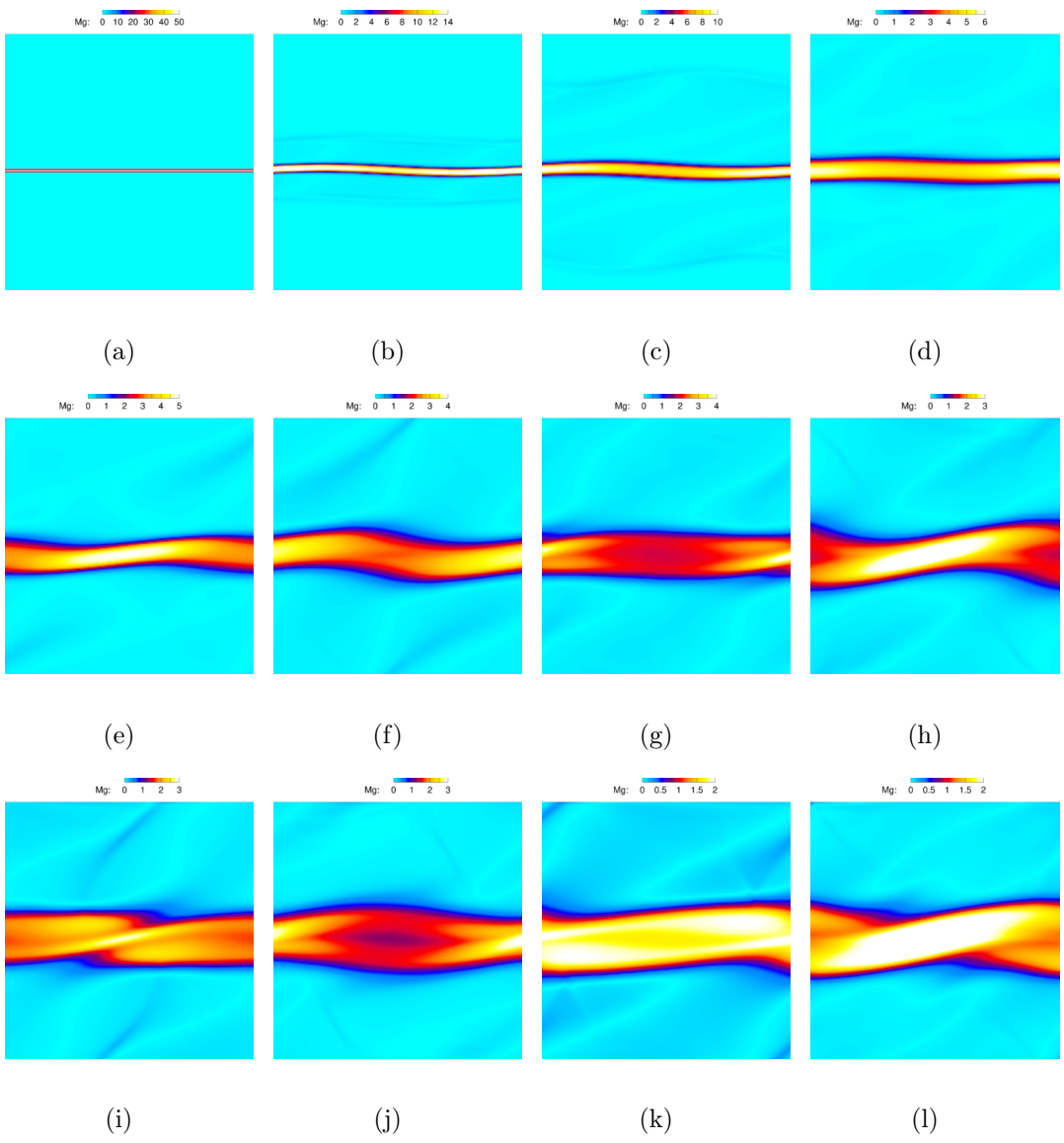

Figure V.9. Gradient Mach number contours for $M_c = 1.2$ at $\tau =$ (a) 0, (b)10, (c)24, (d)64, (e)105 , (f)172, (g)209, (h)257 ,(i)287, (j)345, (k)355 and (l) 375. Solid dark blue line indicates $M_g = 1$.

The layer around the interface wherein $M_g(x_2)$ exceeds unity is given the name *dilatational interface layer* (DIL). Based on M_g, the mixing layer can be divided into three regions: DIL and two other regions on either side comprising of the two free streams. The compressibility effects are prominent within the DIL and less so in the outer region. The three regions are presented in schematic in Fig V.10. A Mach number schematic given by Papamoschou and Roshko is shown in Figure.V.11. Contrary to the present work, Papamoschou and Roshko partition the flow field on

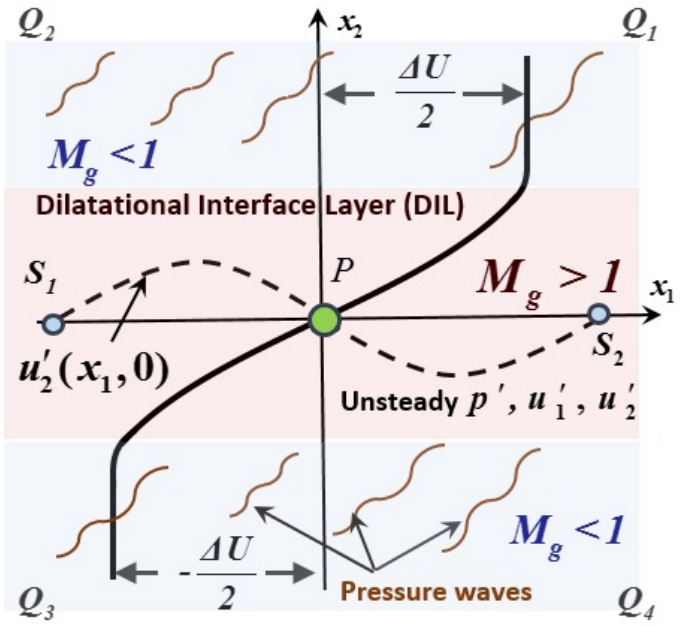

Figure V.10. A schematic of a compressible mixing layer; the dilatational interface layer where $M_g > 1$; two stagnation points (S_1 and S_2); and propagated pressure waves in the outer region (color online).

the basis of the convective Mach number. Unfortunately, such classification can be misleading as the maximum compressibility effects manifest at the interface wherein the convective Mach number can be subsonic.

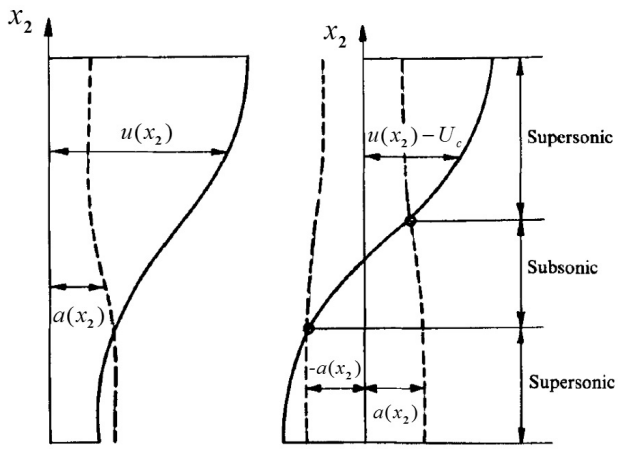

(a) (b)

Figure V.11. Profiles of the flow velocity (solid line) and speed of sound (dashed line); U_c is the convective velocity in a mixing layer given by (2.6); a is the average speed of sound which varies along the normal direction at (a) stationary (b) convective coordinates frames, taken from [1]

Within the DIL, pressure behavior is dictated by thermodynamic considerations and the perturbations evolve according to the inhomogeneous wave equation given in (5.2). Perturbation pressure waves propagate along the $x_1 - x_2$ plane with a velocity proportional to $1/M_g$. Toward the outer regions, pressure waves from the DIL propagate with the speed of $1/M_g^*$. The pressure perturbation equation in (3.31) can be rewritten in terms of the dilatation as

$$\frac{\partial p'}{\partial t} = -\gamma \bar{p} \left[\mathcal{D} - S^* \right], \tag{5.13}$$

where the velocity perturbation dilatation, $\mathcal{D}$, is defined by

$$\mathcal{D} = \frac{\partial u_i'}{\partial X_i}. \tag{5.14}$$

Since the pressure field is periodic within the DIL, the nature of the dilatation field evolution is periodic correspondingly, according to the equation (5.13). Most impor-

tantly, the flow field along the interface is unsteady under the influence of pressure wave propagation. The pressure and velocity fields develop a phase lag. Within the DIL, the value of the pressure perturbation alternates between its maxima and minima at a given point in space.

In the outer regions, $M_g(x_2) < 1$, and the source terms in the wave equations are weaker. The outer regions cannot be considered truly incompressible in character as the pressure and dilatational waves generated in the DIL propagate throughout the flow domain. A schematic of the DIL and outer layers, along with the various characteristics of the different regions are shown in Fig. V.10.

To understand the unsteady compressibility effects upon KH instability, contours of pressure and vorticity perturbations contours for $M_c = 1.2$ case are presented in Figure V.12. From Figures V.12 (c) and (e), the DIL can be identified as the narrow region in the middle wherein the pressure field shows steep variations. In the outer regions, the pressure wave merely propagates diagonally to the flow domain boundary. It is clear from the vorticity contours that high levels of vorticity are restricted to the DIL. The different stages of perturbation evolution are now described. We will first examine the behavior within DIL and then proceed to the outer regions. The different parts of the DIL will still be referred as pivot, P, and stagnation points, S_1 andS_2, depicted in Figure V.1, based upon the nomenclature introduced in the incompressible case.

Stage 1: The ***initial development stage*** of the compressible case is similar to the incompressible one as the initial conditions and source terms in the governing equations are identical. The qualitative similarities of this stage at different Mach

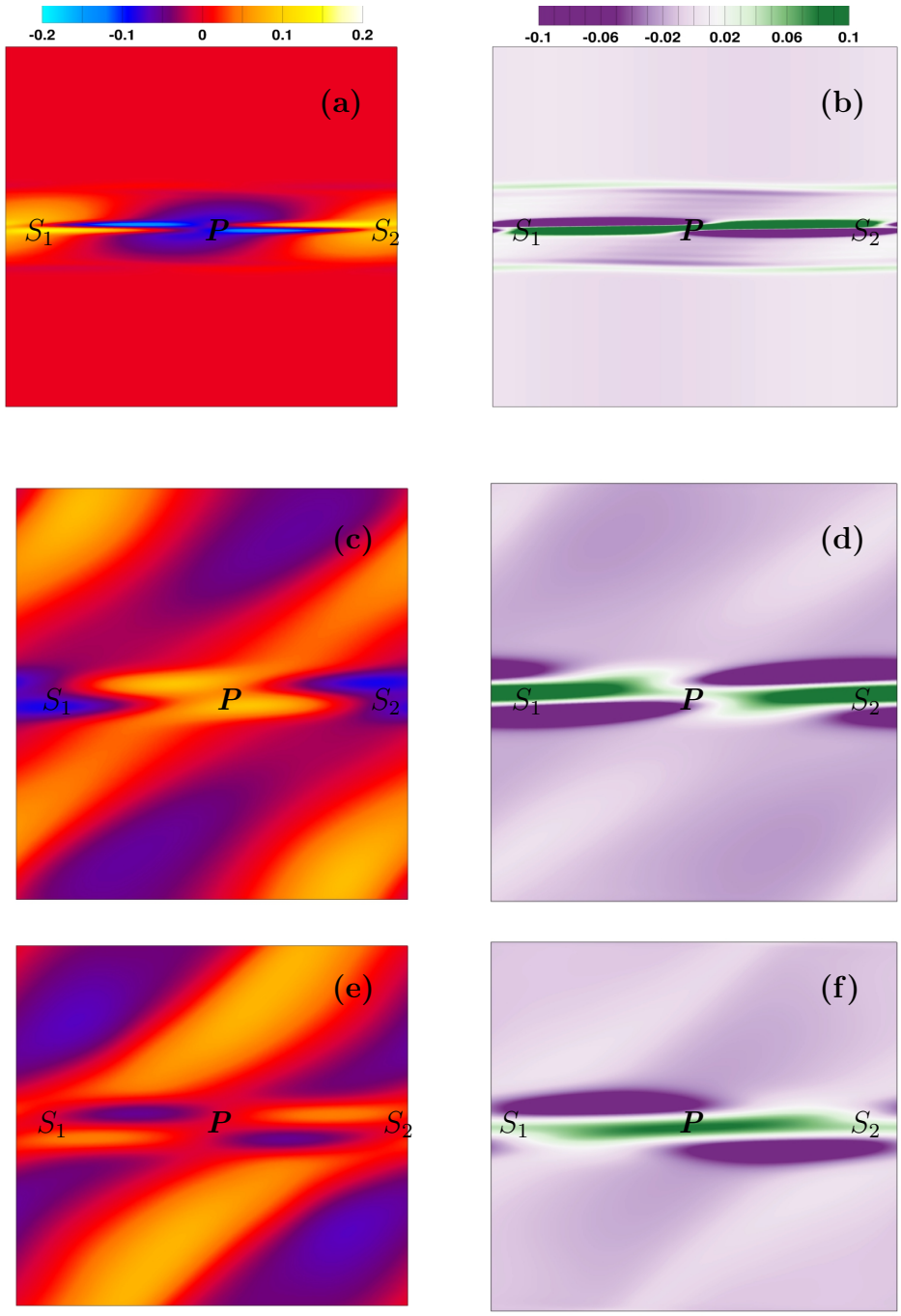

Figure V.12. Contours of pressure perturbation (on the left) and spanwise vorticity perturbation (on the right) of a mixing layer at $M_c = 1.2$, illustrating *Stage 1* in (a-b), *Stage 2* in (c-f) of the KH instability development in the compressible flows.

numbers can be seen by comparing Figure V.8 (a) and (b) with Figure V.12 (a) and (b). Once again, low and high pressure regions form around pivot point P and stagnation points $S1$ and $S2$ respectively.

Stage 2: The second stage behavior is dictated by the evolution equations of velocity and pressure fields, and therefore is markedly different in the compressible case. Now p' and u_2' evolve according to wave equations resulting in the following around P: (i) gradual u_2' magnitude reduction and sign change leading ultimately to the reversal of the vortices in Q_2 and Q_4 to counter-clockwise; (ii) similar reversal of vortices in Q_1 and Q_3 to clockwise; and (iii) gradual increase in pressure at P. Thus, vortex reversal dominates the second stage rather than merging. Indeed during the reversal process, positive pressure and counter-clockwise vortex prevail at P , shown in Figure V.12 (c) and (d). With passage of time, the pressure at P returns to negative values, clockwise vorticity returns to Q_2 and Q_4 region and counter-clockwise to Q_1 and Q_3 quadrants as seen in Figure V.12 (e) and (f). Most importantly, the reversals preclude the steady positive feedback of clockwise vortex and negative pressure field at P which is central to incompressible KH instability. A similar reversal, but in the opposite sense occurs at the stagnation points. Thus this stage is now identified as the *first vortex reversal stage* with no roll-up.

Stage 3: The final ***asymptotic stage*** is marked by periodic reversals until non-linear or viscous processes intervene. There is no steady entrainment and thus the circulation remains small.

Outer regions: Although M_g is smaller than unity in the outer regions, the behavior here is not similar to that in incompressible flow. Pressure waves generated

within the DIL propagate through these regions dominating the flow features. At any given point, the velocity is nearly periodic and this leads to very little mixing even in the low M_g regions. Although regions with large circulation are formed in these subsonic regions, vorticity reverses directions in accordance with the pressure field reversal. These large, but weak time-dependent circulation zones can not cause significant mixing.

Summary. The physical mechanism of suppression KH instability in compressible flows is explicated through the pressure-vorticity interaction dynamics. To summarize the main features of KH perturbation evolution in compressible and incompressible flows, we sketch the relevant dynamics in Figure V.13. The most crucial dynamics occur in the vicinity of the so-called pivot point P. The *first stage* of evolution in the two cases are quite similar as the behavior is dictated by the initial conditions and source terms in the evolution equations. Low pressure region forms around P and clockwise and counter clockwise vortices form in diagonally opposite quadrants as seen in Figure V.13 (a) and (b). The behavior in the *second stage* is determined by the evolution equations and is consequently markedly different in the two cases. In the incompressible case, the velocity field mediates a steady positive-feedback interaction between clockwise vortex and negative pressure field causing mutual intensification and ultimately triggering the KH instability, as illustrated in (Figure V.13 (c). The onset of compressibility engenders the formation of a layer called dilatational interface layer (DIL). Within the DIL, the compressible velocity field is inherently oscillatory as it is governed by the wave equation. This results in vorticity and pressure field reversals, precluding positive feedback growth, as shown

in Figure V.13 (d). In the *final stage*, the incompressible case features growing inward spiraling motion around the pivot point entraining increasing quantities of fluid from either side as shown in Figure V.13 (e). In stark contrast, the compressible interface features mostly oscillatory fluid motion that cannot sustain any sizable mixing between the two streams as flow field alternates between Figure V.13 (d) and Figure V.13 (f).

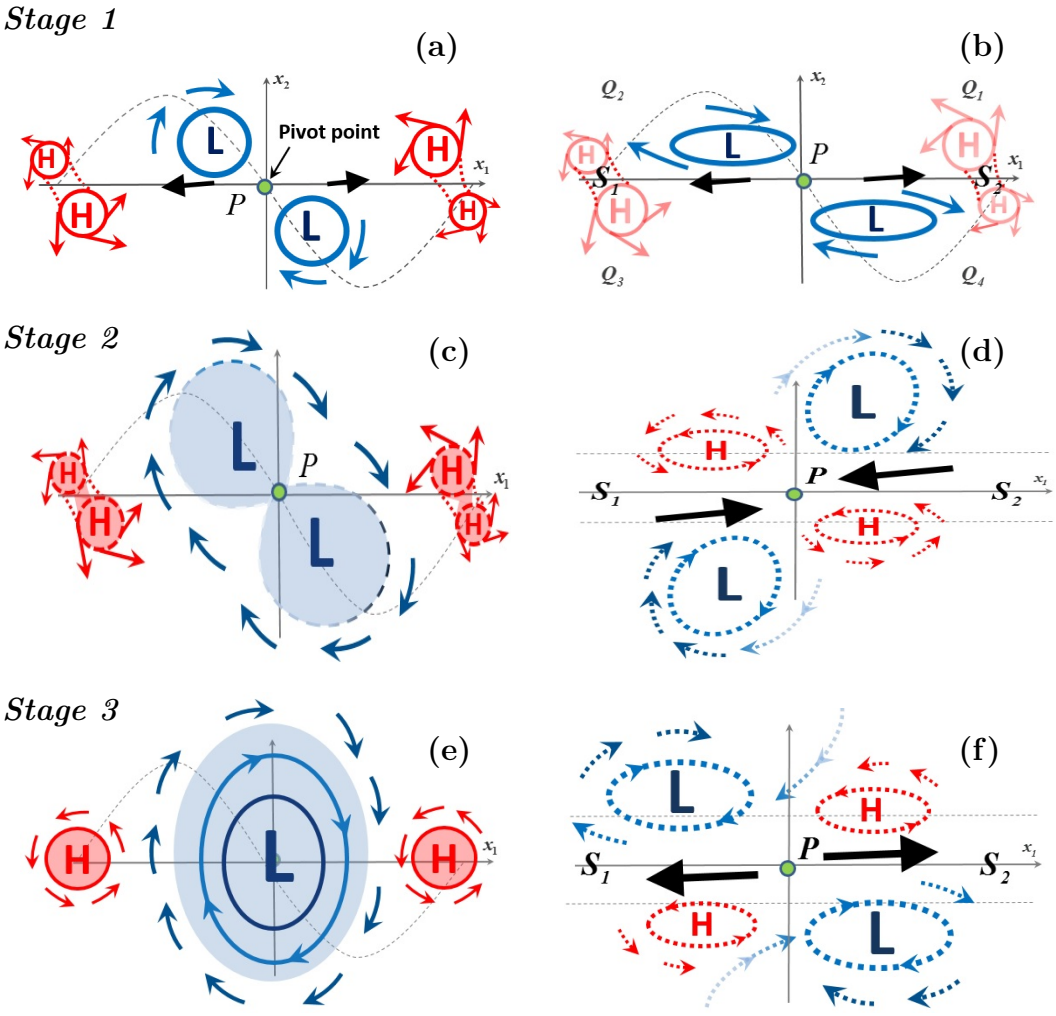

Figure V.13. Schematic representation of contrasting the stages of development of the KH instability in compressible flows (on the right) against the incompressible counterpart (on the left); and $u_2'S$ are marked by solid black arrows.

VI

EFFECT OF OBLIQUENESS AND NON-LINEAR INTERACTIONS

A comprehensive analysis of mixing layer stability entails two further investigations. Mixing layers of practical relevance are subject to perturbations that are oblique to the plane of shear. It is important to establish the stability characteristics of such oblique perturbations. It is also vital to examine the effect of non-linear interactions among oblique modes. In this chapter, we investigate obliqueness and non-linearity effects drawing from the planar KH instability analysis presented in the previous chapter. The various mixing metrics defined in the KH instability will again be employed to assess the degree of instability.

VI.A. Linear Stability of Oblique Perturbations

From the linearized perturbation equations in Chapter III, the pressure-velocity interaction of an oblique perturbation can be expressed in the form of hyperbolic wave equations:

$$\frac{\partial^2 \hat{u}_2^*}{\partial x_2^{*2}} + (\hat{u}_2^* S^* - \hat{u}_1^*) S^* + \frac{i}{\kappa} \frac{\hat{p}^*}{\gamma u^0} S \cos\beta = M_g^{*2} \frac{\partial^2 \hat{u_2}}{\partial t^{*2}}, \tag{6.1}$$

$$\frac{\partial^2 \hat{p}^*}{\partial x_2^{*2}} - \hat{p}^* + 2i \frac{u^0 \bar{\rho}}{\kappa \bar{p}} \hat{u}_2^* S \cos\beta = M_g^{*2} \frac{\partial^2 \hat{p}^*}{\partial t^{*2}}, \tag{6.2}$$

where β is the obliqueness angle of the initial perturbation mode, κ is the initial value of the wavenumber vector, S is the background shear rate and $S^* \equiv \int_0^t S(X_2) d\xi$. The normalized velocity, $\hat{u}^*$, amplitude and pressure amplitudes, $\hat{p}^*$, are obtained by $\hat{u}_i^* \equiv \hat{u}_i / u^0$ and $\hat{p}^* \equiv \hat{p}/\overline{p}$, respectively where u^0 is the r.m.s. of the initial

perturbation velocity. Recall also that the effective gradient Mach number, M_g^*, is defined by

$$M_g^* = M_g \cos\beta = \frac{S}{\bar{a}\kappa} \cos\beta. \tag{6.3}$$

Here, M_g^* is the relevant measure of compressibility experienced by an oblique perturbation mode. It is clear that M_g^* decreases with increasing the obliqueness angle. The modes with the obliqueness angle of close to $\beta = 0$ experience the highest effect of compressibility. In this work, modes with $M_g^* \geq 1$ are called *supersonic modes*. Whereas the modes aligned closer to the spanwise direction with $\beta = \pi/2$, where $M_g^* < 1$, can be classified as *subsonic modes*. It is clear that in the case of $\beta = \pi/2$, $M_g^* = 0$. Then, the pressure term is eliminated from equations (6.1)-(6.2). To analyze linear stability of oblique perturbations in mixing layers, based on the value of β, three categories of perturbation modes are considered as follows:

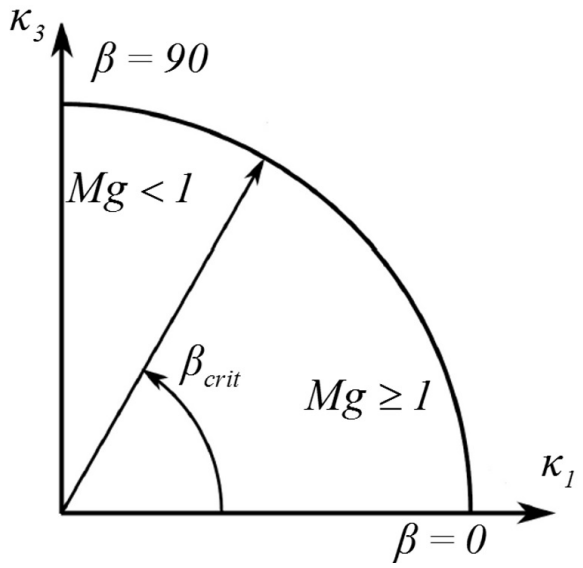

Figure VI.1. Schematic of modal stability for compressible mixing layers

1. Streamwise mode ($\beta = 0$): The baseline case of $\beta = 0$, corresponding to the initial perturbation along the streamwise direction, is extensively discussed in Chapter V. Compressibility inhibits the growth of the KH instability due to the fact that the streamwise modes are suppressed the most as Mach number increases.

2. Spanwise mode ($\beta = \pi/2$): In specific case of purely spanwise modes, the perturbations are aligned with the principal direction of the background flow, along κ_3 direction in Figure VI.1. Since $\beta = \pi/2$, $M_g^* = 0$. Therefore, the pressure perturbations evolve according to the reduced form of (6.2), which has an elliptic form as:

$$\frac{\partial^2 \hat{p}}{\partial x_2^{*2}} - \hat{p} = 0. \tag{6.4}$$

Regardless of the value of Mach number, the spanwise modes grow all the time. Since these modes are corresponding to $M_g^* = 0$, compressibility has the least effect on their growth. This is also referred to $pressure - release\ limit$ [151–154], where the spanwise wave modes can be called *pressureless* modes [155] as well. For spanwise modes, the velocity perturbations evolve according to:

$$\frac{\partial \hat{u_1}}{\partial t} = -\hat{u_2} S, \tag{6.5}$$

$$\frac{\partial \hat{u_2}}{\partial t} = -\frac{1}{\bar{\rho}} \frac{\partial \hat{p}}{\partial X_2} \sim 0, \tag{6.6}$$

$$\frac{\partial \hat{u_3}}{\partial t} = -i \frac{\kappa_3}{\bar{\rho}} \hat{p} \sim 0. \tag{6.7}$$

It is evident that the incompressible and compressible contribution of the pressure vanishes from the streamwise component of velocity amplitude, $\hat{u}_1$ in (6.5). Thus,

we can simply write $\hat{u}_1(t) = -\hat{u}_2(0)St$. If there are no initial pressure perturbation, both the incompressible and compressible of the pressure is eliminated from the $\hat{u}_2$ and $\hat{u}_3$ equations (6.6)-(6.7). Then, for spanwise modes, the turbulent kinetic energy can be written as

$$k \sim \hat{u}_1\hat{u}_1^*(t) = -u_2^2S^2t^2. \tag{6.8}$$

Hence, the evolution of velocity components are entirely unaffected by pressure regardless of the initial Mach number. The spanwise mode is unstable.

3. Oblique mode ($\beta \in (0, \pi/2)$): As this mode combines characteristics of both spanwise and streamwise modes, the full form of the non-homogeneous wave equations of (6.1)-(6.2) govern the velocity-pressure interaction. Within the range of $\beta \in (0, \pi/2)$, there exists an angle which corresponds to an *effective gradient Mach number* of unity:

$$\beta_{crit} \equiv cos^{-1}(\frac{1}{M_g}) = \frac{\kappa\bar{a}}{S}. \tag{6.9}$$

The existence of such a critical obliqueness angle verifies demarcation of the two modal classes: subsonic modes, where $\beta > \beta_{crit}$; and supersonic modes, where $\beta < \beta_{crit}$. The higher the Mach number, the larger the critical obliqueness angle. The two modal classes of supersonic and subsonic along with the critical obliqueness angle are depicted in Figure VI.1. Clearly, for the smaller β, the source terms in (6.1)-(6.2) are stronger and the perturbation growth is suppressed more by compressibility. This is in concert with the definition of the effective gradient Mach number in (6.3): when β is closer to zero, the highest compressibility effect is experienced by the oblique mode. Whereas for the oblique modes with $\beta > \beta_{crit}$, the perturbations are less

suppressed and evolve almost independent of Mach number.

In summary, spanwise modes with the initial obliqueness angle of $\beta = \pi/2$ are impervious to compressibility and perturbation grows exponentially regardless of the initial convective Mach number of a mixing layer flow. Whereas in the streamwise modes, $\beta = 0$ are affected the most by compressibility. Based on the behavior of the $\beta = 0$ and $\beta = \pi/2$ modes, it is suggested that wave modes with low obliqueness angles will experience higher compressibility effects than large obliqueness angles. To isolate the effect of the perturbation alignment, the evolution of an individual perturbation mode can be analyzed through the numerical simulations by changing the obliqueness angle $\beta : 0 \rightarrow \pi/2$ at different Mach numbers.

VI.B. Simulations of Single Oblique Modes

To focus on the linear effect, the background flow field is initially perturbed by a single wave mode of the form:

$$u_j'(\mathbf{x}, 0) = \hat{u}_j(\boldsymbol{\kappa}(0), 0) e^{i\boldsymbol{\kappa}(0)\cdot\mathbf{x}} = \hat{u}_j(\boldsymbol{\kappa}(0), 0) \sin(\boldsymbol{\kappa}(0) \cdot \mathbf{x} + \phi), \quad \phi \in [0, \pi], \qquad (6.10)$$

where $\boldsymbol{\kappa}(0)$ is the initial wavevector and $\hat{u}_j$ is the corresponding Fourier coefficient. The phase angle, ϕ, represents an arbitrary shift between the wave mode vector and the normal x_2-direction. A schematic representation of the streamwise, spanwise and oblique modes is depicted in Figure VI.2.

For all simulations, regardless of the type of initial perturbation modes, the $\hat{u}_2^0$ is set to 0.05 ΔU and $\phi = 0$. The background velocity field is again taken to be $\overline{u}_i = (\Delta U/2 \tanh(x_2/(2\delta_m^0), 0, 0)$, where δ_m^0 is the initial momentum thickness of the mixing layer. The density ratio between two streams is specified to unity. The initial

background pressure is set to a uniform value, p_0. The initial temperature for all the cases is $T_0 = 300$. The initial momentum thickness Reynolds number is fixed to $Re^0_{\delta_m} = 400$ for all cases at different initial convective Mach numbers. The Prandtl number is set to $Pr = 0.7$. In the current simulations, air is used as the working fluid, thus, the Gas constant is $R = 287\ (J/KgK)$ and the specific heat ratio is $\gamma = 1.4$. The simulation parameters are presented in Table VI.1.

Table VI.1. Simulation parameters for the study of the obliqueness angle effects

Case	M_c	β	δ^0_m	$N_{x_1} \times N_{x_2} \times N_{x_3}$
M3B0	0.3	0	0.25	$256 \times 1024 \times 128$
M3B30	0.3	30	0.25	$256 \times 512 \times 128$
M3B60	0.3	60	0.25	$256 \times 512 \times 128$
M3B90	0.3	90	0.25	$256 \times 256 \times 128$
M7B0	0.7	0	0.25	$256 \times 1024 \times 128$
M7B30	0.7	30	0.25	$256 \times 512 \times 128$
M7B60	0.7	60	0.25	$256 \times 512 \times 128$
M07B90	0.7	90	0.25	$256 \times 256 \times 128$
M12B0	1.2	0	0.25	$256 \times 1024 \times 128$
M12B30	1.2	30	0.25	$256 \times 512 \times 128$
M12B60	1.2	60	0.25	$256 \times 512 \times 128$
M12B90	1.2	90	0.25	$256 \times 256 \times 128$

Now, we present results for these three classes of modes by presenting the temporal evolution of the momentum thickness (δ_m), vorticity thickness (δ_ω), turbulent kinetic energy (k) and the average of the normal component of turbulent kinetic energy ($\overline{u_2' u_2'}$). All quantities are non-dimensionalized- in the conventional way- by their initial values. Recall that time is non-dimensionalized by the maximum initial shear rate: $\tau = (\Delta U/\delta^0_m)t$.

I. Streamwise modes ($\beta = 0$): The initial dilatational velocity perturbation

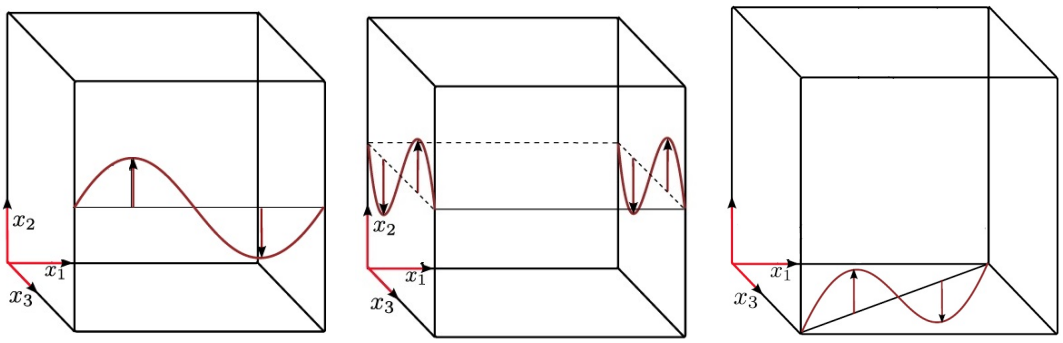

Figure VI.2. Schematic diagrams (not to scale) of the initial perturbation mode within the computational domain: (a) streamwise, (b) spanwise, and (c)oblique wave modes

is along the streamwise direction and has the form of

$$(u_1', u_2', u_3') = (0, \hat{u}_2^0 \sin(\kappa_1^0 x_1), 0) \tag{6.11}$$

Although the streamwise mode case, ($\beta = 0$) was discussed extensively in Chapter V, in order to identify the role of the obliqueness angle on the instability of a mixing layer, this case is included here as well. The evolution of the perturbation rate, shown in Figure VI.3, demonstrates that the streamwise modes experience the highest effective Mach number. The normalized momentum thickness is much smaller at $M_c = 1.2$ than one of quasi-incompressible case, i.e. with the lowest convective Mach number, e.g. $M_c = 0.3$, depicted in Figure VI.3 (a). Compressibility inhibits the growth of the vorticity thickness as well, as seen in Figure VI.3 (b).

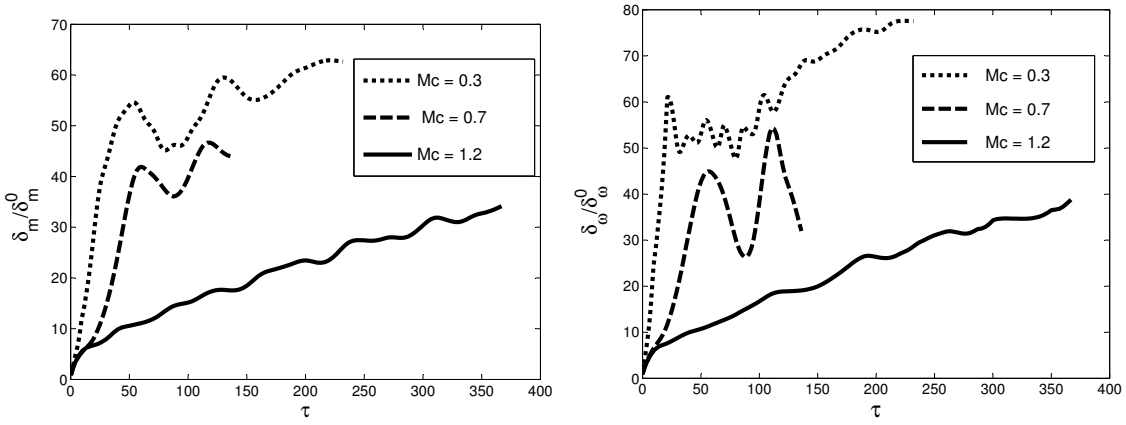

Figure VI.3. The temporal evolution of the normalized momentum thickness and the normalized vorticity thickness at different Mach numbers when the initial obliqueness angle is zero, β=0.

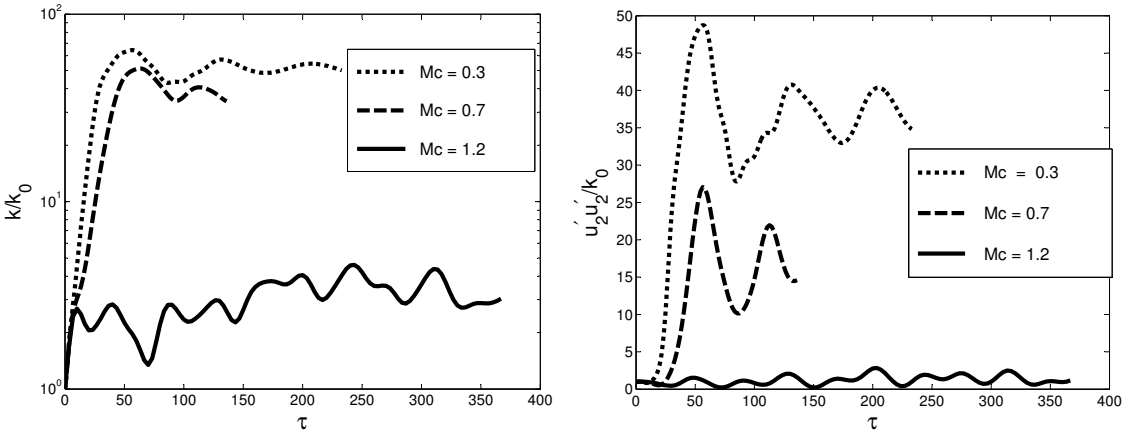

Figure VI.4. The temporal evolution of the normalized turbulent kinetic energy and the normal component of the turbulent kinetic energy at different Mach numbers when the initial obliqueness angle is zero, β=0.

II. Spanwise modes ($\beta = \pi/2$): For these wavemodes, the initial solenoidal velocity perturbation used in the DNS is given by:

$$(u_1', u_2', u_3') = (0, \hat{u}_2^0 \sin(\kappa_3^0 x_3), 0). \tag{6.12}$$

The evolution of both the momentum thickness and the vorticity thickness for the spanwise modes ($\beta = \pi/2$) is demonstrated in Figure VI.5. There is rapid growth for both thicknesses regardless of the initial convective Mach number. The same trend can be observed in the evolution of the normalized kinetic energy, as shown in Figure VI.6 (a), while the evolution of the most contributive component of turbulent kinetic energy in the case of $\beta = \pi/2$, $\overline{u_2' u_2'}$, is shown in VI.6 (b). Note that the change of $\overline{u_2' u_2'}$ is fairly small as the Mach number increases, as shown in Figure VI.6 (b). Clearly, the growth of the spanwise wavemode perturbations is impervious to compressibility. The evolution of both the momentum thickness and the turbulent kinetic energy indicates the monotonic growth of the mixing layer, thus, leading to the unstable state.

In this case, the linear analysis shows that the velocity field experiences the least compressibility effect. This implies that irrespective of the initial convective Mach number, the streamwise velocity perturbations will experience a monotonic growth as indicated in (6.5) and illustrated in Figure VI.6 (b), referring to the pressure-release limit in literature. Consequently, the turbulent kinetic energy evolution also follows as the pressure-release limit undergoes the monotonic growth as shown in Figure VI.6 (a). The variation of u_2' remains small, as shown in Figure VI.6 (b). This is perfectly in agreement with the results of the linear analysis expressed in equation (6.6).

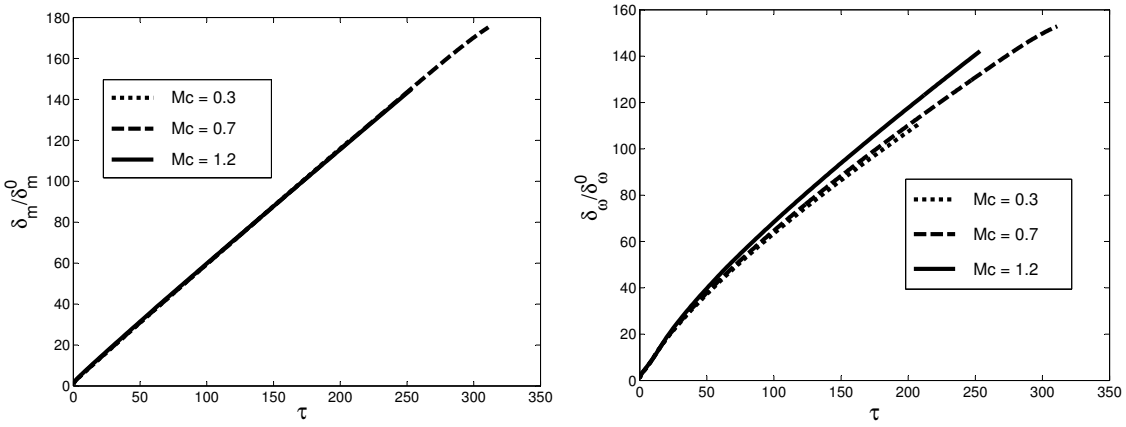

Figure VI.5. The temporal evolution of the normalized momentum thickness and the normalized vorticity thickness at different Mach numbers when the initial obliqueness angle $\beta = \pi/2$.

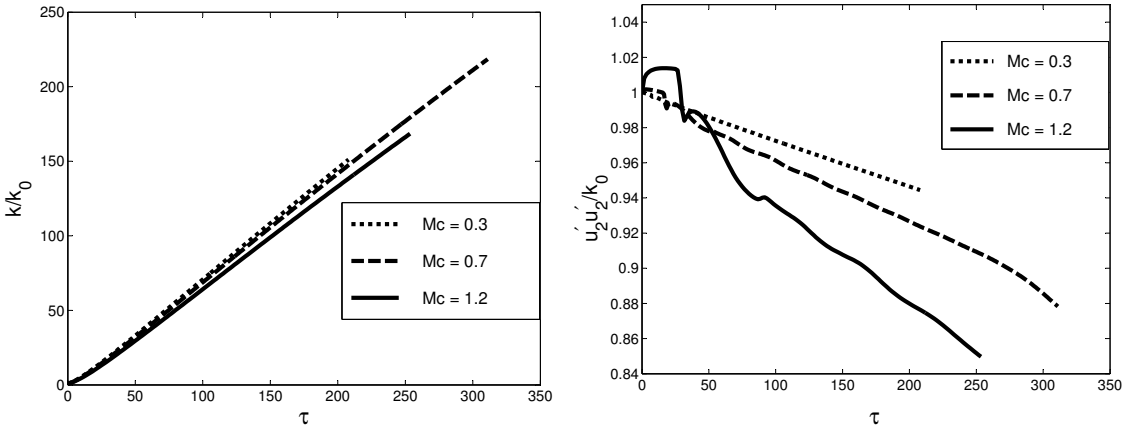

Figure VI.6. The temporal evolution of the normalized turbulent kinetic energy and the normal component of the turbulent kinetic energy at different Mach numbers when the initial obliqueness angle is $\pi/2$, $\beta = 90$.

III. Oblique modes, $\beta \in (0, \pi/2)$: Oblique modes combine characteristics of both streamwise and spanwise wave modes. The initial oblique modes perturbation have the form of

$$\vec{u'} = (u'_1, u'_2, u'_3) = (0, \hat{u}_2^0 \sin(\kappa_1^0 x_1 + \kappa_3^0 x_3), 0), \tag{6.13}$$

where both the streamwise and spanwise wavevector components are initially non-zero, $\kappa_1^0 \neq \kappa_3^0$. The evolution of a single wave mode for various obliqueness angles has been studied, but for the sake of brevity, only the results of the obliqueness angles $\beta = \pi/6$ and $\pi/3$ are presented. The evolution of the momentum thickness and the vorticity thickness for the single mode perturbation with obliqueness angle of $\beta = \pi/6$ is shown in Figure VI.7 and those of $\beta = \pi/3$ is shown in Figure VI.9.

It is evident that as obliqueness angle increases, the effect of compressibility diminishes. For instance, the evolution of the turbulent kinetic energy for $\beta = \pi/6$, shown in Figure VI.8 (a), indicates that the initial development stage persists similarly to the streamwise wave mode shown in Figure VI.4, where there is an initial saturation point. For for the case of $\beta = \pi/3$, there is a weaker dependence on M_c in the evolution of perturbation, similar to the spanwise case. Note the evolution of momentum thickness and turbulent kinetic energy for $\beta = \pi/3$ mode in Figure VI.9 (a) and Figure VI.10 (b), respectively. Nonetheless, compressibility still suppresses the perturbation growth as it shown through the evolution of all mixing indicators in Figures VI.10 & VI.9.

Comparing the evolution of either of these mixing indicators, for different obliqueness angles at a given Mach number reveals that modes closer to the streamwise direction become more stable. Conversely, the more closely the initial perturbations

are aligned with the spanwise direction, the more unstable they become. In other words, in high speed flows, oblique modes with larger solenoidal components or larger β, e.g. $\beta = \pi/3$, (Figure VI.10) have higher kinetic energy content than do oblique modes of smaller β, e.g. $\beta = \pi/6$ (Figure VI.8).

For high speed flows, the nature of velocity field evolution can be analyzed through the turbulent kinetic energy, k, or its normal component, $\overline{u_2' u_2'}$. At a given Mach number (e.g. $M_c = 1.2$), comparing the temporal evolution of k and $\overline{u_2' u_2'}$ for the $\beta = \pi/6$ oblique mode (Figure VI.10) with that of the streamwise mode (Figure VI.4) and spanwise mode (Figure VI.6) shows that the wave-like behaviour of velocity fluid is less observed as β increases. This essentially stems from the change in the nature of the pressure expressed by the hyperbolic (wave) equation of (6.2) when $\beta = 0$, to the purely elliptic equation of (6.4) when $\beta = \pi/2$. This is evident since the oscillation impact decreases as $\beta : 0 \rightarrow \pi/2$.

Linear analysis in Chapter III demonstrates that the velocity component u_2' plays an important role in the evolution of perturbation kinetic energy and spanwise vorticity. Comparing the temporal evolution of $\overline{u_2' u_2'}$ for different oblique angles at a given Mach number, shown in Figures VI.4-VI.6 (b), indicates that in low-speed flows (e.g. $M_c = 0.3$), the growth rate of $\overline{u_2' u_2'}$ decreases as β increases. However, in high-speed flows (e.g. $M_c = 1.2$), the $\overline{u_2' u_2'}$ growth of the streamwise modes ($\beta = 0$) is substantially more suppressed compared to the one of other oblique modes (e.g $\beta = \pi/6$ or $\pi/3$). It is important to point out that in spanwise modes ($\beta = \pi/2$), $\overline{u_2' u_2'}$ remains almost the same regardless of the initial Mach number as shown in Figure VI.6 (b), while there is still a trend of slight suppression of growth with the

increase of Mach number.

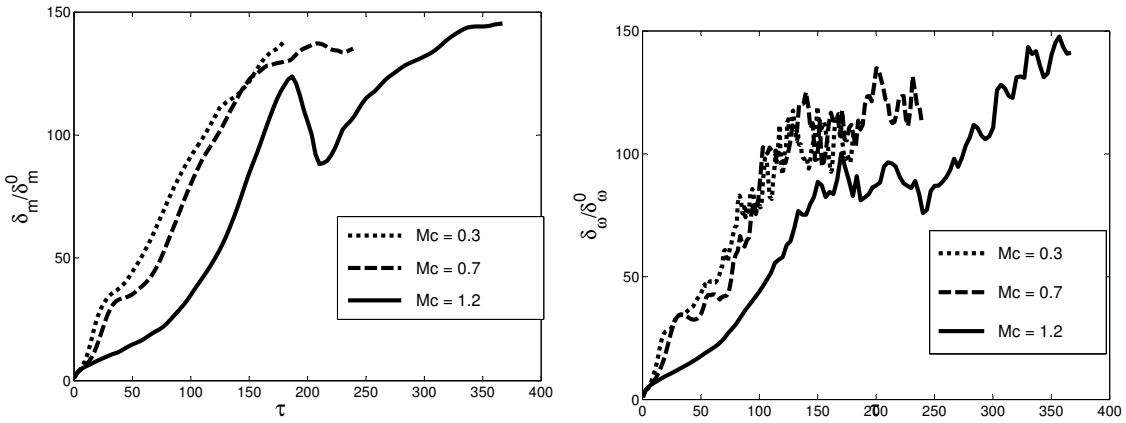

Figure VI.7. The temporal evolution of the normalized momentum thickness and the normalized vorticity thickness at different Mach numbers when the initial obliqueness angle is $\beta = \pi/6$.

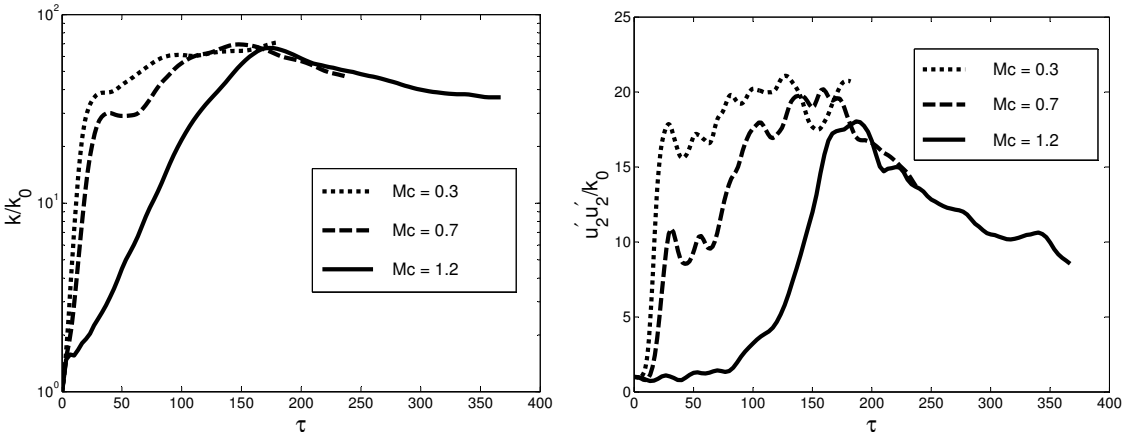

Figure VI.8. The temporal evolution of the normalized turbulent kinetic energy and the normal component of the turbulent kinetic energy at different Mach numbers when the initial obliqueness angle is $\beta = \pi/6$.

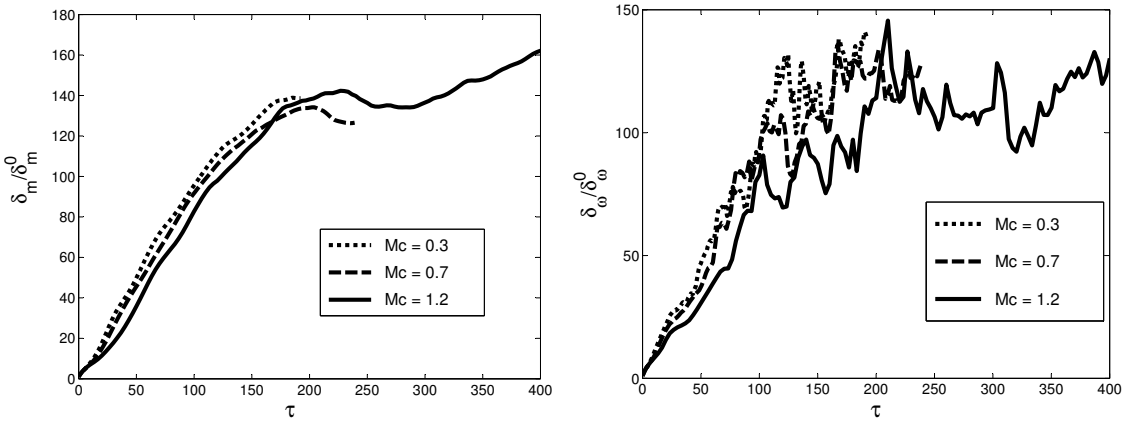

Figure VI.9. The temporal evolution of the normalized momentum thickness and the normalized vorticity thickness at different Mach numbers when the initial obliqueness angle is $\beta = \pi/3$.

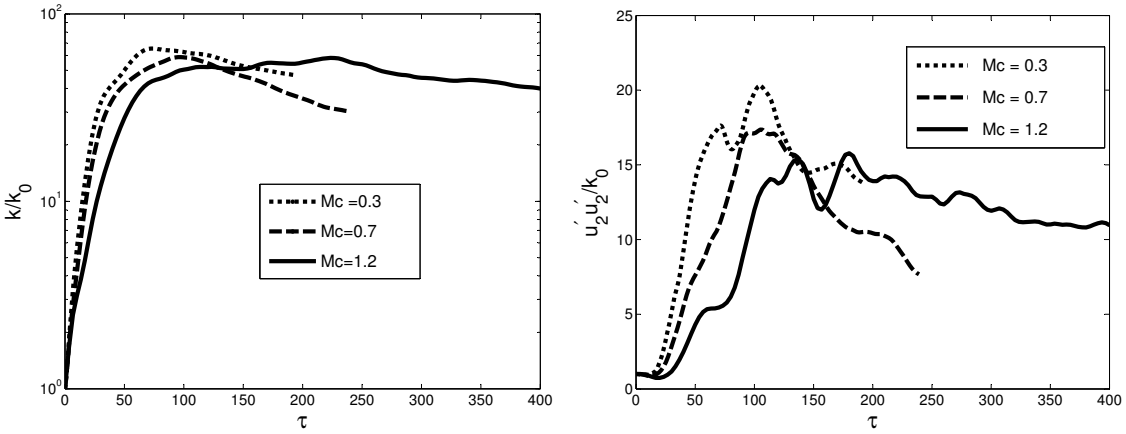

Figure VI.10. The temporal evolution of the normalized turbulent kinetic energy and the normal component of the turbulent kinetic energy at different Mach numbers when the initial obliqueness angle is $\beta = \pi/3$.

The evolution of the normalized turbulent kinetic energy, Figure VI.4 (a) illustrates that after the first peak of the initial amplification, at any given Mach number, perturbations will eventually reach an asymptotic stability. It may be use-

ful to highlight the saturation level of the normal-component of energy, $\left(\overline{u_2' u_2'}\right)_{max}$, where the first maximum of energy occurs. The corresponding time can be denoted by τ_{max} as well. Figure VI.4 (a) shows that saturation level decreases drastically as Mach number increases. Compressibility inhibits the growth of the streamwise perturbations in high-speed flows (e.g. for $M_c = 1.2$). Therefore, the suppression of the growth of $\overline{u_2' u_2'}$ is more enhanced in high-Mach number mixing layer, shown in Figure VI.4. It is important to note that all Mach-number mixing layers share the similar initial growth stage. As it is shown in VI.4 (b), the normal perturbations peak for the first time at the relatively similar τ_{max} values regardless of their initial convective Mach numbers. Notably, spanwise perturbations are impervious to Mach number effects. Within $0 < \beta < \pi/2$, the wave modes behave within the range of the stable streamwise modes, contributing to the KH instability and the unstable spanwise modes, contributing the exponential growth of perturbation. If the wave mode is aligned closer with the shear direction, it behaves similar to the unstable subsonic modes. Whereas for modes aligned closer with streamwise direction, the growth is more suppressed by compressibility. This is evidence of how the overall flow evolution is highly dependent on the precise form of the initial perturbations.

The effect of obliqueness on the growth of perturbation stability is summarized in the schematic diagram in Figure VI.11. For a given M_c, perturbation suppression intensifies with decrease of β. For a given β, perturbation suppression intensifies with increase of M_c.

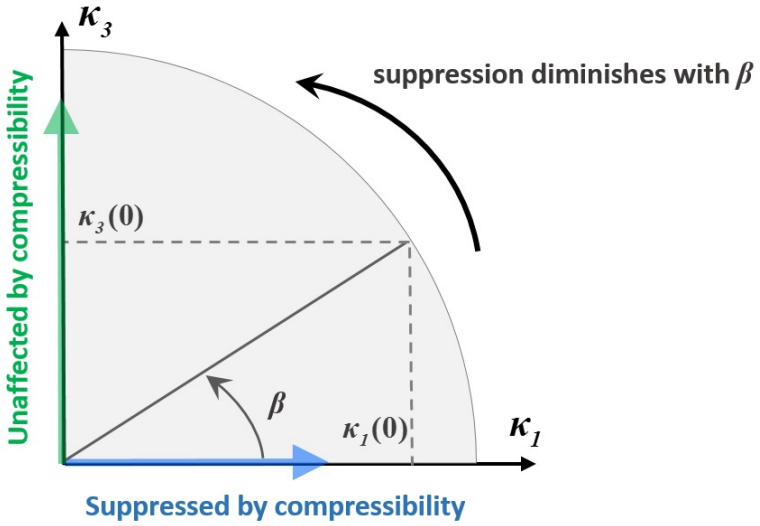

Figure VI.11. Stability map of the compressible mixing layer

VI.C. Effect of the non-linear interactions

To investigate the effect of compressibility manifesting via non-linear interactions, we consider two classes of initial conditions at different initial Mach numbers: (i) single mode and (ii) coupled mode. Investigation of non-linear interactions is complex due to the emergence of wave-vectors not present in the initial conditions. However, the most elementary way to understand the non-linear interaction is through a triadic-interaction map. The term *triad* refers to the interaction between two perturbation wavevectors ($\kappa^{\mathbf{a}}$ and κ^b) leading to the generation of a third wave-vector (κ^c) such that:

$$\kappa^c = \kappa^a \pm \kappa^b, \tag{6.14}$$

In spectral space, energy transfer can be explained by triadic interaction among wave modes. The non-linear triadic interaction does not create or destroy energy.

It merely redistributes energy among the constituents of the interaction. Energy transfers predominantly from lower to higher wavenumber or from the more energetic perturbations to the less energetic ones.

I. Single initial mode: If the initial perturbation field consists a single mode, then the first stage of non-linear interaction will involve *only* self-interaction. Then, according to the triadic interaction rules, the new generated mode will be collinear with the original one. In other words, as single mode of arbitrary obliqueness β will generate higher harmonics whose obliqueness will continue to be β. In the second stage, the following infarctions are possible: (i) original-original, (ii) original-first harmonic and (iii) first-harmonic-first harmonic. In subsequent stages, higher and higher harmonics will be generated until viscous effects terminate higher wavenumber modes. All the generated modes will be of the same obliqueness β of the original mode. In the incompressible flows, the non-linear effect do no qualitatively affect the inviscid stability characteristics since all of the harmonics share the same β. To a large extent, the stability character of the newly generated modes will be similar to that of the original mode. Nonetheless, based on the definition of M_g^* in (6.3), the higher harmonics may experience lower M_g^* as the wavenumber vector magnitude $|\kappa|$ attains higher value. In summary, non-linearity does not affect the stability of single initial modes.

II. Coupled initial mode: to emphasize the importance of the non-linear interactions, we now initialize the perturbations field with two wavevectors of oblique-

ness $\pm\beta$. A schematic of the first stage of non-linear interactions is shown in Figure VI.12. The first stage results in the emergence of two new obliqueness angles: streamwise ($\beta = 0$) and spanwise ($\beta = \pm\pi/2$). In subsequent non-linear interaction stages, more and more modes will be generated due to the following interactions: (i) original-original, (ii) original-generated, and (iii) generated-generated modes. These interactions will lead to more and more modes of different wavenumber magnitude and obliqueness angles. In the incompressible case, all the modes grow, while for the compressible case, the modes oriented closer to the streamwise direction get more suppressed compared to others as schematically shown in Figure VI.11 earlier. The stability characteristics will depend upon both parameters: $|\kappa|$ and β. The compressibility effect on each generated mode will depend on, M_g^*, the effective Mach number:

$$M_g^* = M_g \cos\beta = \frac{S}{\bar{a}\kappa} \cos\beta. \tag{6.15}$$

Clearly, small β or $|\kappa|$ values will experience higher Mach numbers and greater degree of suppression. Viscous effects are proportional to $\nu\kappa^2$. Thus, in simulations starting with paired $\pm\beta$ modes, we can expect highest level of energy content in modes close to $\beta = \pm\pi/2$. The energetic modes are anticipated to be of small wavenumber magnitude, $|\kappa|$.

A schematic of triadic interactions between two wavevectors of obliqueness angles β and $-\beta$ is shown in Figure VI.12. Each interaction results in emergence of streamwise ($\beta = 0$) and spanwise ($\beta = \pm\pi/2$) modes. These interactions are then repeated iteratively leading to a rapid proliferation of modes. Any generated streamwise modes will be suppressed and spanwise modes will be unstable. Therefore, even

if the initial modes are stable, non-linear interactions can lead to unstable modes. We now perform DNS of paired modes to verify the foregoing analysis and establish the effects of non-linearity.

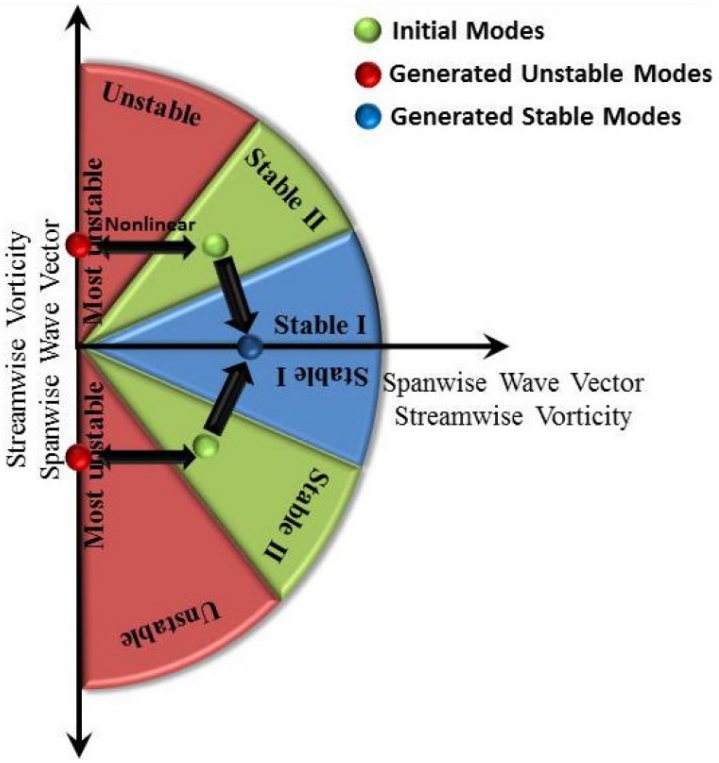

Figure VI.12. Sketches of the three types of triad interactions among wavemodes

VI.C.1. Simulations of Coupled Oblique Modes

To isolate the non-linearity effects, the temporal evolution of single wave modes is contrasted with that of coupled pair wave modes. The velocity perturbation initial condition for a single wave mode and coupled pair mode under consideration are given

respectively by:

$$\vec{u'} \equiv (u'_1, u'_2, u'_3) = (0, \hat{u}_2^0 \sin(\kappa_1^0 x_1 + \kappa_3^0 x_3), 0), \tag{6.16}$$

$$\vec{u'} = (u'_1, u'_2, u'_3) = (0, \hat{u}_2^0 \sin(\kappa_1^0 x_1 + \kappa_3^0 x_3) + \hat{u}_2^0 \sin(\kappa_1^0 x_1 - \kappa_3^0 x_3), 0). \tag{6.17}$$

For both single wavemodes and pair wavemodes, the streamwise wavenumber is initially taken as equal to the spanwise wavenumber, $\kappa_1^0 = \kappa_3^0$. Therefore, a single mode with obliqueness angle of $\beta = \pi/4$ and a coupled mode with the obliqueness angle of $\beta = \ pm\pi/4$ are considered. The schematic of these two classes of wave modes are presented in VI.13. The simulation parameters are shown in Table VI.2.

Table VI.2. Simulation parameters for non-linear effects study

Case	M_c	β	δ_m^0	$N_{x_1} \times N_{x_2} \times N_{x_3}$
N1	0.3	$\pi/4$	0.25	$256 \times 512 \times 128$
N2	0.3	$(\pi/4, -\pi/4)$	0.25	$256 \times 512 \times 256$
N3	1.2	$\pi/4$	0.25	$256 \times 512 \times 128$
N4	1.2	$(\pi/4, -\pi/4)$	0.25	$256 \times 512 \times 256$

Turbulent kinetic energy: The evolution of the energy spectrum on the plane normal to the shear, the $\kappa_1 - \kappa_3$-plane, is defined by

$$E(\kappa_1, \kappa_3) = \int_{-L_{x_2}/2}^{L_{x_2}/2} \hat{u}_i(\boldsymbol{\kappa})\, \hat{u}_i{}^c(\boldsymbol{\kappa}) \mathrm{d}x_2, \tag{6.18}$$

where $(.)^c$ indicates a complex conjugate, and κ_1 and κ_3 are taken as integer wavenumbers contained in the computational domain. To analyze the non-linearity effects, the energy content, $E(\kappa_1, \kappa_3)$, calculated by (6.18), for the single mode and coupled

mode are compared in Figure. To establish how such non-linearity effects correspond to compressibility, this comparison is carried out at low and high Mach numbers. The temporal growth of the turbulent kinetic energy, k/k_0, for both single and coupled modes are shown in Figure VI.14. For each initial mode, turbulent kinetic energy is non-dimensionalized in the conventional way by its initial value, k_0. Clearly, at high Mach number the coupled mode has much higher growth than a single wave mode. Focusing on the difference between the magnitude of k/k_0 for the single and pair modes as time advances, in the case of incompressible (Figure VI.14 (a)) and the

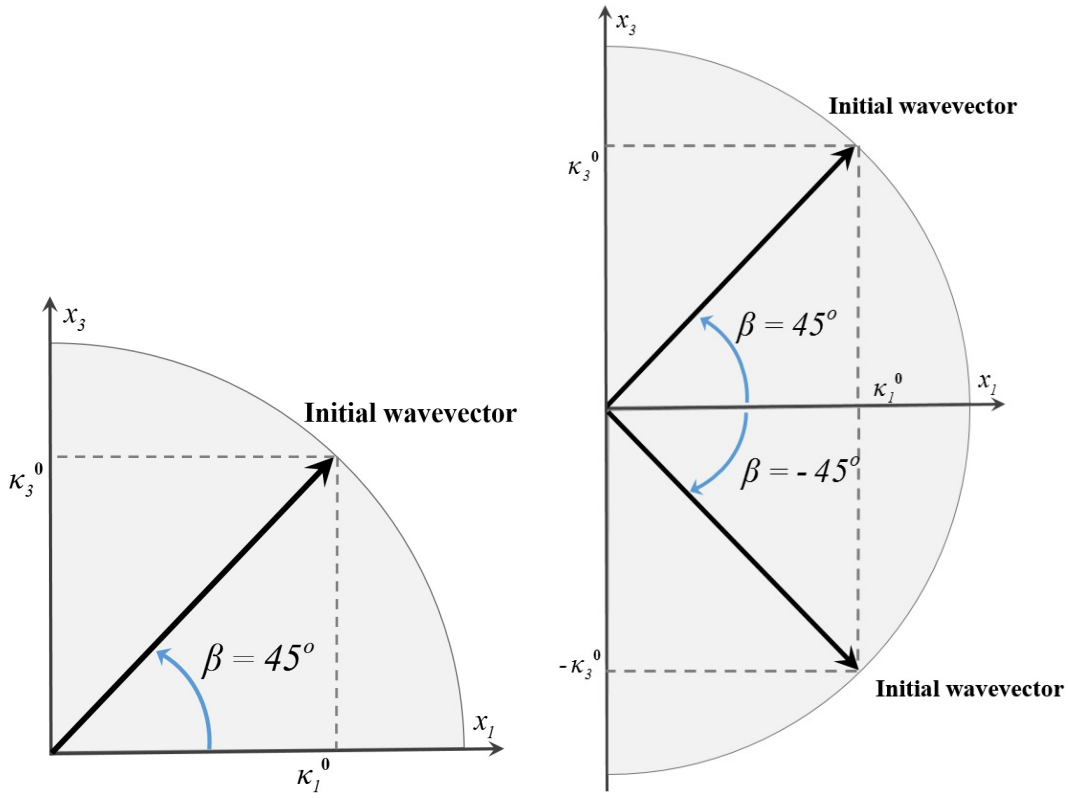

Figure VI.13. Schematic representation of the initial wavemode in the κ_1–κ_3 plane for (a) a singleton with the obliqueness angle of $\beta = \pi/4$ and (b) a pair wavemode with the obliqueness angle of $\beta = (\pi/4, -\pi/4)$.

compressible case (Figure VI.14 (b)), demonstrates non-linear effects are enhanced in high speed flows. This is due to the fact that single modes in high-Mach number flows are more affected and suppressed by compressibility than the coupled modes. Note that all discussion is restricted to the early stages of development or before the breakdown to turbulence.

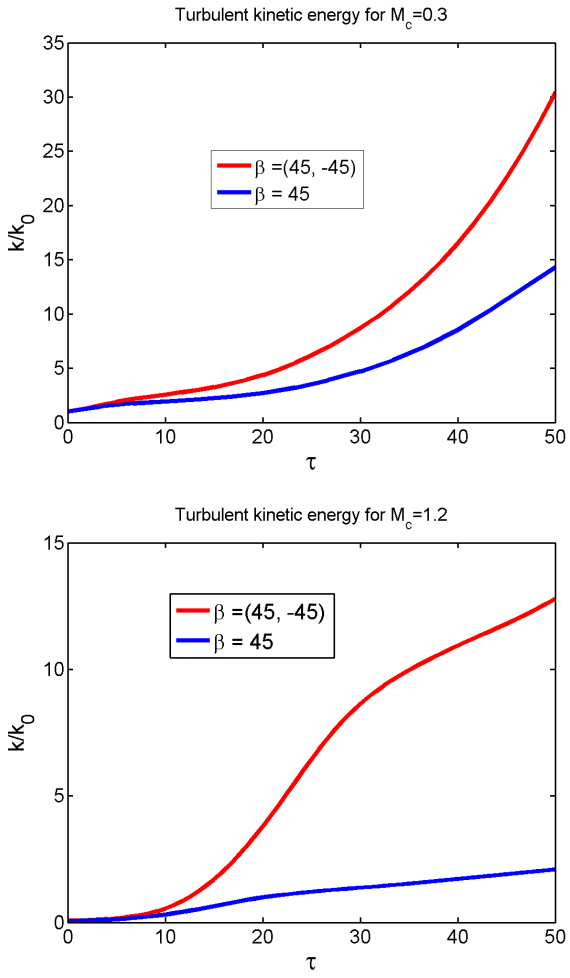

Figure VI.14. The evolution of the turbulent kinetic energy for a singleton with the obliqueness angle of $\beta = \pi/4$ and a pair wavemode with the obliqueness angle of $\beta = (\pi/4, -\pi/4)$ at (a) $M_c = 0.3$ and (b)$M_c = 1.2$.

Energy spectrum of initial single modes: The energy content as a function of κ_1 and κ_3 for a single mode at two different initial Mach numbers of $M_c = 0.3$ and 1.2 are compared in in Figures VI.15 and VI.16, respectively. The contour plots are shown for the times marked in VI.14. Initially, for both low and high Mach numbers, the most energetic waves are of the obliqueness of $\pi/4$, shown in Figure VI.15 (a) and Figure VI.16(a). For both low and high Mach numbers, the most energetic modes remain at the same wavenumber since non-linearity results in other oblique modes.

Energy spectrum of initial coupled modes: To understand the non-linear effects in compressible flows, the energy content of a coupled mode ($\beta = \pm\pi/4$) is investigated at low ($M_c = 0.3$) and high ($M_c = 1.2$) Mach numbers shown in Figure VI.17 and Figure VI.18, respectively. Comparisons of wavespectra evolution of the coupled wave modes at low and high Mach numbers reveal that energy transfers toward the spanwise direction under the influence of compressibility. This is due to the fact that at low Mach number flows, the growth of low β perturbations are not suppressed, while at high Mach number flows, the lower *beta* modes are, the more inhibited by compressibility.

In coupled modes, the new spanwise modes arising from triadic interaction are more energetic than the original or streamwise modes. Hence, the new spanwise modes are responsible for accelerated instability. Observation of the temporal evolution of single modes and coupled modes indicate that at a low Mach number most modes exhibit growth along their initial obliqueness angle. For single initial modes, contrasted with coupled initial modes, there are not many new spanwise or streamwise wave modes created.

Summary. For initial single modes of perturbation, energy remains with the same obliqueness angles under the influence of compressibility. Degree of suppression increases with β. For initial couple modes, compressibility moves the energy toward the spanwise direction. This is related to the fact that low β modes play a key role in the non-linear interaction such that high β mode growth is independent of compressibility effects, whereas the growth of low β modes is suppressed by compressibility.

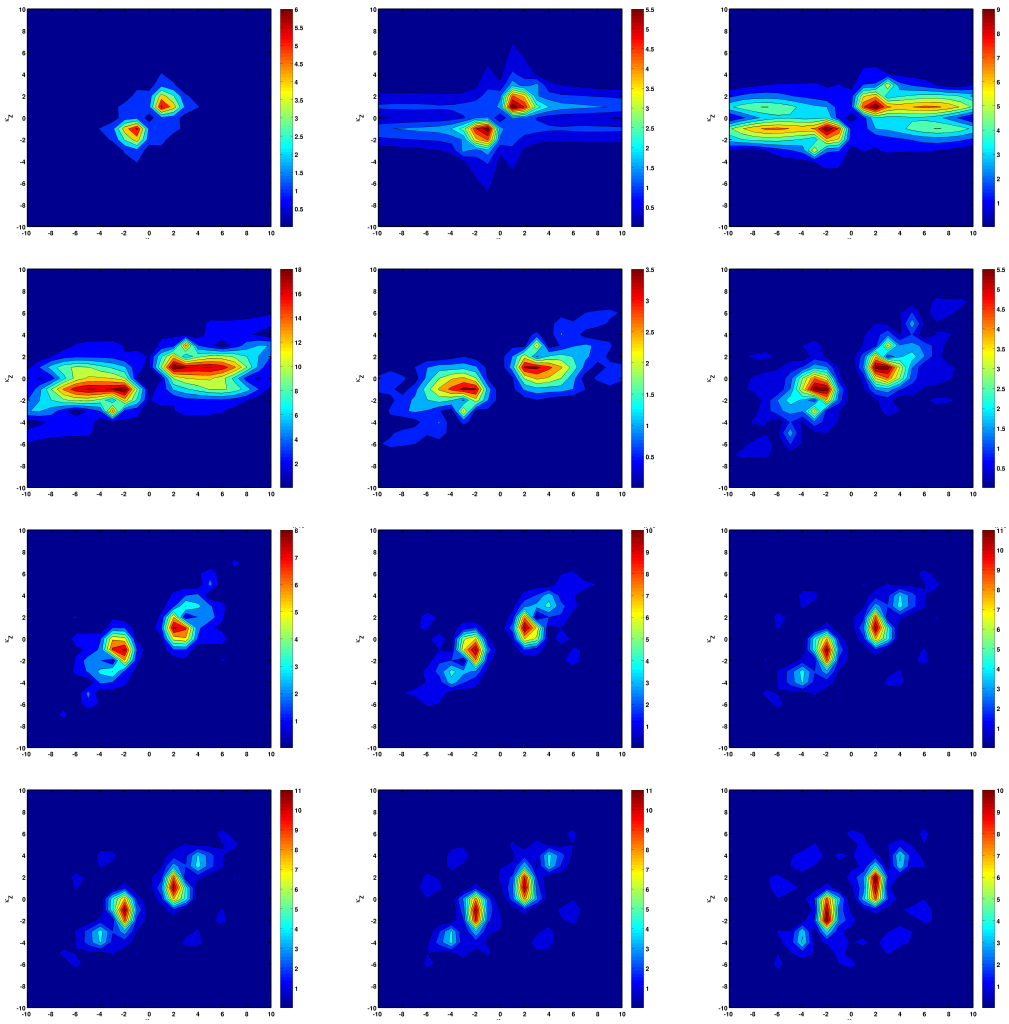

Figure VI.15. Temporal evolution of the wavevector spectrum of a singleton at Mach number contours for $M_c = 0.3$ at $\tau =$ (a) 0, (b)4, (c)8, (d)12, (e)16, (f)21, (g)25, (h)29, (i)31, (j)33, (k)37 and (l) 41. Dash gray line indicates the initial obliqueness angle.

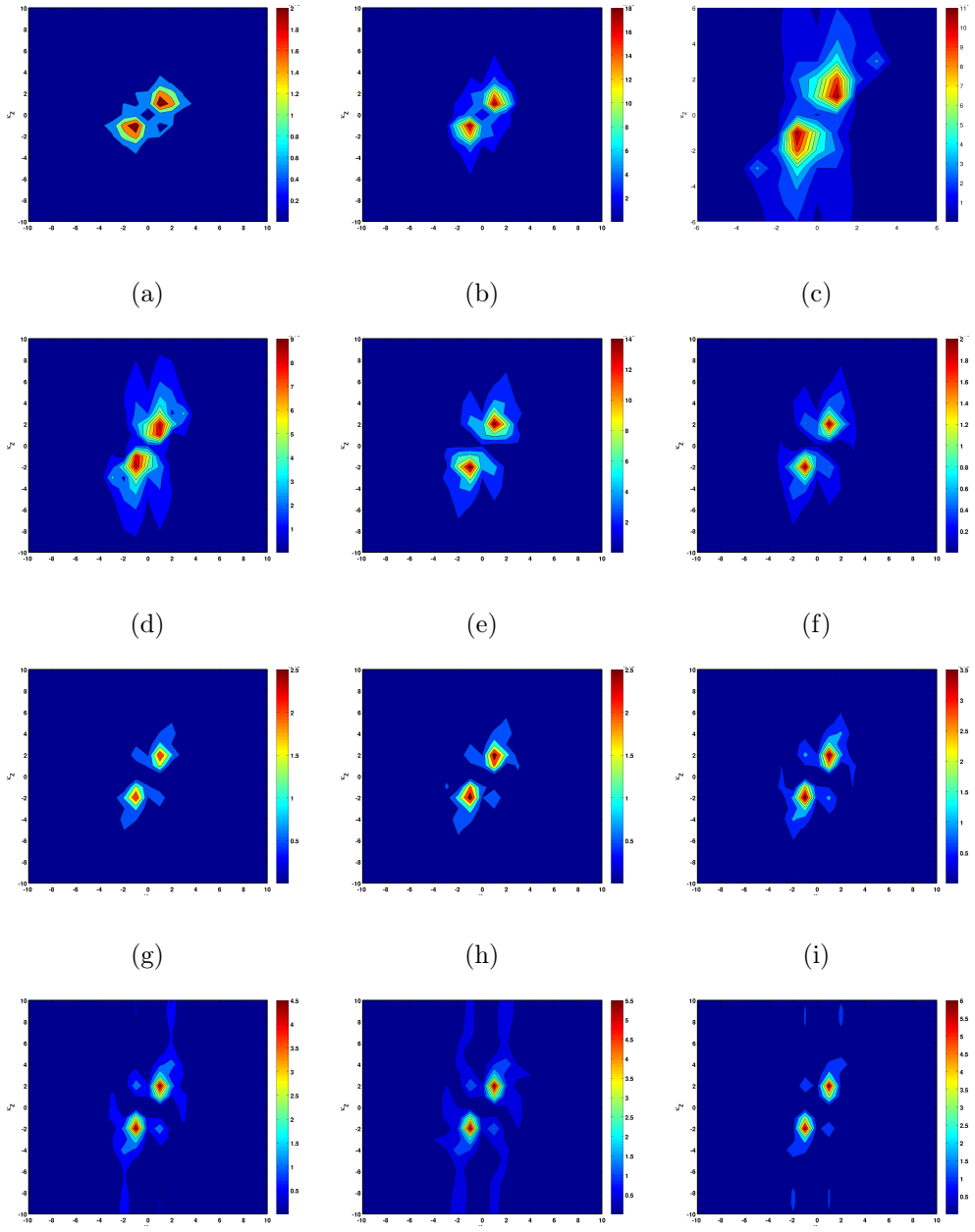

(a) (b) (c)

(d) (e) (f)

(g) (h) (i)

(j) (k) (l)

Figure VI.16. Temporal evolution of the wavevector spectrum of a singleton at Mach number contours for $M_c = 1.2$ at $\tau =$ (a) 0, (b)4, (c)8, (d)12, (e)17, (f)20, (g)23, (h)27,(i)33, (j)37, (k)40 and (l) 43. Dash gray line indicates the initial obliqueness angle.

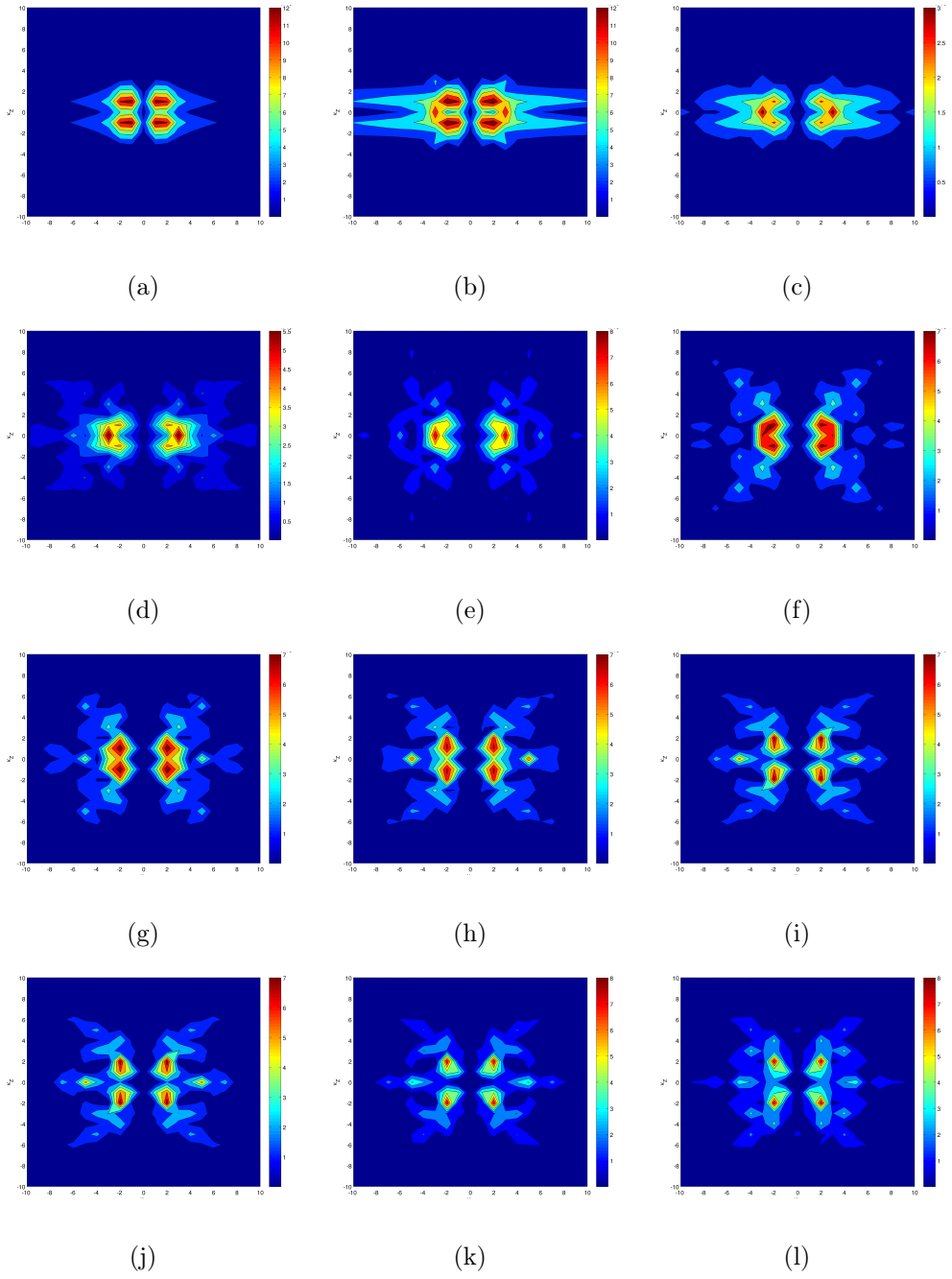

Figure VI.17. Temporal evolution of the wavevector spectrum of a pair wavemode at Mach number contours for $M_c = 0.3$ at $\tau =$ (a) 0, (b)4, (c)8, (d)12, (e)16, (f)21, (g)25, (h)29, (i)31, (j)33, (k)37 and (l) 41. Dash gray line indicates the initial obliqueness angle.

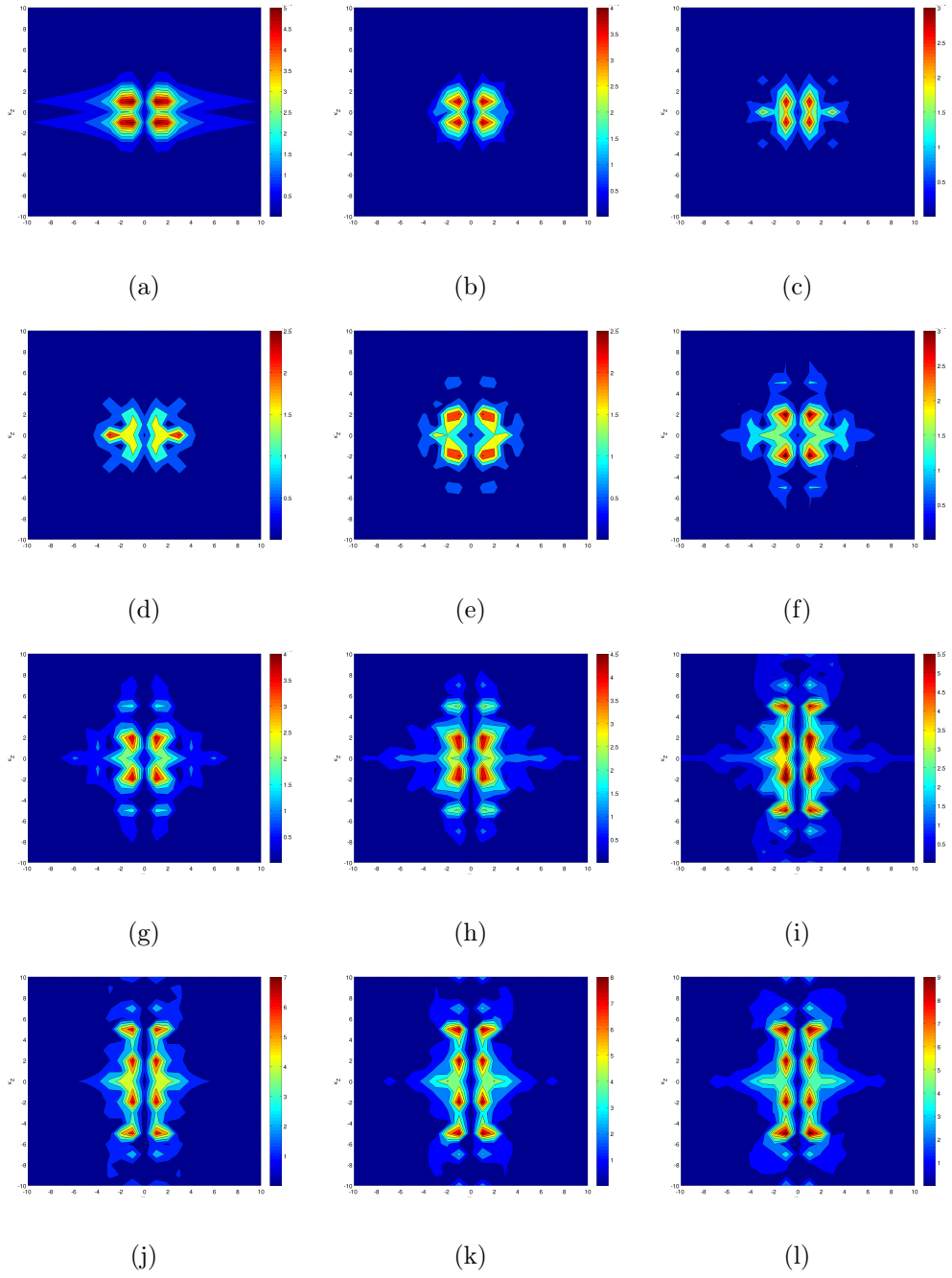

(a) (b) (c)

(d) (e) (f)

(g) (h) (i)

(j) (k) (l)

Figure VI.18. Temporal evolution of the wavevector spectrum of a pair at Mach number contours for $M_c = 1.2$ at $\tau =$ a) 0, (b)4, (c)8, (d)12, (e)17, (f)20, (g)23, (h)27 ,i)33, (j)37, (k)40 and (l) 43. Dash gray line indicates the initial obliqueness angle.

VII

MIXING LAYER FLOW STRUCTURE

It has been well-established in literature that compressibility not only affects the stability characteristics, but also the flow structure in mixing layers [34, 37, 81, 156–158]. Incompressible turbulent mixing layers are made of two primary coherent flow structures: (i) spanwise vortices (rollers) and (ii) streamwise vortices (ribs) [79, 159]. Spanwise rollers are known to arise from the KH instability. In compressible mixing layers, on other hand, the KH instability is inhibited as established earlier in this thesis. In this chapter change in the structure for the mixing layer with different obliqueness angles at different Mach numbers is investigated. First, we examine the flow structure of fully turbulent mixing layer. To explain, we also scrutinize, mixing layers at the linear growth subject to a single perturbation mode.

VII.A. Vortical Structure of Turbulent Mixing Layers

Spanwise vorticity fields of a turbulent mixing layer with the initial flow conditions similar to the DNS carried out by Pantano and Sarkar [2] at low ($M_c = 0.3$) and high (1.2) initial convective Mach numbers are presented in Figure VII.1 and VII.2, respectively. This data set is ideally suited for the present study as it has already been validated against the DNS of Pantano and Sarkar [2] in section IV.C.1.

Incompressible mixing layer structure. At low Mach numbers (e.g. $M_c = 0.3$), the side view of the spanwise vorticity, shown in Figure VII.1 (a), exhibits multiple spanwise rollers. These rollers are dominant only in the strong shear region

around the interface. The top view of the center-plane spanwise vorticity contours, depicted in Figure VII.1 (b), exhibits numerous rib-like structures throughout the spanwise plane .

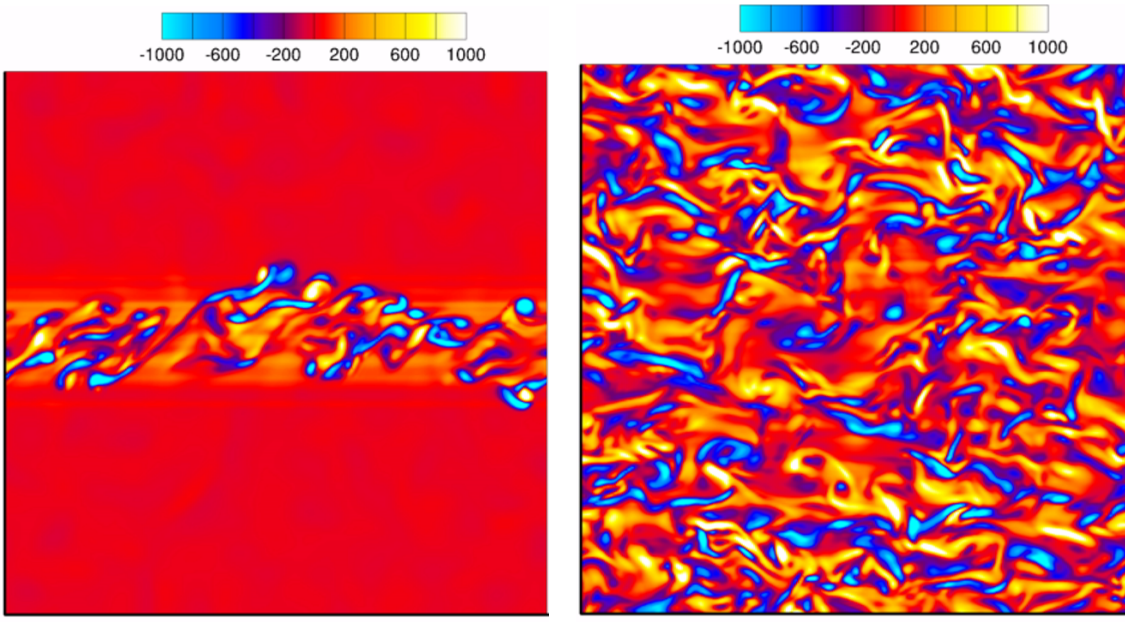

(a) (b)

Figure VII.1. Vorticity plots of the turbulent mixing layer simulation with the initial flow conditions of [2] at $M_c = 0.3$.

Compressible mixing layer structure. The spanwise vorticity structure in high Mach number simulation is shown in Figure VII.2 (a) (side view, z=0 plane) and Figure VII.2 (v) (top view, y=0 plane). The absence of the spanwise rollers is clearly evident. Instead of well-defined rollers, alternating strands of positive and negative vorticity along the streamwise direction are seen. The top view, shown in Figure VII.2 (b), further reinforced the fact that the elongated vortical structures are aligned along the streamwise direction. The absence of spanwise rollers is likely due

to the suppression of the KH instability at high speed. It would appear that in the absence of the KH rollers, the longitudinal structures link to form long streamwise coherent vortices of either sign.

To further highlight the change in vortex dynamics and the vortical structures, animations of the side view (x_1-x_2 plane) and top view (x_1-x_3 plane) of the spanwise vorticity at two different initial Mach numbers of $M_c = 0.3$ and $M_c = 1.2$ are available online.

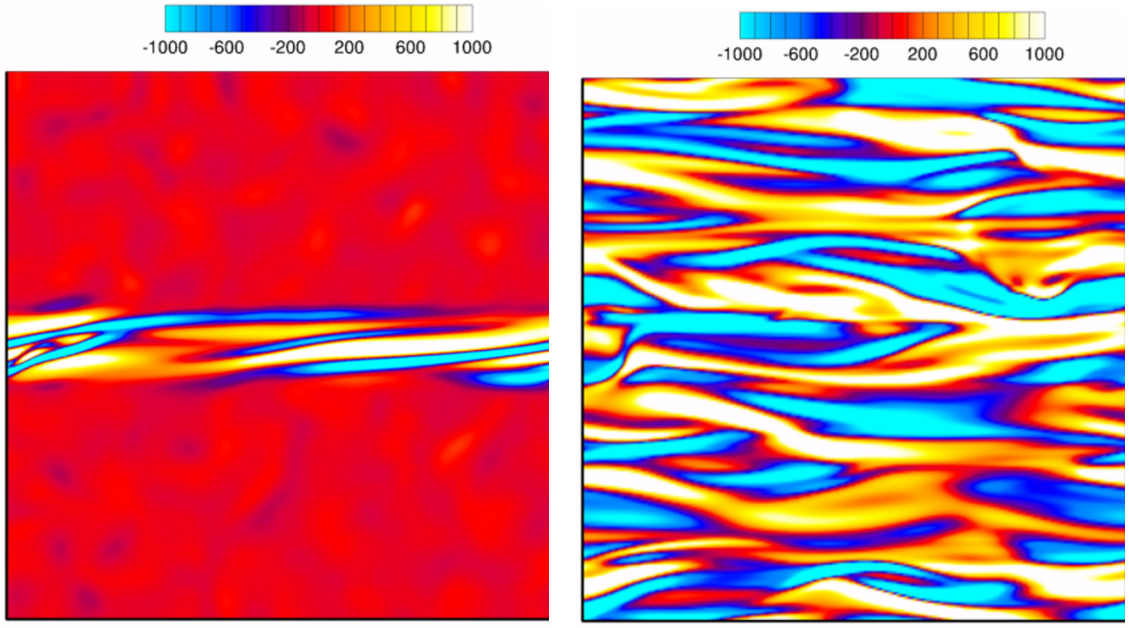

(a) (b)

Figure VII.2. Vorticity plots of the turbulent mixing layer simulation with the initial conditions of [2] at $M_c = 1.2$.

The largescale coherent structures seen in fully turbulent flows have their origins in linear stage of instability development. Therefore, we examine the vortical structure of linear perturbations at different obliqueness angles.

VII.B. Vortical Structure at Linear Growth Regime

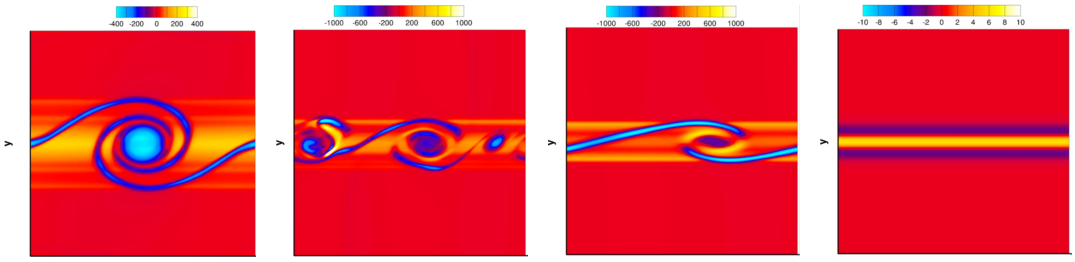

(a) (b) (c) (d)

Figure VII.3. Side view of vorticity contours at the initial convective Mach number of 0.3 at $\beta =$ (a) 0, (b) 30, (c) 60 and (d) 90

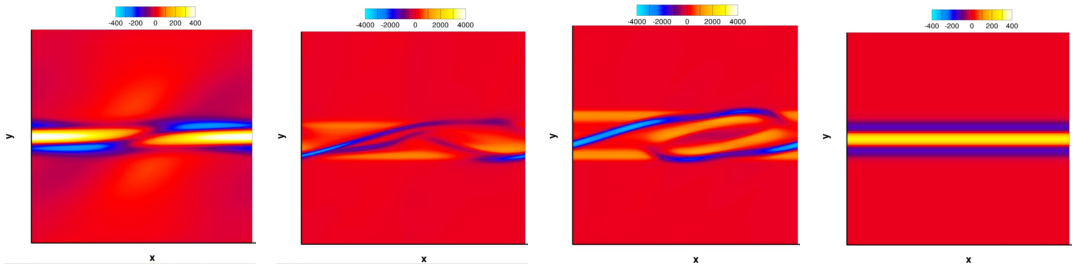

(a) (b) (c) (d)

Figure VII.4. Side view of vorticity contours at the initial convective Mach number of 1.2 at $\beta =$ (a) 0, (b) 30, (c) 60 and (d) 90

From the analysis in Chapter III, the linearized perturbation vorticity equations can be written as:

$$\frac{\partial \omega_1'}{\partial t} + U_1 \frac{\partial \omega_1'}{\partial x_1} = -\frac{1}{\bar{\rho}^2} \frac{\partial \bar{\rho}}{\partial x_2} \frac{\partial p'}{\partial x_3} - \frac{\partial U_1}{\partial x_2} \frac{\partial u_3'}{\partial x_1}, \tag{7.1}$$

$$\frac{\partial \omega_2'}{\partial t} + U_1 \frac{\partial \omega_2'}{\partial x_1} = -\frac{1}{\bar{\rho}^2} \frac{\partial \bar{\rho}}{\partial x_2} \frac{\partial p'}{\partial x_2} - \frac{\partial U_1}{\partial x_2} \frac{\partial u_2'}{\partial x_3}, , \tag{7.2}$$

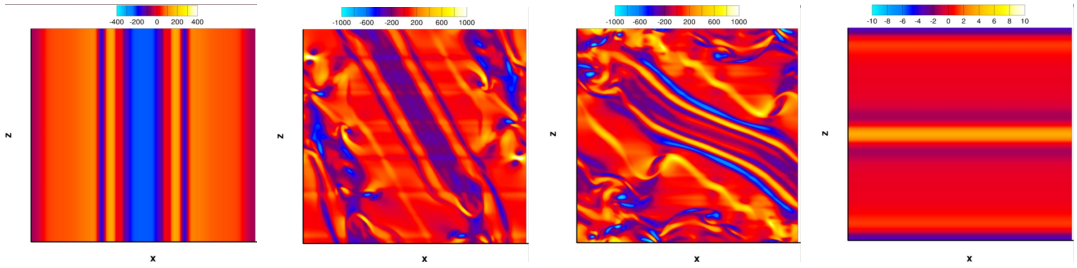

(a) (b) (c) (d)

Figure VII.5. Top view of vorticity contours at the initial convective Mach number of 0.3 at $\beta =$ (a) 0, (b) 30, (c) 60 and (d) 90

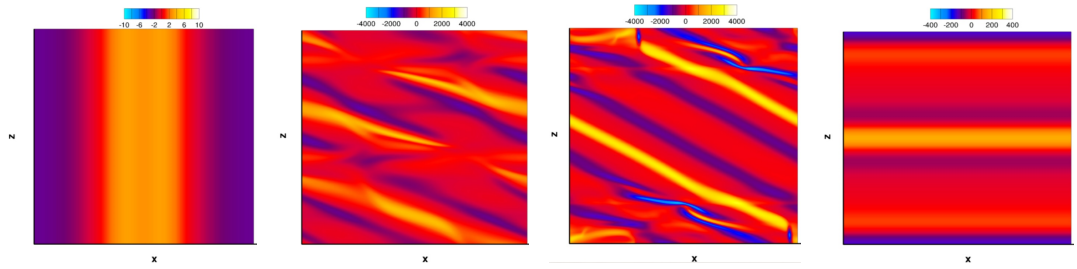

(a) (b) (c) (d)

Figure VII.6. Top view of vorticity contours at the initial convective Mach number of 1.2 at $\beta =$ (a) 0, (b) 30, (c) 60 and (d) 90

$$\frac{\partial \omega_3'}{\partial t} + U_1 \frac{\partial \omega_3'}{\partial x_1} = -\frac{1}{\bar{\rho}^2} \frac{\partial \bar{\rho}}{\partial x_2} \frac{\partial p'}{\partial x_1} - u_2' \frac{\partial^2 U_1}{\partial x_2^2} + \frac{\partial U_1}{\partial x_2} \left(\frac{\partial u_1'}{\partial x_1} + \frac{\partial u_2'}{\partial x_2} \right).$$

The first term on the righ-hand side of all above equations, the baroclinic term, is negligible since $\bar{\rho}$ is uniform in x_2 direction. The normal component of vorticity does not play an important role in the evolution of vortical structure since the variation of u_2' in the spanwise direction is small, thus $\partial u_2'/\partial x_3 \sim 0$ in the right-hand side of (7.2). For the types of initial perturbation considered in this study, the streamwise vorticity, ω_1', is not important as $\partial u_3'/\partial x_1$ is small and does not grow in time. Thus,

it suffices to focus on the spanwise vorticity, ω_3': Shear normal perturbations play a critical role in the ω_3' equation (7.3). As was shown in Chapter III, u_2' is govern by a wave equation:

$$\frac{\partial^2 \hat{u}_2^*}{\partial x_2^{*2}} + (\hat{u}_2^* S^* - \hat{u}_1^*) S^* + \frac{i}{\kappa} \frac{\hat{p}^*}{\gamma u^0} S \cos\beta = M_g^{*2} \frac{\partial^2 \hat{u}_2}{\partial t^{*2}}. \tag{7.3}$$

Recall that the compressibility effects manifest via, the effective gradient Mach number which includes the effect of shear rate and obliqueness angle of initial perturbation mode is defined by $M_g^* = S/(\bar{a}\kappa)\cos\beta$. To contrast the vortex dynamics of a mixing layer at different obliqueness angles between incompressible and compressible flows, a side view (x_1-x_2 plane) of the spanwise vorticity contours from simulations with perturbation of different obliqueness angles ($\beta = 0, 30, 60, 90°$) at low $M_c = 0.3$ and high $M_c = 1.2$ are depicted in Figure VII.3 and Figure VII.4, respectively. The top view of the same structure is presented in Figure VII.5 and Figure VII.6. The dependence of flow structure on perturbation orientation can now be summarized:

1. For $\beta = 90°$, $M_g^* = 0$. Then regardless of the initial convective Mach number, vorticity evolution will remain impervious to compressibility in (7.3), as shown in Figure VII.3 (d) and VII.4 (d). This is also evident by comparing the vorticity evolution from top view in Figure VII.5 (d) and VII.6 (d).

2. For $\beta = 0°$, $M_g^* = S/(\bar{a}\kappa)$. Therefore compressibility has the strongest effect on the evolution of u_2' according to the equation (7.3). At low Mach number ($M_c = 0.3$), the strong structure of the spanwise roller leads to the formation of *cat's eye*, shown in FigureVII.3 (a). At high Mach number ($M_c = 1.2$), the wave-like nature of u_2' causes the vortical structures to become oscillatory. Furthermore, pressure is also wave-like. This prevents roll up of the vortex sheets that leads to KH

initially. These positive and negative vortices retain their early sheet-like structure aligned along the x_1 direction. The lack of strong rotational motion also results in vortex sheets from adjacent pivot points to link with one another. As a result, long coherent vortex streaks of negative and positive vorticity form and persist for an extended period of time.

3. For $0^\circ < \beta < 90^\circ$, structures of intermediate obliqueness angles experience indeterminate level of vortex suppression. Comparing the top view of vorticity contour at $\beta = 30, 60^\circ$ depicted in VII.6 (b and c) with their incompressible counterparts depicted in VII.5 (b and c) indicates compressibility favors formation of longitudinal vortices, while it suppresses the spreading rates of the mixing layer through the inhibition of the spanwise rollers. It is evident that as the obliqueness angle increases (from $\beta = 0$ to 90°), the effects of compressibility on flow structures decreases.

In high Mach number of fully turbulent and linear growth-regime mixing layers at high Mach numbers, the sheet-like vortex structures at the interface clearly inhibit mixing. It is evident that the two streams are segregated in the high-speed mixing layer.

VII.C. Segregation of Two Streams

Finally, we examine if the two streams that constitute the mixing layer are indeed segregated by pressure effects at high speeds. To highlight this effect, a set of six fluid particles in each stream across the initial interface of the mixing layer are tagged at the initial times and their motion is monitored. The motion of the 12 tagged fluid particles in low and high Mach number turbulent mixing layer is shown

in Figure VII.7 and Figure VII.8, respectively. The online version also contains animations of the particle paths. The low Mach-number pathlines clearly move cross the initial interface between the two streams and meander far from their origins, indicating efficient mixing. In contrast, the high Mach-number pathlines stay within their stream of origin without crossing the interface. This clearly demonstrates that (i) the interface segregates the two streams; (ii) even within each stream mixing is significantly suppressed. This verifies the presence of the DIL near the initial interface of two streams in a high-speed mixing layer. The DIL acts as a buffer layer preventing mixing between two streams. In summation, the action of pressure leads to stirring motion between the two streams at low speeds, but merely a shaking of the interface at high speeds.

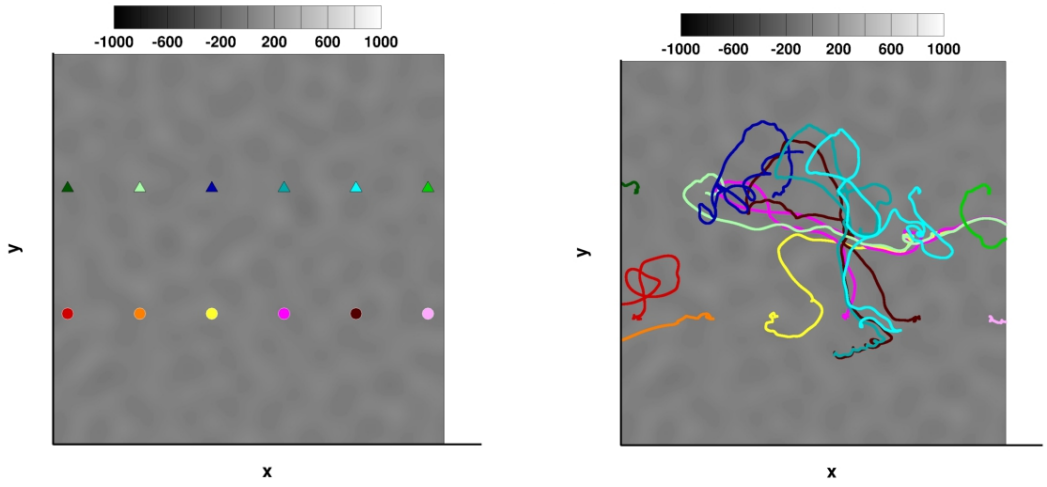

(a) (b)

Figure VII.7. The temporal evolution of the velocity perturbation pathlines with the embedded vorticity contour plots for a mixing layer with the initial isotropic turbulent velocity field at $M_c = 0.3$ (a) initial $\tau = 0$ (b) at $\tau = 250$ (color).

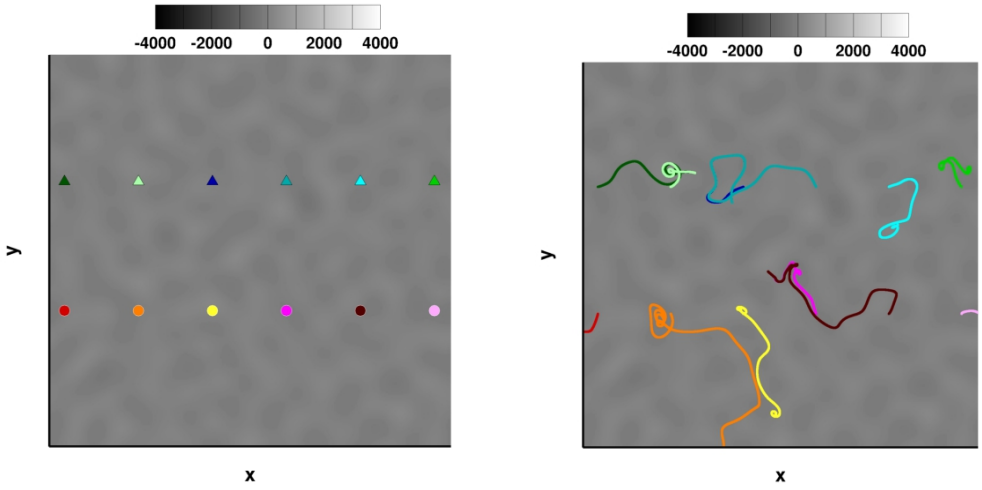

(a) (b)

Figure VII.8. The temporal evolution of the velocity perturbation pathlines with the embedded vorticity contour plots for a mixing layer with the initial isotropic turbulent velocity field at $M_c = 1.2$ (a) initial $\tau = 0$ (b) at $\tau = 250$ (color).

VIII

SUMMARY AND CONCLUSIONS

From experiments and numerical simulations, it has been well established that compressibility can severely reduce the spreading rate in high-speed mixing layers. It has also been observed that the flow structure, specifically vorticity, changes significantly with Mach number. In literature several studies have examined compressibility effect on mixing and flow structure. It has been shown that perturbation obliqueness also plays a critical role in the flow dynamics of compressible mixing layers. While important progress has been made, a comprehensive physical explanation that consolidates the effects of compressibility and perturbation on mixing and vorticity structure is yet to be developed. The objective of this thesis is to further our understanding of the interplay between various physical phenomena in high-speed mixing layers, and to attempt to develop a more complete explanation. The thesis comprises of three studies, and employs linear analysis and direct numerical simulations.

Study I—It is well-established that the Kelvin-Helmholtz (KH) instability is central to shear flow mixing. Toward understanding the suppression of turbulent mixing under the influence of compressibility, we first examine the modification to KH instability at high speeds. It is also known from previous studies [101] that the compressibility effect is more accurately parameterized by so-called gradient Mach number rather than convective Mach number. In this study, combining the outcomes of the linear stability analysis with the results of the numerical simulation, we

establish that the flow domain can be classified into three regions: the far-field region on the fast side, far-field region on the slow side and dilatational interface layer (DIL) in the middle. The DIL experiences very high gradient Mach numbers and compressibility effects. In both the high- and low-speed far-field regions, the local gradient Mach numbers are small, even though the convective Mach number can be large. Within the DIL, the pressure is governed by the inhomogeneous wave equation. As a consequence, the pressure-velocity coupling leads to oscillatory motion in the streamwise direction at the interface. Importantly, due to this strong streamwise oscillations, the DIL acts as a barrier between the fast and slow moving fluids. The oscillatory pressure and velocity fields of the DIL set the boundary conditions for the flow in the high- and low-speed outer regions. The resulting motion in each outer region is nearly oscillatory. This sequence of compressible flow phenomena leads to inhibition of the K-H instability and mixing.

Study II— The second study uses linear analysis to establish that the effect of compressibility decreases when the perturbation is inclined away from the shear plane. Indeed, spanwise perturbations do not experience any compressibility effects. The evolution of perturbations of various degrees of obliqueness is examined.

Study III— In the final study, we extend the inferences of the effect of compressibility and obliqueness to flow structure. While the streamwise structures are unaffected, the spanwise rollers are suppressed and deformed by the effect of compressibility. In the absence of the spanwise rollers, the streamwise structures align to form long coherent streamwise streaks. Thus, the thesis consolidates the effect of Mach number and obliqueness on mixing efficiency and flow structure. Future works

can employ this insight to develop strategies to predict and control mixing efficiency in high-speed mixing layers.

REFERENCES

[1] Papamoschou, D. and Roshko, A., "The compressible turbulent shear layers: an experimental study," *Journal of Fluid Mechanics*, Vol. 9, 1988, pp. 453–477.

[2] Pantano, C. and Sarkar, S., "A study of compressibility effects in the high-speed turbulent shear layer using dircet simulation," *Journal of Fluid Mechanics*, Vol. 451, 2002, pp. 329–371.

[3] Silva, I. P. D. D., Fernando, H., Eaton, F., and Hebert, D., "Evolution of Kelvin-Helmholtz billows in nature and laboratory," *Earth Planet. Sci. Lett*, , No. 84-0368, 1996.

[4] Fritts, D., Palmer, T., Andreassen, O., and Lie, I., "Evolution and breakdown of Kelvin–Helmholtz billows in stratified compressible flows. Part I: comparison of two- and three-dimensional flows," *J. Atmos. Sci.*, Vol. 53, 1996, pp. 3173–3191.

[5] Blumen, W., Bantab, R., Burnsc, S., Fritts, D., Newsome, R., Poulosd, G. S., and Sun, J., "Turbulence statistics of a Kelvin–Helmholtz billow event observed in the night-time boundary layer during the Cooperative atmosphere–surface exchange study field program," *Dyn. Atmos. Oceans*, Vol. 34, 2001, pp. 189–204.

[6] Haren, H. V. and Gotiaux, L., "A deep ocean Kelvin-Helmholtz billow train," *Geophys. Res. Lett.*, Vol. 37, No. 8, 2010, pp. L03605.

[7] Miura, A., "Anomalous transport by magnetohydrodynamic KelvinHelmholtz instabilities in the solar windmagnetosphere interaction," *Journal of Geophysical Research*, Vol. 89, No. A2, 1984, pp. 801–818.

[8] Miura, A., "Simulation of Kelvin-Helmholtz instability at the magnetospheric boundary," *Journal of Geophysical Research*, Vol. 92, No. A4, 1987, pp. 3195–3206.

[9] Miura, A., "Self-organization in the two-dimensional Kelvin-Helmholtz instability," *Phys. Rev. Lett.*, Vol. 83, No. 8, 1999, pp. 1586–1589.

[10] Foullon, C., Verwichte, E., Nakariakov, V. M., Nykyri, K., and Farrugia, C. J., "Magnetic Kelvin-Helmholtz instability at the sun," *The Astrophysical Journal Letter*, Vol. 729, No. 1, 2011, pp. 1–4.

[11] Hasegawa, H., Fujimoto, M., Phan, T., Rème, H., Balogh, A., Dunlop, M. W., Hashimoto, C., and TanDokoro, R., "Transport of solar wind into Earth's magnetosphere through rolled-up Kelvin–Helmholtz vortices," *Nature*, Vol. 430, 2004, pp. 755–758.

[12] Hasegawa, A., *Plasma Instabilities and Nonlinear Effects*, Springer, New York, 1975.

[13] Nagano, H., "Effect of finite ion Larmor radius on the Kelvin-Helmholtz instability of the magnetopause," *Planet. Space Sci*, Vol. 27, No. 6, 1979, pp. 881–884.

[14] Farrugia, C. J., Sandholt, P. E., and Burlaga, L. F., "Auroral activity associated with Kelvin-Helmholtz instability at the inner edge of the low-latitude boundary layer," *Journal of Geophysical Research*, Vol. 99, 1994.

[15] Ershkovich, A. I., Prialnik, D., and Eviatar, A., "Instability of a comet ionopause: Consequences of collisions and compressibility," *Journal of Geophysical Research*, Vol. 91, 1986.

[16] Gamezo, V. N., Khokhlov, A. M., Oran, E. S., Chtchelkanova, A. Y., , and Rosenberg, R. O., "Thermonuclear supernovae: Simulations of the deflagration dtage and their implications," *Science*, Vol. 299, 2003, pp. 77–81.

[17] Burrows, A., "Supernova explosions in the Universe," *Nature*, Vol. 430, 2000, pp. 727–733.

[18] Nomoto, K., Iwamoto, K., and Kishimoto, N., "Type Ia Supernovae: Their origin and possible applications in cosmology," *Science*, Vol. 276, 1997, pp. 1378–1382.

[19] Gomez, G. C. and Ostriker, E. C., "The effect of the Coriolis force on Kelvin-Helmholtz-driven mixing in protoplanetary disk," *The Astrophysical Journal*, Vol. 630, 2005, pp. 1093–1106.

[20] Keppens, R., Toth, G., Westermann, R. H. J., and Goedblod, J. P., "Growth and saturation of the Kelvin–Helmholtz instability with parallel and antiparallel magnetic fields," *J. Plasma Physics*, Vol. 61, No. 1, 1999, pp. 1–19.

[21] Baty, H. and Keppens, R., "Kelvin-Helmholtz disruptions in extended magnetized jet flows," *Astronomy and Astrophysics*, Vol. 447, No. 1, 2006, pp. 9–22.

[22] Lesieur, M., *Turbulent in Fluids*, Springer, Dordrecht, The Netherlands, 4th ed., 2008.

[23] Drake, R. P., *High-Energy-Density Physics: Fundamentals, Inertial Fusion and Experimental Astrophysics*, Springer, New York, 2006.

[24] Smits, A. J. and Dussauge, J.-P., *Turbulent Shear Layers in Supersonic Flows*, Springer, Princeton University, 2nd ed., 2006.

[25] Chinzei, N., Masuya, G., Komuro, T., Murakami, A., and Kudou, K., "Spreading of twostream supersonic turbulent mixing layers," *Physics of Fluids*, Vol. 29, No. 5, 1986, pp. 1345–1347.

[26] Clemens, N. T. and M.G.Mungal, "Two- and three-dimensional effects in the supersonic mixing layer," *AAA Journal*, Vol. 30, No. 4, 1992, pp. 973–981.

[27] Hall, J. L., Dimotakis, P. E., and Rosemann, H., "Experiments in non-reacting compressible shear layers," *AIAA Journal*, Vol. 31, No. 12, 1993, pp. 2247–2254.

[28] Samimy, M. and Elliot, G. S., "Effects of compressibility on the characteristics of free shear layers," *AIAA Journal*, Vol. 28, No. 3, 1990, pp. 439–445.

[29] Goebel, S. G. and Dutton, J. C., "Experimental study of compressible turbulent mixing layers," *AIAA Journal*, Vol. 29, No. 4, 1991, pp. 538–546.

[30] Birch, S. and Eggers, J., "A critical review of the experimental data for developed free turbulent shear layers," *NASA SP-321*, 1973, pp. 11–40.

[31] Papamoschou, D. and Roshko, A., "Observations of supersonic free shear layers," *AIAA paper*, , No. 86-0162, 1986.

[32] Brown, G. and Roshko, A., "On density effects and large structures in turbulent mixing layers," *Journal of Fluid Mechanics*, Vol. 64, 1974, pp. 775–816.

[33] Bradshaw, P., "Compressible turbulent shear layers," *Annual Review of Fluid Mechanics*, Vol. 9, 1977, pp. 33–54.

[34] Sandham, N. D. and Reynolds, W. C., "Three-dimensional simulations of large eddies in the compressible mixing layer," *Journal of Fluid Mechanics*, Vol. 224, 1991, pp. 133–158.

[35] Vreman, A. W., Sandham, N. D., and Luo, K. H., "Compressible mixing layer growth rate and turbulence characteristics," *Journal of Fluid Mechanics*, Vol. 320, 1996, pp. 235–258.

[36] J. B. Freund, S. K. L. and Moin, P., "Compressible effects in a turbulent annular mixing layer. Part I. Turbulence and growth rate," *Journal of Fluid Mechanics*, Vol. 421, 2000, pp. 229–267.

[37] Lesieur, M., Comte, P., and Lamballais, E., "Large- and small-scale stirring of vorticity and a passive scalar in a 3D temporal mixing layer," *Physics of Fluids A*, Vol. 4, No. 12, 1992.

[38] Foysi, H. and Sarkar, S., "The compressible mixing layer: an LES study," *Theor. Comput. Fluid Dyn.*, Vol. 24, No. 6, 2010, pp. 565–588.

[39] Hadjadj, A., Yee, H. C., and Sjögreen, B., "LES of temporally evolving mixing layers by an eight-order filter scheme," *Int.J.Numer.Meth.Fluids*, Vol. 70, 2012, pp. 1405–1427.

[40] Lessen, M., Fox, J. A., and Zien, H., "On the inviscid instability of laminar mixing of two parallel streams of a compressible fluid," *Journal of Fluid Mechanics*, Vol. 23, 1965, pp. 355–367.

[41] Lessen, M., Fox, J. A., and Zien, H. M., "Stability of the laminar mixing of two parallel streams with respect to supersonic disturbances," *Journal of Fluid Mechanics*, Vol. 25, 1966, pp. 737–742.

[42] Gropengiesser, H., "Study on the stability of boundary layers and compressible fluids," *NASA TT F-12*, 1970, pp. 786.

[43] Ragab, S. A. and Wu, J. L., "Linear instabilities in twodimensional compressible mixing layers," *Physics of Fluids A*, Vol. 1, No. 6, 1989, pp. 957–966.

[44] L., R., "On the stability of certain fluid motions," *Proc. Math. Soc. Lond.*, , No. 11, 1880, pp. 57–70.

[45] Miles, J., "On the generation surface waves by shear flows. 3. Kelvin-Helmholtz instability," *Journal of Fluid Mechanics*, Vol. 6, No. 4, 1959, pp. 583–598.

[46] Blumen, W., "Shear layer instability of an inviscid compressible fluid," *Journal of Fluid Mechanics*, Vol. 40, 1970, pp. 769–781.

[47] Blumen, W., Drazin, P. G., and Billings, D. F., "Shear layer instability of an inviscid compressible fluid. Part 2," *Journal of Fluid Mechanics*, Vol. 71, 1975, pp. 305–316.

[48] Drazin, P. G. and Davey, A., "Shear layer instability of an inviscid compressible fluid. Part 3," *Journal of Fluid Mechanics*, Vol. 82, 1977.

[49] Jackson, T. L. and Grosch, C. E., "Inviscid spatial stability of a compressible mixing layer," *Journal of Fluid Mechanics*, Vol. 208, 1989, pp. 609–637.

[50] Jackson, T. L. and Grosch, C. E., "Absolute/convective instabilities and the convective Mach number in a compressible mixing layer," *Physics of Fluids*, , No. 2, 1990, pp. 949–954.

[51] White, F. M., *Viscous Fluid Flow*, McGraw-Hill, New York, 1974.

[52] Mack, L. M., "On the inviscid acoustic-mode instability of supersonic shear flows," *Theor. Comput. Fluid Dyn.*, Vol. 2, No. 2.

[53] Walker, J., Talmage, G., Brown, S., and Sondergaard, N., "Kelvin–Helmholtz instability of Couette flow between vertical walls with a free surface," *Physics of Fluids*, Vol. A, No. 5, 1993, pp. 1466–1471.

[54] Bau, H. H., "Kelvin–Helmholtz instability for parallel flow in porous media: a linear theory," *Physics of Fluids*, Vol. 25, 1982, pp. 1719–1722.

[55] Miles, J. W., "On Kelvin–Helmholtz instability," *Physics of Fluids*, Vol. 23, 1980, pp. 1915–1916.

[56] Wang, L. F., Xue, C., Ye, W. H., and Li, Y. J., "Destabilizing effect of density gradient on the Kelvin–Helmholtz instability," *Phys. Plasma*, Vol. 16, 2009, pp. 112104.

[57] Wang, L. F., Ye, W. H., and Li, Y. J., "Combined effect of the density and velocity gradients in the combination of Kelvin–Helmholtz and Rayleigh–Taylor instabilities," *Phys. Plasma*, Vol. 17, 2010, pp. 042103.

[58] Blaauwgeers, R., Eltsov, V. B., Eska, G., Finne, A. P., Haley, R. P., Krusius, M., Ruohio, J. J., Skrbek, L., and Volovik, G. E., "Shear flow and Kelvin-Helmholtz instability in superfluids," *Phys. Rev. Lett.*, Vol. 89, No. 15, 2002, pp. 155301.

[59] Bodo, G., Mignone, A., and Rosner, R., "Kelvin-Helmholtz instability for relativistic fluids," *Phys. Rev. E*, Vol. 70, 2004, pp. 36304.

[60] Horton, W., Perez, J., Carter, T., and Bengtson, R., "Vorticity probes and the characterization of vortices in the Kelvin-Helmholtz instability in the large plasma device experiment," *Phys. Plasma*, Vol. 12, No. 2, 2005, pp. 022303.

[61] Chimonas, G., "The extension of the Miles-Howard theorem to compressible fluids," *Journal of Fluid Mechanics*, Vol. 43, 1970, pp. 833–836.

[62] Betchov, R. and Szewczyk, A., "Stability of a shear layer between parallel streams," *Physics of Fluids*, Vol. 6, No. 10, 1963, pp. 1391–1396.

[63] Schmid, P. J. and Henningson, D. S., *Stability and Transition in Shear Flows*, Springer–Verlag, Berlin–Heidelberg–New York, 2001.

[64] Breidenthal, R., "Structure in turbulent mixing layers and wakes using a chemical reaction," *Journal of Fluid Mechanics*, Vol. 109, 1981, pp. 1–24.

[65] Winant, C. D. and Browand, F. K., "Vortex pairing: the mechanism of turbulent mixing-layer growth at moderate Reynolds number," *Journal of Fluid Mechanics*, Vol. 63, 1974, pp. 237–255.

[66] Lasheras, J., Cho, J., and Maxworthy, T., "On the origin and evolution of streamwise vortical structures in a plane, free shear layer," *Journal of Fluid Mechanics*, Vol. 172, 1986, pp. 231–258.

[67] Elliot, G. S. and Samimy, M., "Compressibility effects in free shear layers," *Physics of Fluids A*, Vol. 2, 1990.

[68] Bell, J. and Mehta, R., "Measurement of the streamwise vortical structures in a plan mixing layer," *Journal of Fluid Mechanics*, Vol. 239, 1992, pp. 213–248.

[69] Ho, C.-M. and Huerre, P., "Perturbed Free Shear Layers," *Annual Review of Fluid Mechanics*, Vol. 16, 1984, pp. 365–424.

[70] Peltier, W. R. and Caulfield, C. P., "Mixing Efficiency in Stratified Shear Flows," *Annual Review of Fluid Mechanics*, Vol. 35, 2003, pp. 135–167.

[71] Brown, G. and Roshko, A., "The effect of density difference on the turbulent mixing layer," *Turbulent Shear Flows AGARD-CP*, , No. 93, 1971, pp. 23–1.

[72] Hernan, M. and Jimenez, J., "Computer analysis of a high-speed film of the plane turbulent mixing layer," *Journal of Fluid Mechanics*, Vol. 119, 1982, pp. 323–345.

[73] Jimenez, J., "A spanwise structure in the plane shear layer," *Journal of Fluid Mechanics*, Vol. 132, 1983, pp. 319–336.

[74] Bernal, L. and Roshko, A., "Streamwise vortex structure in plane mixing layers," *Journal of Fluid Mechanics*, Vol. 170, 1986, pp. 499–525.

[75] Lin, S. and Corcos, G., "The mixing layer: deterministic models of a turbulent flow. Part 3. The effect of plane strain on the dynamics of streamwise vortices," *Journal of Fluid Mechanics*, Vol. 141, 1984, pp. 139–178.

[76] R.W. Metcalfe, S.A. Orszag, M. B. S. M. and Riley, J., "Secondary instability of a temporally growing mixing layer," *Journal of Fluid Mechanics*, Vol. 184, 1987, pp. 207–243.

[77] Moser, R. and Rogers, M., "The three-dimensional evolution of a plane mixing layer: pairing and transition to turbulence," *Journal of Fluid Mechanics*, Vol. 247, 1993, pp. 275–320.

[78] Rogers, M. M. and Moser, R. D., "The three-dimensional evolution of a plane mixing layer: the Kelvin-Helmholtz rollup," *Journal of Fluid Mechanics*, Vol. 243, 1992, pp. 183–226.

[79] Rogers, M. M. and Moser, R. D., "Spanwise scale selection in plane mixing layers," *Journal of Fluid Mechanics*, Vol. 247, 1993, pp. 321–337.

[80] Adams, N. and Sandham, N., "Numerical simulation of boundary-layer at Mach two," Vol. 51, 1993, pp. 371–375.

[81] Luo, K. and Sandham, N., "On the formation of small scales in a compressible mixing layers," *Direct and Large-Eddy Simulation I*, Vol. 26, 1994, pp. 335–346.

[82] Kourta, A. and Sauvage, R., "Computation of supersonic mixing layers," *Physics of Fluids*, Vol. 14, No. 11, 2002, pp. 3790–3797.

[83] Y. Yao, L. Krishnan, N. D. S. and Roberts, G. T., "The effect of Mach number on unstable disturbances in shock/boundary layer interactions," *Physics of Fluids*, Vol. 19, 2007, pp. 054104–15.

[84] Livescu, D. and Madnia, C. K., "Small scale structure of homogeneous turbulent shear flow," *Physics of Fluids*, Vol. 16, No. 8, 2004, pp. 2864.

[85] Lee, J., "Dynamical behavior of the fundamental triadinteraction system in threedimensional homogeneous turbulence," *Physics of Fluids*, Vol. 22, No. 40, 1979, pp. 40–53.

[86] Cambon, C., Tesseidre, C., and Jeandel, D., "Effects couples de dèformation et de rotation sur une turbelence homogène," *J. Mec. Theor. Appl.*, Vol. 4, 1985, pp. 629–657.

[87] Waleffe, F., "The nature of triad interactions in homogeneous turbulence," *Physics of Fluids*, Vol. 4, No. 2, 1992, pp. 350–363.

[88] Waleffe, F., "Inertial transfer in the helical decomposition," *Physics of Fluids*, Vol. 5, No. 3, 1993, pp. 677–685.

[89] Smith, L. M. and Waleffe, F., "Generation of slow large scales in forced rotating stratified turbulence," *Journal of Fluid Mechanics*, Vol. 451, 2002, pp. 145–168.

[90] Kida, S., Kraichnan, R. H., Rogallo, R. S., and andand Y. Zhou, F. W., "Trial interactions in the dissipation range," *Proc. of the Summer Program*, Stanford University, Center for Turbulence Research, Stanford, CA, 1992.

[91] Moore, D., "The effect of compressibility on the speed of propagation of a vortex ring," *Proc.R.Soc.Lond*, Vol. A, No. 397, 1985, pp. 87–97.

[92] Sandham, N., "The effect of compressibility on vortex pairing," *Physics of Fluids*, Vol. 6, No. 2, 1994, pp. 1063–1072.

[93] Vreman, B., Kuerten, H., and Geurts, B., "Shocks in direct numerical simulation of the confined three-dimensional mixing layer," *Physics of Fluids*, Vol. 7, No. 9, 1995, pp. 3790–3797.

[94] Bernal, L., *The coherent structure of turbulent mixing layers. I similarity of the primary vortext structure.II secondary streamwise vortex structure*, Ph.D. thesis, 1981.

[95] Bogdanoff, D., "Compressibility effects in turbulent shear layes," *AIAA*, Vol. 21, 1983, pp. 926–927.

[96] Coles, D., "Prospects for useful research on coherent structures in turbulent shear flow," *P.Indian AS-Eng Sci*, Vol. 4, 1981, pp. 111–127.

[97] Dimotakis, P. E., "Entrainment into a fully developed, two-dimensional shear layer," *AIAA, Paper No.*, , No. 84-0368, 1984.

[98] Chandrasekhar, S., *Hydrodynamic and Hydromagnetic Stability*, Oxford Clarendon Press, London, 1981.

[99] Birch, S. and Keyes, J., "Transition in compressible free Shear Layers," *Journal of Spacecraft and Rockets*, Vol. 9, No. 8, 1972, pp. 623–624.

[100] Blaisdell, G., Mansour, N., and Reynolds, W., "Compressibility effects on the growth and structure of homogeneous turbulent shear flow," *Journal of Fluid Mechanics*, Vol. 253, 1993, pp. 443–485.

[101] Sarkar, S., "The stabilizing effect of compressibility in turbulent shear flow," *Journal of Fluid Mechanics*, Vol. 282, 1995, pp. 163–186.

[102] S. Barre, J.-P Bonnet, T. G. and Sandham, N., "Compressible, high speed flows," *Closure strategies for sodeling turbulent and transitional tlows*, edited by B. Launder and N. Sandham, Cambridge University Press, Cambridge, 2002, pp. 522–581.

[103] Zhuang, M., Kubota, T., and Dimotakis, P. E., "Instability of inviscid, compressible free shear layers," *AIAA J.*, Vol. 28, No. 10, 1989, pp. 1728–1733.

[104] Lu, G. and Lele, S. K., "On the density ratio effect on the growth rate of a compressible mixing layer," *Physics of Fluids A*, Vol. 6, No. 2, 1994, pp. 1074–1075.

[105] Aluie, H., "Compressible turbulence: the cascade and its locality," *Phys. Rev. Lett.*, Vol. 106, No. 17, 2011, pp. 174502.

[106] Aluie, H., "Scale decomposition in compressible turbulence," *Physica D*, Vol. 247, No. 1, 2013, pp. 54–65.

[107] Prichett, L. P., Wu, c. C., and Dawson, J. M., "Interchange instabilities in a compressible plasma," *Physics of Fluids*, Vol. 21, No. 9, 1978, pp. 1958–1988.

[108] Howarth, L., "Concerning the effect of compressibility on laminar boundary layers and their separation," *Proc. Roy. Soc. A.*, Vol. 194, No. 1036, 1948, pp. 16.

[109] Betchov, R. and Criminale, W. O., *Stability of Parallel Flows*, Academic Press, New York, 1st ed., 1967.

[110] Bayly, B. J., "Three-dimensional instability of elliptical flow," *Phys. Rev. Lett.*, Vol. 57, No. 17, 1986, pp. 2160–2164.

[111] Landman, M. J. and Saffman, P. G., "The threedimensional instability of strained vortices in a viscous fluid," *Physics of Fluids*, Vol. 30, No. 8, 1987, pp. 2329–2342.

[112] Simone, A., Coleman, G. N., and Cambon, C., "The effect of compressibility on turbulent shear flow: a rapid-distortion-theory and direct-numerical-simulation study," *Journal of Fluid Mechanics*, Vol. 330, 1997, pp. 307–338.

[113] Kumar, G., Bertsch, R. L., and Girimaji, S. S., "Stabilizing action of pressure in homogeneous compressible shear flows: effect of Mach number and perturbation obliqueness," *Journal of Fluid Mechanicsanics*, Vol. 760, 2014, pp. 540–566.

[114] Xu, K., "Gas-Kinetic Schemes for Unsteady Compressible Flow Simulations," VKI for Fluid Dynamics Lecture Series 1998-03, 1998.

[115] May, G., Srinivasan, B., and Jameson, A., "An improved gas-kinetic BGK finite-volume method for three-dimensional transonic flow," *Journal of Computational Physics*, Vol. 220, 2007, pp. 856–878.

[116] Bird, G., *Molecular Gas Dynamics and the Direct Simulation of Gas Flows*, Oxford University Press, Oxford, 1994.

[117] C.Cercignani, *The Boltzmann Equations and its Applications*, Springer-Verlag, New York/Berlin, 1988.

[118] Sandres, R. H. and Prendergast, K. H., "The possible relation of the 3-kiloparsec arm to explosions in the galactic nucleus," *The Astrophysical Journal*, Vol. 188, 1974, pp. 489–500.

[119] Pullin, D. I., "Direct simulation methods for compressible inviscid ideal gas flow," *Journal of Computational Physics*, Vol. 34, 1980, pp. 231–244.

[120] Reitz, R. D., "One-dimensional compressible gas dynamics calculations using the Boltzmann equations," *Journal of Computational Physics*, Vol. 42, 1981, pp. 108–123.

[121] Deshpande, S. M., "A second order accurate, kinetic theory based method for inviscid compressible flows," *NASA Langley Report*, , No. 2613, 1986.

[122] Xu, K., "BGK-based scheme for multicomponent flow calculations," *Journal of Computational Physics*, Vol. 134, 1997, pp. 122–133.

[123] Xu, K., "A Gas-Kinetic BGK scheme for the Navier-Stokes equations and its connection with artificial dissipation and Godunov method," *Journal of Computational Physics*, Vol. 171, No. 1, 2001, pp. 289–335.

[124] Kerimo, J. and Girimaji, S., "Boltzmann-BGK approach to simulating weakly compressible 3D turbulence: comparison between lattice Boltzmann and gas kinetic methods," *Journal of Turbulence*, Vol. 8, No. 46, 2007, pp. 1–16.

[125] K. Xu, X. H. and Cai, C., "Multiple temperature kinetic model and gas-kinetic method for hypersonic nonequilibrium flow computations," *Journal of Computational Physics*, Vol. 227, 2008, pp. 6779–6794.

[126] Bhatnagar, P. L., Gross, E. P., and Krook, M., "A model for collision processes in gases I. Small amplitude processes in charged and neutral one-component systems," *Physical Review*, Vol. 9, 1954, pp. 511–525.

[127] Vincenti, W. G. and Kruger, C. H., *Introduction to Physical Gas Dynamics*, Wiley, New York, 4th ed., 1965.

[128] Kogan, M. N., *Rarefied Gas Dynamics*, Plenum, New York, 1969.

[129] Shu, C.-W., "Essentially non-oscillatory and weighted essentially non-oscillatory schemes for hyperbolic conservation laws," *ICASE*, Vol. Technical Report 97-65, 1997.

[130] Jiang, G.-S. and Shu, C.-W., "efficient implementation of weighted ENO schemes," *Journal of Computational Physics*, Vol. 126, 1996, pp. 202–228.

[131] S., S. C. and Cowling, T. G., *The mathematical theory of non-uniform gases: an account of the kinetic theory of viscosity, thermal conduction and diffusion in gases*, Cambridge University Press, New York, 3rd ed., 1991.

[132] Xu, K., Mao, M., and Tang, L., "mutidimensional gas-Kinetic BGK scheme for hypersonic viscous flows," *Journal of Computational Physics*, Vol. 203, No. 2, 2005, pp. 405–421.

[133] Pope, S. B., *Turbulent Flows*, Cambridge University Press, Cambridge, 2000.

[134] Zaman, K. B. M. Q. and Hussain, A. K. M. F., "Taylor hypothesis and large-scale coherent structures," *Journal of Fluid Mechanics*, Vol. 112, 1981, pp. 379–396.

[135] Buell, J. and Mansour, N., "Asymmetric effects in three-diemnsional spatially developing mixing layers," *Proc. Seventh Intl Symp. on Turbulent Shear Flows*, Standford University, Standford, CA, 1989.

[136] Lee, S., Lele, S. K., and Moin, P., "Simulation of spatially evolving turbulence and the applicability of Taylor's hypothesis in compressible flow," *Physics of Fluids A*, Vol. 4, No. 7, 1992, pp. 1074–1075.

[137] Wyngaard, J. C. and Clifford, S. F., "Taylor's hypothesis and high–frequency turbulence spectra," *J. Atmos. Sci.*, Vol. 34, 1977, pp. 922–929.

[138] Pierrhumbert, R. T. and Widnall, S. E., "The two-and three-dimensional instabilities of a spatially periodic shear layer," *Journal of Fluid Mechanics*, Vol. 114, 1982, pp. 59–82.

[139] Sreenivasan, K. R. and Antonia, R. A., "The phenomenology of small-scale turbulence," *Annual Review of Fluid Mechanics*, Vol. 29, 1997, pp. 435–472.

[140] Rogers, M. M., Moser, R. D., and Buell, J. C., "A direct comparison of spatially and temporally evolving mixing layers," *Bull. Am. Phys. Soc.*, 1990.

[141] Lui, G. and Lele, S. K., "Direct numerical simulation of spatially developing compressible mixing layers," *AIAA paper*, , No. 291, pp. 1–16 Year = 2001.

[142] Zhou, Q., He, F., and Shen, M. Y., "Direct numerical simulation of a spatially developing compressible plane mixing layer: flow structures and mean flow properties," *Journal of Fluid Mechanics*, Vol. 711, 2012, pp. 437–468.

[143] Wang, T., Shi, X., and Zhang, G., "Visualization of large-scale structures in spatially developing compressible mixing layers," *J. Visualization*, Vol. 16, No. 3, 2013, pp. 219–227.

[144] Thompson, K. W., "Time dependent boundary conditions for hyperbolic systems," *Journal of Computational Physics*, Vol. 68, No. 1, 1987, pp. 1–24.

[145] Rogers, M. M. and Moser, R. D., "Direct simulation of a self-similar turbulent mixing layer," *Physics of Fluids A*, Vol. 6, No. 2, 1994, pp. 903–923.

[146] Vreman, B., Kuerten, H., and Geurts, B., "Large Eddy Simulation of the temporal Mixing Layer Using the Clark Model," *Theor. Comput. Fluid Dyn.*, Vol. 8, 1996, pp. 309–324.

[147] Fathali, M., Meyers, J., Rubio, G., Smirnov, S., and Baelmans, M., "Sensitivity analysis of initial condition parameters on the transitional temporal turbulent mixing layer," *Journal of Turbulence*, Vol. 9, No. 12, 2008, pp. 1–28.

[148] Kumar, G., Girimaji, S. S., and Kerimo, J., "WENO-enhanced gas-kinetic scheme for direct simulations of compressible transition and turbulence," *Journal of Computational Physics*, Vol. 234, 2012, pp. 499.

[149] Xie, Z. and Girimaji, S. S., "Instability of Poiseuille flow at extreme Mach numbers: Linear analysis and simulations," *Phys. Rev. Lett. E*, Vol. 89, No. 15, 2014, pp. 043001.

[150] Drazin, P. G. and Reid, W., *Hydrodynamic Stability*, Cambridge University Press, New York, 1981.

[151] Lagnado, P. R., Phan-Thien, N., and Leal, L. G., "The stability of three-dimensional linear flows," *Physics of Fluids*, Vol. 27, No. 5, 1984.

[152] Leblanc, S., "Stability of stagnation points in rotating flows," *Physics of Fluids*, Vol. 9, No. 11, 1997, pp. 3566–69.

[153] Leblanc, S. and Cambon, C., "On the three-dimensional instabilities of plane flows subjected to Coriolis," *Physics of Fluids*, Vol. 9, No. 5, 1997, pp. 1307–16.

[154] Caulfield, C. P. and Kerswell, R. R., "The nonlinear development of three-dimensional disturbances at hyperbolic stagnation points: a model of the braid region in mixing layers," *Physics of Fluids*, Vol. 12, No. 5, 2000, pp. 1032–1042.

[155] Leblanc, S. and Cambon, C., "Effects of the Coriolis force on the stability of Sturat vortices," *Journal of Fluid Mechanics*, Vol. 356, 1998, pp. 353–379.

[156] Fouillet, Y., *Contribution a l'etude par experimenatation numerique des ecoulements cisailles libres. Effects de compressibilite*, Ph.D. thesis, Grenoble, 1992.

[157] Comte, P., Fouillet, Y., and Lesieur, M., "Simulation numerique des zones de melange compressibles," *Revu Scientifique et Technique dela Defense*, Vol. 3eme trimestre.

[158] Lesieur, M., Metais, O., and Comte, P., *Large-Eddy Simulations of Turbulence*, Cambridge, New York, 1st ed., 2005.

[159] Moser, R. and Rogers, M., "Mixing transition and the cascade to small scales in a planar mixing layer," *Physics of Fluids A*, Vol. 3, No. 5, 1991, pp. 1128–1134.